National Aeronautics and Space Administration

Final Report

Super Ball Bot - Structures for Planetary Landing and Exploration

for the

NASA Innovative Advanced Concepts (NIAC) Program

Principle-Investigator: Adrian Agogino, Ph.D.

Principle-Investigator: Vytas SunSpiral, MS.

Co-Investigator: David Atkinson Ph.D.

NASA Ames Research Center

Intelligent Systems Division

July, 2013

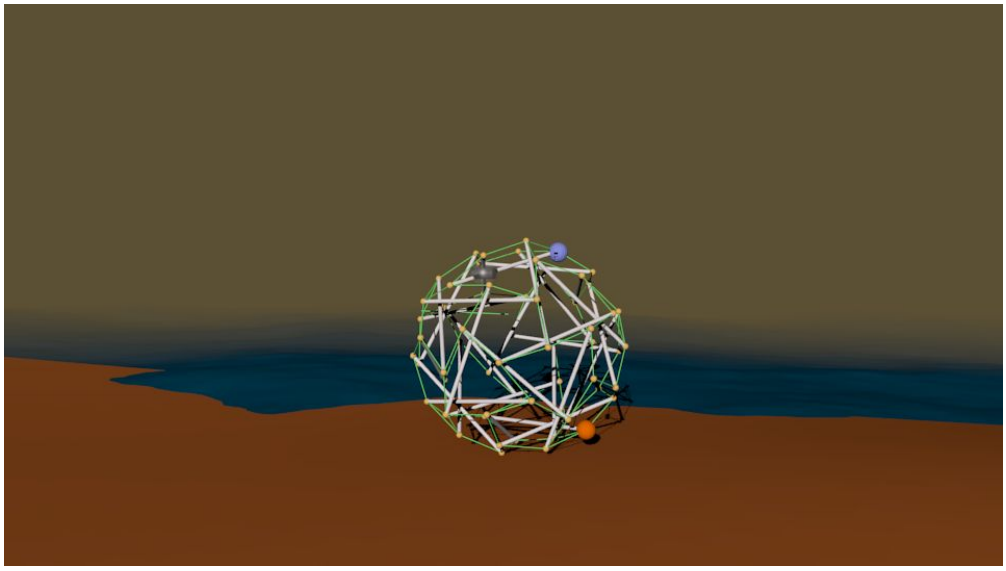

Contents

1 Executive Summary **5**

2 Introduction **7**

2.1 Mission Concept 7

2.2 Reusability, Redundancy, Reliability 7

2.3 Enabling the Mission 8

3 Organization of this Report **9**

4 Background on Tensegrity Robotics **10**

4.1 Tensegrity Structures 10

4.2 Tensegrity and Biology 11

4.3 Tensegrity Control 11

4.3.1 Control Based on Genetic/Evolutionary Algorithms 12

4.3.2 Control Based on Central Pattern Generators 12

5 Summary of Key Findings **14**

5.1 Define Notional Titan Mission and Requirements 14

5.2 Developing Control Algorithms using Evolution and Central Pattern Generators . . 15

5.3 Verification in Simulation and Hardware 17

6 Tensegrity Probes for a Notional Mission to Titan **19**

6.1 Motiviation for Titan Mission 19

6.2 Approach, Entry, Decent and Landing on Titan 21

6.2.1 Approach and Entry 22

6.2.2 Unpacking 22

6.2.3 Terminal Velocity Landing 22

6.3 Mobility 24

6.4 Scientific Study of Titan's Surface and Instrument Packages 24

6.4.1 Mass Analysis 26

6.5 Tensegrity Probes in Comparison to Other Flown Missions 26

7 Evolutionary Controls **29**

7.1 Target Tensegrity Platform 29

7.2 Tensegrity Actuation 29

7.3 Simulation 30

7.4 Evolutionary Algorithms . . . 31
7.5 Evaluation Function . . . 31
7.6 Centralized Evolutionary Algorithms . . . 31
7.7 Cooperative Coevolutionary Algorithms . . . 32
7.8 Hand-Coded Solution . . . 33
7.9 Experimental Results . . . 34
7.9.1 Centralized, Decentralized and Hand-Coded . . . 34
7.9.2 Historical Average, Average and Leniency . . . 35
7.9.3 Actuation Noise . . . 36
7.9.4 Broken Cable and Obstacles . . . 37
7.9.5 Updated Analysis Using 1.0 Meter Rods . . . 38

8 Dynamical and Central Pattern Generator Controls 40
8.1 Principle . . . 40
8.2 Reactive Method . . . 42
8.3 Inverse Kinematics Method . . . 43
8.3.1 First order IK . . . 43
8.3.2 Second order IK . . . 45
8.4 Gyroscopic Method . . . 46
8.5 CPG and Adaptive Frequency Oscillators Method . . . 48
8.5.1 Arbitrary Waveform Oscillator . . . 48
8.5.2 Hopf Oscillator . . . 50
8.6 Hybrid CPG - Inverse Kinematics method . . . 55
8.6.1 AWO and IK . . . 55
8.6.2 Hopf oscillators and IK . . . 56

9 Hardware Robot 58
9.1 Project Goals . . . 58
9.2 Structural Component . . . 58
9.2.1 Structure of Choice . . . 58
9.2.2 Structural Construction . . . 60
9.2.3 Motor Implementation . . . 60
9.2.4 Methods of Collapse . . . 60
9.2.5 Abaqus FEA Simulation . . . 61
9.3 Simulation and Electrical Aspects of the Spherical Tensegrity . . . 62
9.3.1 DC Gear Motors . . . 62

9.3.2 Control Systems 63

10 Landing Structure Analysis **64**

10.1 Simulation of Landing 64

10.1.1 Landing Simulation using Bullet Simulator 64

10.1.2 Landing Simulation using Euler-Lagrange (E-L) Solver 65

10.1.3 Detailed Impact Simulations and Cross-Validation Using Two Simulators . 67

10.1.4 Comparing Simulators to Hardware 69

10.1.5 Simulated Drop Tests and Payload Protection 70

10.1.6 Landing Orientation Studies 71

10.2 Drop Test of Actuated Hardware Tensegrity 72

10.3 Drop Test of Hardware Tensegrity with Payload 73

10.3.1 Tensegrity Configuration 73

10.3.2 Results 75

10.3.3 Droptest Evaluation 75

10.4 Conclusions from Landing Structure Analysis 78

11 Conclusions and Future Work **79**

12 Acknowledgements **82**

1 Executive Summary

Small, light-weight and low-cost missions will become increasingly important to NASA's exploration goals. Ideally teams of small, collapsible, light weight robots, will be conveniently packed during launch and would reliably separate and unpack at their destination. Such robots will allow rapid, reliable in-situ exploration of hazardous destination such as Titan, where imprecise terrain knowledge and unstable precipitation cycles make single-robot exploration problematic. Unfortunately landing lightweight conventional robots is difficult with current technology. Current robot designs are delicate, requiring a complex combination of devices such as parachutes, retrorockets and impact balloons to minimize impact forces and to place a robot in a proper orientation. Instead we are developing a radically different robot based on a "tensegrity" structure and built purely with tensile and compression elements. Such robots can be both a landing and a mobility platform allowing for dramatically simpler mission profile and reduced costs. These multi-purpose robots can be light-weight, compactly stored and deployed, absorb strong impacts, are redundant against single-point failures, can recover from different landing orientations and can provide surface mobility. These properties allow for unique mission profiles that can be carried out with low cost and high reliability (see Figure 1). We believe tensegrity robot technology can play a critical role in future planetary exploration.

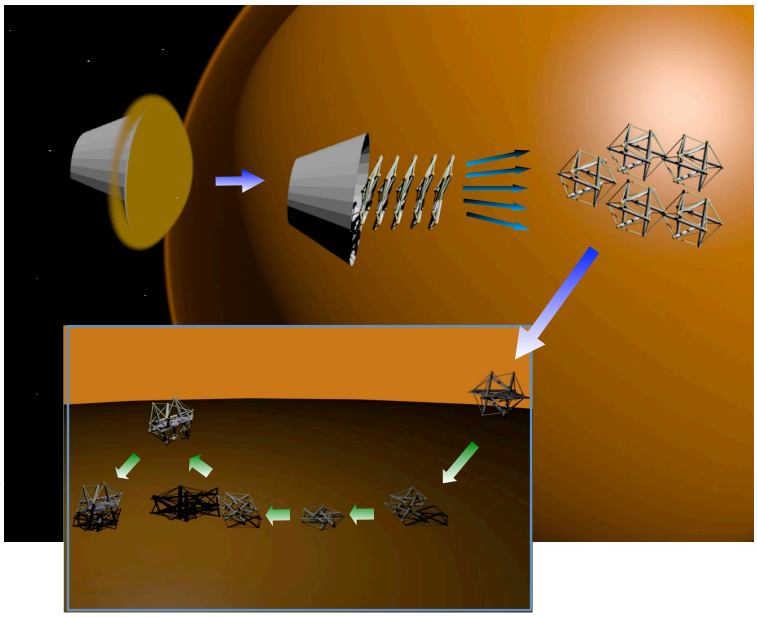

Figure 1: *Tensegrity structures are composed of pure compression and tension elements. They can be lightweight, reliable, deployable, and efficient to manipulate.* **Mission Scenario** - *Tightly packed set of tensegrities, expand, spread out, fall to surface of moon, then safely bounce on impact. The same tensegrity structure which cushioned the landing is then used for mobility to explore moons such as Titan and small asteroids.*

Our Phase I study explored: 1) Feasibility of applying tensegrities to a low-cost, high science return mission to Saturn's moon Titan. 2) Ability to control these structures that exhibit oscillatory and nonlinear behavior through evolutionary and central pattern generator based algorithms. 3)

Effectiveness of tensegrities as a landing and mobility platform. These studies resulted in three important conclusions:

1. Having analyzed the mission design from trajectory planning, to science instrument selection, deployment, and mass estimation, we showed that tensegrities can be an effective landing and mobility platform for a Titan mission. A tensegrity mission can have a high mass fraction between science payload and overall weight (as measured at atmospheric entry) due to its dual use as a landing system (like an airbag) and as a system for surface mobility. As a result, tensegrity based missions can be cheaper and open up new forms of surface exploration that take advantage of their natural tolerance to impacts.

2. We demonstrated in our physics based simulator that tensegrity probes can be controlled effectively with evolutionary and dynamical algorithms resulting in robust smooth rolling motion over a variety of terrains.

3. Using multiple analysis and simulation tools we showed that tensegrities are a very robust landing platform, and can protect delicate payloads from a landing impact of 15 m/s (and possibly beyond). This was further confirmed by performing drop tests on multiple physical prototypes.

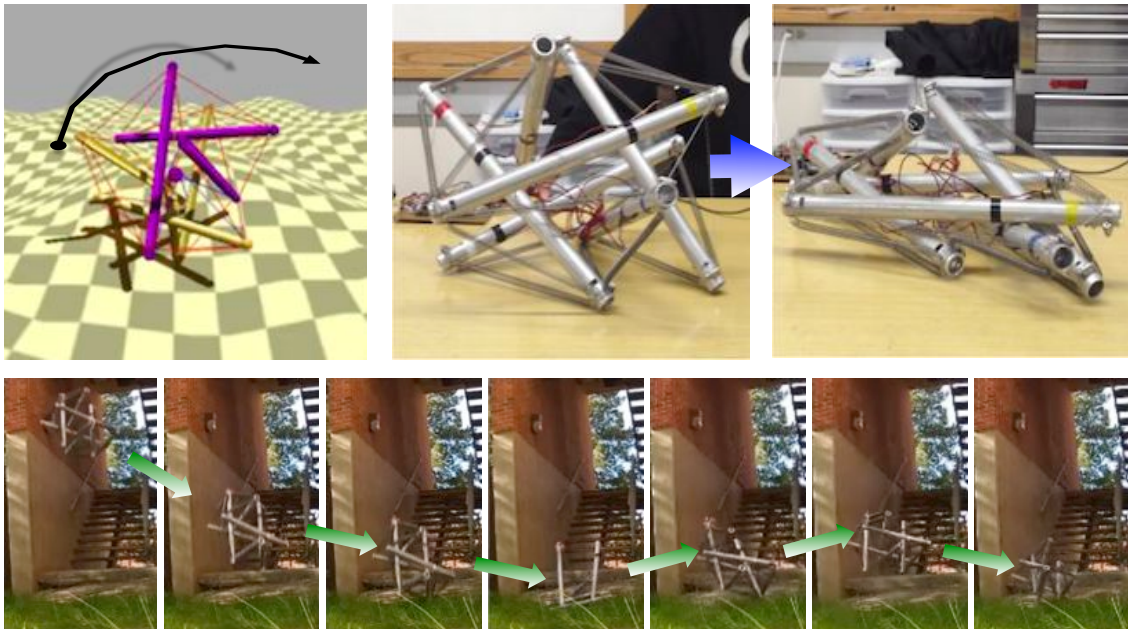

Figure 2: **Tensegrity Evaluations.** *Phase I study showed: A) That tensegrities can be controlled for mobility, B) That our partially actuated hardware prototype can be efficiently stowed and deployed (with greater stowage efficiency when fully actuated), and C) Analytical and physical drop tests confirm that the probe can serve as an effective landing platform.*

These results are summarized in Figure 2. We are glad to report that our results exceeded all expectations at the start of the project, thoroughly validating the overall tensegrity robot and landing platform concept. This work has already resulted in three full papers and one short paper publications [36, 34, 35, 2].

2 Introduction

2.1 Mission Concept

Tensegrity robots can facilitate an intriguing low-cost planetary exploration mission profile (see Figure 1) comprising of the following stages: 1) A set of tensegrity robots can be squeezed into a small launch platform; 2) After initial atmospheric entry and ejection of the heat shield, they can automatically spring away from each other when released at their destination. 3) They "bounce" on impact reducing the need for final descent equipment, such as airbags; and 4) They can reorient themselves from landed position without addition reorientation hardware and efficiently move from scattered initial positions to perform sensor measurements; 5) They can survive significant falls and are resistant to being stuck, simplifying route planning and allowing for more aggressive exploration in the pursuit of science.

Once on the surface, tensegrity robots can perform an array of scientific analysis including soil and atmospheric composition, surface imagery and microscopic analysis. To further reduce complexity, sensors can be suspended on the interior of the tensegrity on cables attached to the nodes, or when appropriate even to the nodes themselves so that the sensors can be moved with movements of the structure itself, eliminating the need for separate sensor arms. In addition, environmental analysis can be performed in-situ at the landing site, at different local locations, or even at distant locations given a tensegrity robot's potential for efficient locomotion. The biggest advantages of this mission profile are:

1. The structure of the robot itself provides capability for deployment, entry/decent/landing (EDL), and mobility, reducing complexity, risk, and mass compared to using three separate systems.
2. Tensegrity robots are light-weight and can be packed tightly, reducing cost;
3. Multiple robots expand science coverage and reduce risk.
4. Flexibility of robot design allows design reuse, reducing mission project risk.

2.2 Reusability, Redundancy, Reliability

This mission concept has three fundamental desirable properties 1) **Design Reusability** - The core design of a tensegrity robot is simply composed of modular rods which contain actuators, controls, power, and cables. All instances of these components are nearly identical and do not have to be custom designed, thus reducing complexity and project risk. In addition, using the same basic components of actuated tensegrity rods, many different morphologies are possible, with different landing and mobility characteristics that can be tailored to different missions. 2) **Redundancy** - Due to their light-weight and collapsibility, multiple tensegrity robots can be packed together and deployed, then land and carry out their mission independently. In addition, individual tensegrities are robust against actuator failure, as performance gracefully degrades as the number of failures

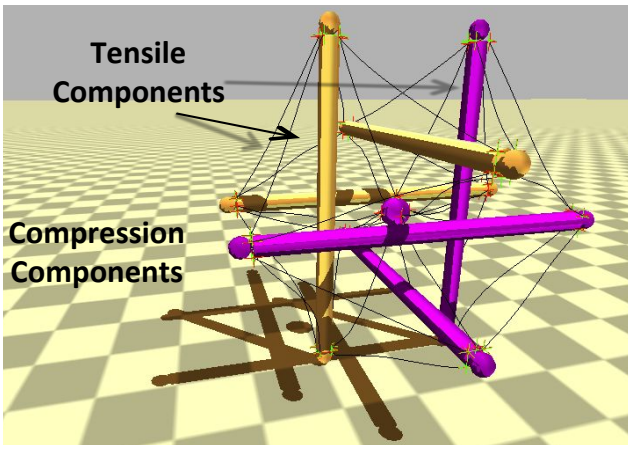

Figure 3: **Tensegrity Structure.** *Tensegrities are composed of pure tension and pure compression elements (e.g. cables and rods) as seen in this picture of a tensegrity robot from our physics based tensegrity simulator. They are light-weight, energy-efficient and robust to failures.*

increases. Note that in this study we mostly focus on the basic engineering, analysis, and testing of a single tensegrity robot, as that is a prerequisite to designing a multi-robot mission. 3) **Reliability** - Structural components can be made robust since they undergo pure linear tension and compression, reducing sheer and bending forces. In addition, the flexible nature of its movements allows the tensegrity robot to recover from awkward landing positions, being stuck, or even falling or rolling from significant heights.

2.3 Enabling the Mission

While tensegrities have the potential to dramatically reduce the cost and increase the reliability of robotic missions, significant technology development is still needed to enable such missions. Our study has made large strides towards showing that a tensegrity landing and mobility platform is feasible by showing that:

1. Having analyzed the mission design from trajectory planning, to science instrument selection, deployment, and mass estimation, we showed that tensegrities can be an effective landing and mobility platform for a Titan mission. A tensegrity mission can have a high mass fraction between science payload and overall weight (as measured at atmospheric entry) due to its dual use as a landing system (like an airbag) and as a system for surface mobility. As a result, tensegrity based missions can be cheaper and open up new forms of surface exploration that take advantage of their natural tolerance to impacts.

2. We demonstrated in our physics based simulator that tensegrity probes can be controlled effectively with evolutionary and dynamical algorithms resulting in robust smooth rolling motion over a variety of terrains.

3. Using multiple analysis and simulation tools we showed that tensegrities are a very robust landing platform, and can protect delicate payloads from a landing impact of 15 m/s (and

possibly beyond). This was further confirmed by performing drop tests on multiple physical prototypes.

These results served our Phase I study goals of showing that our tensegrity landing and mobility platform is theoretically possible and relevant to NASA.

3 Organization of this Report

The goal of this final report is to detail all of our activities related to our Phase I study. This report is organized as follows:

- Section 4 - A summary the basics of tensegrity robotics including their unique structure and possible control methods.
- Section 5 - A summary of our three key findings from our Phase I study as they relate to our three original research goals for this study.
- Section 6 - A detailed description of a notional mission to Titan describing both the mission and advantages a tensegrity probe has over traditional alternatives for landing and mobility.
- Section 7 - A detailed description how to control a tensegrity robot using evolutionary algorithms, including performance experiments in simulation showing how these algorithms are robust to numerous challenges.
- Section 8 - A detailed description of how dynamical controls and neuroscience inspired central pattern generators may be applied to tensegrity robotics.
- Section 9 - A detailed description of our initial hardware prototype designed to show deployment and landing characteristics along with a feasibility study for actuated tensegrities.
- Section 10 - A detailed analysis of the effectiveness of a tensegrity as a landing platform. This section includes analysis from a physics engine and an Euler-Lagrange solver and an analysis and comparison of the accuracy of the two simulators. The simulation studies are followed by drop tests of a hardware tensegrity with actuators for deployment, and drop tests of a tensegrity probe with a fragile payload.
- Section 11 - An outline of future work and the next steps required to mature this concept to Technology Readiness Level (TRL) 3.

Combined, these results form a strong picture of how a tensegrity robot can be used as an effective landing and mobility platform.

4 Background on Tensegrity Robotics

4.1 Tensegrity Structures

Tensegrity structures are composed of axially loaded compression elements encompassed within a network of tensional elements, and thus each element experiences either pure linear compression or pure tension. As a result, individual elements can be extremely lightweight as there are no bending or shear forces that must be resisted. An actively controlled tensegrity structure can be packed into small launch volumes and deployed when required. Active motion in tensegrity structures can be performed with minimal energy expenditure since actuators work linearly along the load paths in the tension elements, avoiding the torques caused by long lever arms of traditional robotic designs.

A unique property of tensegrity structures is how they can internally distribute forces. As there are no lever arms, forces do not magnify into joints or other common points of failure. Rather, externally applied forces distribute through the structure via multiple load paths, creating a system level robustness and tolerance to forces applied from any direction. Thus tensegrity structures can be easily reoriented in gravity fields and are ideally suited for operation in dynamic environments where contact forces cannot always be predicted. Likewise, tensegrities can be robust to the failure of individual actuation elements, resulting in a gradual reduction of overall workspace, rather than the loss of entire ranges of motion which are common in serial manipulators.

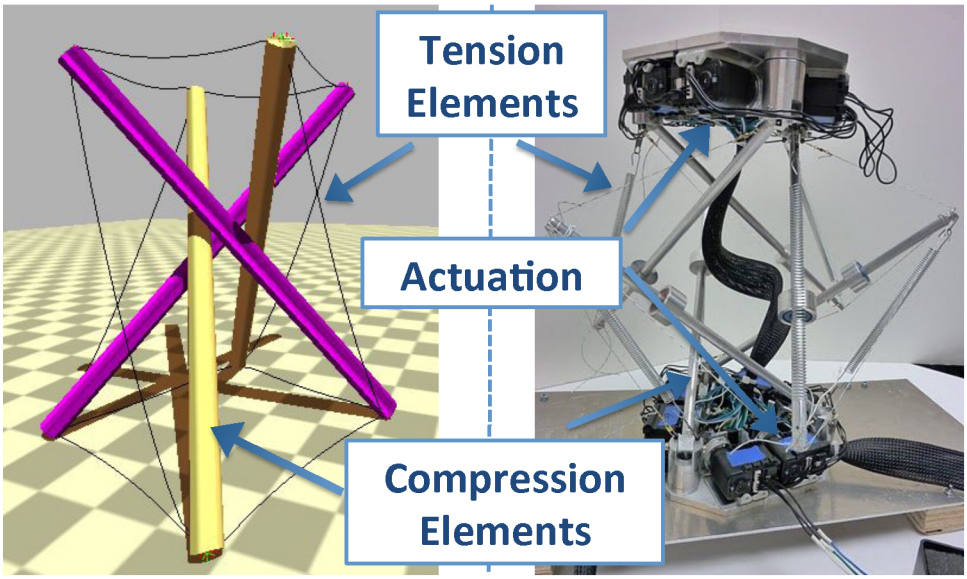

Figure 4: **Tensegrity Structures.** *Left: NASA Ames simulation of tensegrity showing compression and tension elements. Right: Prototype tensegrity robot at NASA Ames. For the prototype actuation is performed with electric motors and pulleys that change the length of tension elements. Future models may use other simple mechanisms to change cable length such as twisted cable actuation or electrically active polymers (EAP).*

4.2 Tensegrity and Biology

One of the most intriguing aspects of tensegrity structures is that they are being discovered in many aspects of biological systems. This property is being discovered at all scales, from the cytoskeleton of individual cells [32] to mammalian physiology [43]. Emerging biomechanical theories are shifting focus from bone-centric models to fascial-centric models [43, 16]. Fascia is the connective tissue in our bodies (including muscles, ligaments, tendons, etc.), and forms a continuous web of tension, even surrounding and supporting the bones which, unlike our traditional robots, have no rigid connections between them [53]. This new view is challenging the common sense view of our skeletal structure as the primary load bearing elements of our bodies. In the emerging biotensegrity model, bones are still under compression, but they are not passing compressive loads to each other, rather it is the continuous tension network of fascia (muscles, ligaments, tendons) that is the primary load path for forces passing through the body [42]. Recent anatomical research through fresh dissections (i.e. without preserving the cadaver, a process which changes the fascia) [52] is providing evidence of the global network of continuous connective tissue that manages force transfers in the body [53]. Tensegrity structures are a good model for this body-wide tension network [20].

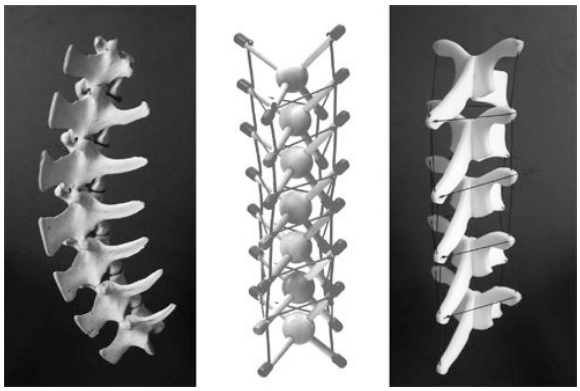

Figure 5: Tensegrity models of the spine showing how vertebrae float without touching, image courtesy of Tom Flemons (copyright 2006) [20]

4.3 Tensegrity Control

Tensegrity structures are a fairly modern concept, having been initially explored in the 1960's by Buckminster Fuller [21] and the artist Kenneth Snelson [75, 74]. For the first few decades, the majority of tensegrity related research was concerned with form-finding techniques [86, 48, 77, 87] and the design and analysis of static structures [5, 37, 73]. Research into control of tensegrity structures was initiated in the mid-1990's, with initial efforts at formalizing the dynamics of tensegrity structures only recently emerging [73]. The very properties that make tensegrities ideal for physical interaction with the environment (compliance, multi-path load distribution, non-linear dynamics, etc) also present significant challenges to traditional control approaches. A recent review [81] shows that there are still many open problems in actively controlling tensegrities. We believe that modern advances in control algorithms based on central pattern generators and distributed learning and genetic algorithms will be key elements in controlling tensegrity robots.

4.3.1 Control Based on Genetic/Evolutionary Algorithms

Instead of defining a control policy directly, evolutionary algorithms can be used to "learn" a control policy. It does this through an iterative cycle, where in simulation a control policy is run and evaluated, and this evaluation is fed back into the genetic algorithm so that it can improve the control policy. Evolutionary algorithms have the following advantages:

1. Complex, nonlinear control policies can be learned.
2. Underlying physics of dynamics does not need to be known.
3. Control policies can be learned from scratch or optimal parameters of existing control policies can be learned.
4. Distributed learning can be used to scale to larger tensegrities and to speed up learning.

Evolutionary algorithms can learn very complex, nonlinear control policies without the need to characterize the physics behind the control policy. Recent advances in distributed evolutionary algorithms applied to control tasks have produced robust learning algorithms that are a perfect match for tensegrity control [19, 25, 14, 76, 83, 80, 3, 79, 28]. Through these methods, each component can individually learn a control policy that decides how to actuate its individual node in such a way that global performance is maximized.

4.3.2 Control Based on Central Pattern Generators

Central pattern generators (CPGs) are neural circuits found in both invertebrate and vertebrate animals that can produce rhythmic patterns of neural activity without receiving rhythmic inputs. CPGs have been studied from a biological perspective and have been used extensively in robotics [29], especially for walking and other locomotion research (swimming, slithering, flying, etc). They use the term "central" to indicate that rhythms of the CPG are not driven by sensory input, but are self-generated. CPGs are the fundamental building blocks for the locomotor neural circuits both in invertebrate and vertebrate animals, and are also key to other fundamental rhythmic activities such as chewing, breathing, and digesting. In fact, recent research [18] has shown a close relationship between CPG's and motion primitives in the spine which enable both rhythmic and discrete motions. Besides the biological inspiration, CPG's present several interesting properties that are useful to robotic motion including distributed control, robustness to perturbations, the ability to deal with redundancies, fast control loops, and allowing modulation of locomotion by simple control signals.

The complex problem of agile locomotion of a robot can be greatly simplified if the structure and reactive controls of the robot provide a high level of locomotion competence. An inspiring goal is how decerebrated mammals can coordinate complex locomotion behavior without the involvement of their brains [62]. Due to the inherent uncertainty of operating in unstructured natural environments, modern robotic locomotion and manipulation research often focuses on compliant actuation. Tensegrity structures, which model the musculoskeletal system, extend this focus on compliance to the entire structure of the robot, providing desirable qualities such as variable stiffness, robustness to perturbations, and multi-path force distribution. Reactive controls draw

inspiration from numerous biological studies showing significant locomotor computation below the brain (for examples and reviews see: cockroaches [64], stick insects [12], and cats [84, 62]), we focus on maximizing the reactive competence of our robots by exploring the combination of compliant tensegrity structures with central pattern generator (CPG) controls [30]. A motivating intuition for pairing tensegrity robots with CPG networks is the similarity in the dynamics of physical forces propagating through a tensegrity structure with the dynamics of control patterns propagating through CPG networks.

Use of tensegrity robots for mobility was initiated in 2004-6 by papers from Masic [49], Aldrich [4], and Paul [60, 61]. Masic's paper included an analytical study of tensegrity based locomotion via periodic waves in a worm-like tensegrity robot; Paul demonstrated mobility both in a physics based simulator and on a hardware prototype. As a result of studies showing the prevalence of tensegrity structures in nature such as cell structure [31] and anatomy [42, 63], and the challenges of controlling tensegrity structures using traditional approaches, the majority of the works in mobile tensegrity robotics have shown biological inspiration in their motivation, using evolutionary algorithms [59, 60, 61, 65, 66, 67, 33], neuroscience inspired CPGs [8, 6, 7], and biomimetic structures such as manta-ray wings [51], or caterpillars [66, 57, 55, 56]. (See also [68, 70, 38, 9, 50] for other works on the locomotion of tensegrity robots) While some work has continued in the analytical understanding of the dynamics of motion for tensegrity mobility [24], the dynamics of contact with the environment are not considered. Since contact dynamics greatly complicate the already difficult task of controller design, most work resulting in simulated or hardware demonstrations of mobility are using non-analytical approaches. This started with Paul's [59, 60, 61] and Rieffel's [65, 66, 67] work which used evolutionary algorithms to discover controllers that resulted in slow crawling and hopping motions. This was followed by Bliss's work using CPGs to control the oscillatory motion of a robotic tensegrity manta ray wing for swimming [8, 6, 7]. Additionally, CPG-like equations have been used by Boxerbaum et al. to control a soft robot moving with peristalsis [10]. Boxerbaum's and Bliss' independent work both confirmed the validity of our approach to using CPGs to control mobile terrestrial tensegrity robots. Other work in our lab, not covered in this report, has also had great success at using CPG's to control the locomotion of a tensegrity inspired "spine" robot over a variety of terrains [78].

5 Summary of Key Findings

The purpose of our study was to validate that the concept of a tensegrity robot landing platform is feasible and useful for real NASA space missions. This validation consisted of three important parts: 1) Define a notional mission to Titan which would provide driving mission requirements for the engineering analysis performed in the later sections. 2) Show that the complexities of non-linear and oscillatory control of a tensegrity robot could be overcome through the use of genetic algorithms and central pattern generators, and 3) Show that in simulation and partially on a hardware platform that a tensegrity robot is in fact a good landing platform capable of surviving a hard landing, protecting its payload, and then act as a mobility platform. We are glad to report that our results exceeded all expectations, thoroughly validating the overall tensegrity robot and landing platform concept.

5.1 Define Notional Titan Mission and Requirements

Section 6 provides full details on our notional mission, which is summarized here. Titans atmosphere, stable bodies of surface liquid and complex organics make it one of the most complex and Earth-like environments in the solar system. This tensegrity probe mission will build on the science returns from Huygens and will answer many of the new and unresolved questions surrounding Titans ongoing organic processes, geologic history, atmosphere, and surface-atmosphere interactions. Upon arrival at Titan, the tightly packed tensegrity probes enter the atmosphere behind a heat shield until sufficiently slowed to avoid further thermal loads, at which point the heat shield is ejected and the probes separate and expand to fully deployed shock absorbing state. Without requiring parachutes or other landing device, each probe is projected to impact the surface at its terminal velocity on Titan at about 11 m/s, absorbing and distributing impact stresses while protecting its science payload. After the tensegrity probes bounce, roll, and finally come to a rest on the surface of Titan, the actuated tensegrity structure will then begin to function as the primary mobility system for these mobile probes. Once on the surface, a notional science payload containing an atmospheric package, an analytical chemistry package, and an imaging package can begin the probes science mission. Since each probe is equipped with a science payload, mission success is not entirely dependent on the survival of a single probe, and the deployment of only a few probes enables the distributed exploration of a planetary surface.

Our first analysis was to explore the possible packaging and deployment of the probe. We found that the basic structure could be fully flattened to a triangular shape with sides equal to the lengths of the rods. This approach leaves room in the middle of the payload, and can be fully deployed with actuated cables. Next, we investigated possible technologies to use for the three science packages: the atmospheric and meteorology package, the analytical chemistry package, and the imaging package. These were used to drive initial mass estimates and to scale the avionics, power, and structural support required for the mission. This resulted in an initial design that showed an overall system mass of 100kg, of which 70kg is productive scientific payload and associated avionics, while the remaining 30kg is dedicated to structure and actuation for deployment and mobility.

Using these numbers, we were able to show that an individual tensegrity probe has a significantly

lower EDL hardware overhead and increased science payload mass percentage when compared to similar planetary surface probe missions, increasing the potential for science return. We evaluate this by comparing the total system mass at the point of atmospheric entry with the mass of the rovers productive payload, which constitutes all the science instruments and associated avionics, power, and controllers. Compared with the Mars Exploration Rovers (MER) and Mars Science Laboratory (MSL) which had a science payload mass fraction of 18% for MER and 22% for MSL, we have shown that a tensegrity probe may be able to operate on Titan as a mobile probe with a science payload mass fraction of 50% due to the dual use of the tensegrity structure as for both EDL and surface mobility. While comparing Mars rovers to a Titan probe is not ideal, these are the closest existing missions which include surface mobility. Further analysis may drive this percentage higher as more efficient versions of the tensegrity lander are explored. By increasing the mass ratio of productive science payload vs total system mass, this approach helps drive down future mission costs by allowing smaller lighter missions with the full capabilities of EDL and surface mobility.

5.2 Developing Control Algorithms using Evolution and Central Pattern Generators

Sections 7 and 8 cover the controls work summarized here. Tensegrity robots have the potential to be fabulous mobility platforms as they can be light-weight, energy efficient, robust against failures, and can traverse across unfavorable terrains. However controlling these robots is difficult since there are many points of control, the controls interact in non-linear ways, and the structure as a whole is oscillatory. Using traditional control algorithms for mobile tensegrity robots is difficult and previous successful attempts have been limited to very slow static gaits, and evolutionary control of very simple structures. A real concern going into the Phase I study was that no reliable control could be found. Fortunately we have had tremendous success with evolutionary algorithms and later with dynamical and Central Pattern Generator based controls (see Figure 6).

We performed several tests of evolutionary control in a detailed physics simulation. Using open loop control, the evolutionary algorithm is able to find a control policy that allows the tensegrity robot to roll quickly in a smooth manner. These results were robust to adding small obstacles to the terrain and was even able to keep rolling after we cut one of the control cables.

The controls used by our evolutionary methods were a simple form of semi-distributed oscillatory control: All the actuations were controlled through sine waves synchronized through their relative phase shifts. These controls proved to be robust and sufficient for our goals of having our tensegrity platform roll smoothly. These controls also gave excellent examples and insight into what fundamental dynamics were required for fast smooth motion. On the other hand, these controls are open-loop and as a result, a major limitation of these evolved controls is that they do not provide a means to direct or steer the motion of the tensegrity probe. Rather, a control law is learned which can be abstracted, but which does not allow reactive changes of direction. To develop steerable controls we took the insights gained from the evolved controllers and hand crafted reactive dynamical controllers that used a variety of simulated sensor feedbacks to enable steerable rolling. This

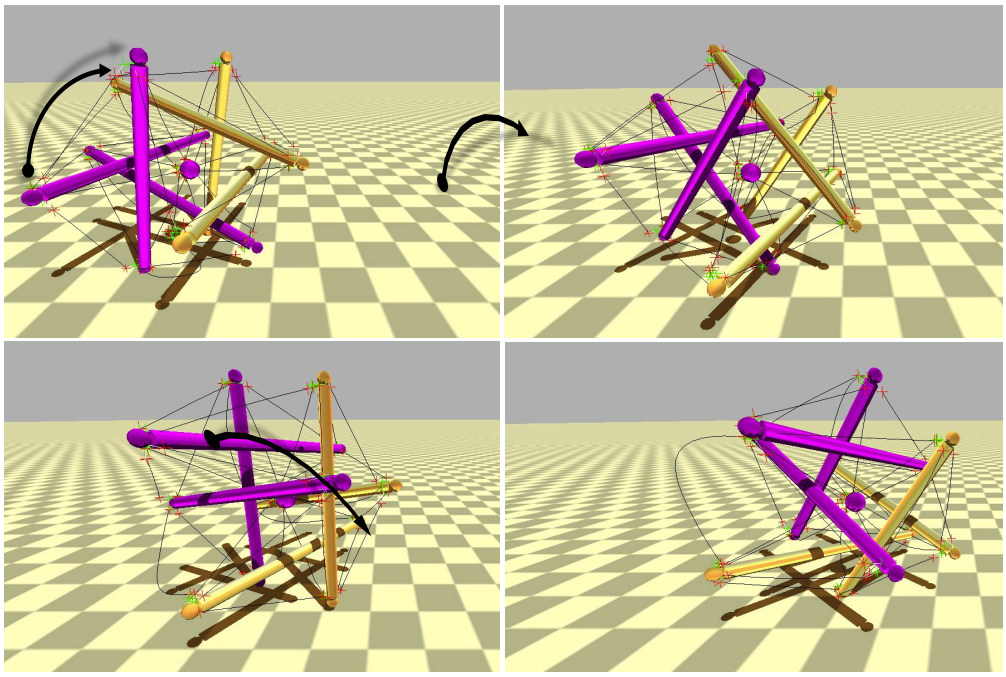

Figure 6: **Tensegrity Dynamics**. *Tensegrity is able to achieve smooth rolling motion. This rolling is accomplished solely by changing the length of the cables. Our learned control policies produce rolling that is also dynamical as the tensegrity does not stop to setup next roll action. This type of rolling can be fast and highly efficient.*

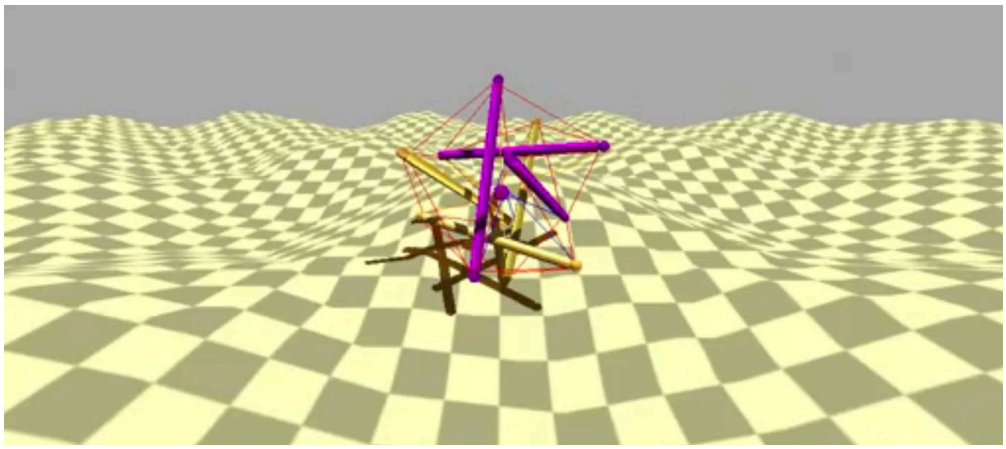

Figure 7: **Dynamical and Central Pattern Generator Based Control**. *Our dynamical controls allows tensegrity to climb over moderate hills.*

approach was very successful and was shown to work on a variety of terrains, including moderate hills (Figure 7). But, this approach relied on significant amounts of sensor feedback which may be difficult to implement, so we wanted to find a hybrid approach that enabled steering while using a minimum amount of sensor feedback. Central Pattern Generators (CPG's) are able to store complex gait cycles in their network dynamics allowing for a significant reduction of sensor feedback required. We explored a variety of ways to use this property and to combine it with aspects of the dynamical controls approach to enable steering. The best result found so far uses the hand-coded dynamical controller as a trainer to learn the parameters for a Hybrid CPG which combines Hopf oscillators and Inverse Kinematics.

5.3 Verification in Simulation and Hardware

Section 9 covers details of our hardware prototype, and Section 10 covers analysis, simulation, and actual hardware drop tests at Titan terminal velocity to confirm the possibility of using these structures for landing platforms. We believe that this is the first such analysis showing the characteristics of tensegrity structures during planetary landing. In all these experiments, our Phase I study verified the suitability of a tensegrity robot as a landing and mobility platform in the following three ways:

1. We verified that actuation for compact storage and deployment is possible in a hardware tensegrity probe.

2. We verified that our actuated prototype tensegrity probe remained structurally sound and could continue to operate after landing.

3. We verified that a tensegrity structure could protect a delicate payload, landing at impact speeds of 15 m/s (and possibly higher, pending future analysis).

Our first hardware prototype was built with hollow aluminum rods with the actuators mounted inside the rods for protection. The cables were a mixture of springs and high tension synthetic cables. This prototype was only partially actuated, with six motors, and was able to demonstrate shape change from a compact form to a fully deployed shock absorbing shape. With full actuation it would be able to achieve an even more compact shape when stored. To test the robustness of the design we dropped the probe 10m, as shown in Figure 8. Dropped from this height at earth gravity the probe landed at it's terminal velocity of Titan, and it easily survived the fall and was still functional afterwards, as was shown by its ability to still change shape between its collapsed and deployed states. A useful insight from this test was that the motors should have mechanical brakes on them for the landing impact, as they were slightly back driven during landing.

Since the first prototype did not contain a central payload, we also extensively analyzed how the landing forces would impact a payload in two simulators: our tensegrity simulator which uses the Bullet Physics Engine, and a hand-built Euler-Lagrange (E-L) simulator based on algorithms developed by Robert Skelton. We used these two simulators because they both have strengths and weaknesses. The Bullet simulator is the most general purpose, allowing us to explore control algorithms and complex environmental interactions, but it is an iterative discrete solver that we were

Figure 8: **Prototype drop test** *from 10m – about 14 m/s, greater than its terminal velocity on Titan*

concerned might not be providing accurate answers. The E-L solver, on the other hand, has a much stronger analytical basis and provides very accurate answers, but is limited because some of the nodes (i.e. rod ends) must be constrained and locked into place.

We first cross-validated these two simulation tools with each other and found that they predicted similar behaviors. We then performed initial cross-validation to motion control of a prototype tensegrities and found a reasonable match, giving us confidence in the accuracy of our modeling tools. Finally, we performed extensive analysis on drop tests and the protection provided to a payload. As expected, we found that by varying the rod lengths, which impacts the stroke distance for the payload to decelerate, we could control the maximum deceleration experienced by the payload while ensuring that it did not collide with the ground or structure. For example, with rods of 1.5 meters in length, our payload experienced a max deceleration of 21.4G when landing at 15 m/s. (See Figure 53).

These payload simulation results were supported by further drop tests with another prototype probe made of wood, plastic and elastomers. In this test, an egg was suspended in the middle of the tensegrity probe, which had no actuators, and was then dropped from a height of almost 10 meters without the egg breaking. The landing speed of the structure was thus about 14 m/s, and an egg can be expected to break at about 2 m/s, showing a significant amount of payload protection provided by the tensegrity structure, and providing support for the validity of our simulation studies. This probe also had a different morphology, a 30 strut dodecahedron, indicating that future work should explore the advantages of other shapes and configurations of tensegrity probes.

6 Tensegrity Probes for a Notional Mission to Titan

Based on their robust structural and control properties, we believe that tensegrity robots will have tremendous potential for numerous NASA robotics missions. In this section, we explore details of what such a mission would look like using a tensegrity robot mission to Titan as an example. In this example we will look at:

1. Approach vector and entry into Titan's atmosphere
2. Unpacking from aeroshell
3. Landing at terminal velocity
4. Instrument package weight and placement
5. Scientific goals
6. Comparison to traditional options for robotic missions

Note that this section is not meant to serve as a complete analysis of a Titan mission. Instead it describes how a tensegrity robot would be beneficial for such a mission. Likewise, while the Tensegrity Probes enable multii-robot missions due to their low weight and packing efficiency, we spend most of our technical analysis looking at a single robot mission in order to build the core knowledge required for a full multi-robot mission design effort.

6.1 Motiviation for Titan Mission

The success of the Huygens probe shed light on Titan's atmosphere and surface conditions which were found to have elements greatly similar to Earth and others vastly different. When it's substantial atmosphere is included, Titan is the largest satellite in the solar system. Titan's thick and very cold atmosphere is composed primarily of nitrogen with traces of methane, argon, and other hydrocarbon molecules. Observation of Titan has shown signs of a significant greenhouse effect, seasons, clouds, evidence of a methane-based hydrological cycle, and an extremely heterogeneous surface that includes methane-ethane lakes, dune fields, evidence of erosion, and possible evidence of cryovolcanism. The density of Titan is 1880 kg/m3, suggesting that it is composed of a 50/50 mixture of rock and ice. At the surface, the gravity of Titan is about 1/7th that of Earth, the pressure is about 1.5 bar, and the surface temperature is 94 Kelvins. With the cold temperatures, the surface density of the atmosphere is approximately 4 times that of the Earth.

In addition to methane, Titan's atmosphere also contains nitriles, more complex hydrocarbons, and aerosols formed from the nitrogen and the products of methane photolysis, and it is the precipitation onto the surface of these complex hydrocarbon compounds and aerosols that are the primary source of Titan's surface organics. Once on the surface, these organics can undergo further processing when exposed to brief periods of liquid water resulting from impact events or possible episodes of cryovolcanism. Although exposed water would quickly freeze over, calculations indicate that near surface pools of water could exist for thousands of years before freezing solid, providing time

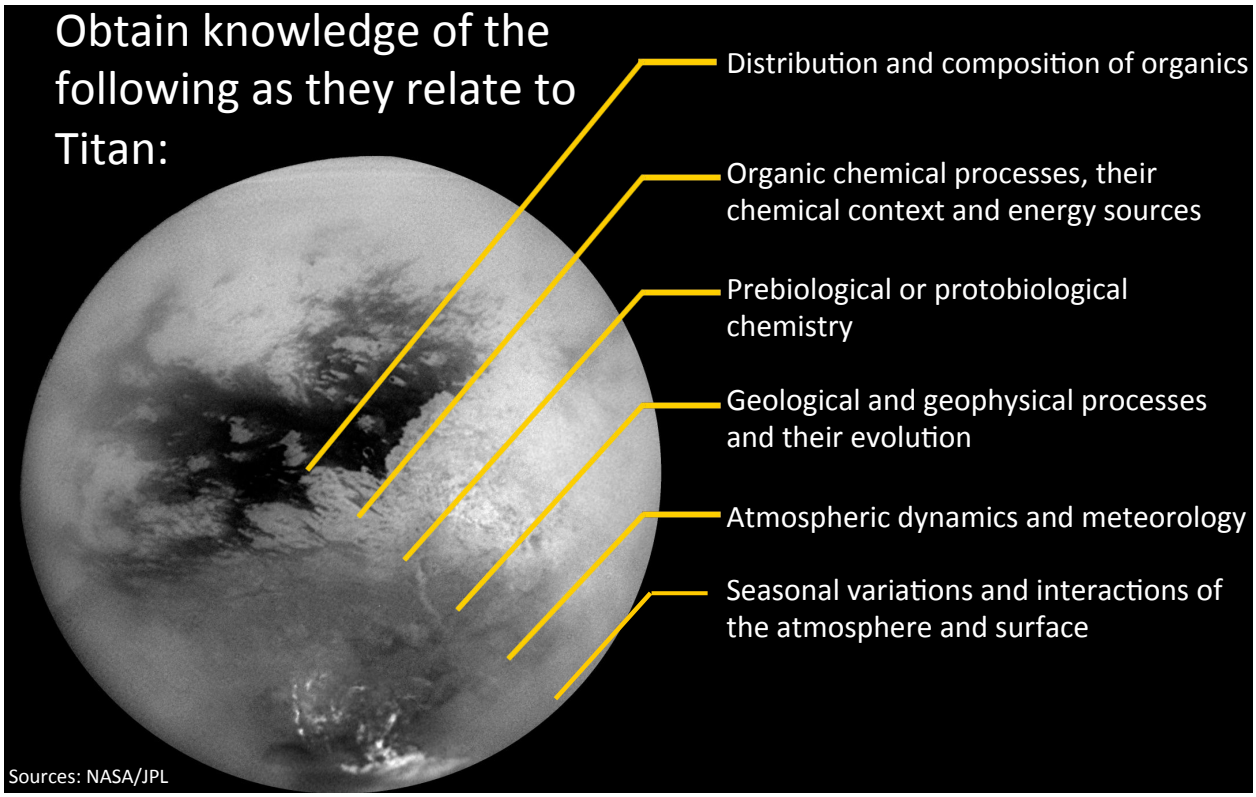

Figure 9: **Scientific Goals for Titan Mission**.

for nitriles and hydrocarbons to be modified by the brief presence of water into compounds with potentially important astrobiological implications including amino acids.

Since the products of complex atmospheric chemistries have precipitated to and been collected on the surface over geologic time, and since it is these products that form the basis of possible biotic and prebiotic chemistries, detailed studies of the chemical composition of the surface and subsurface of Titan are of high interest. In particular, regions of current and previous cryovolcanism and possible impact events are important since it is in these regions that material from the deeper interior of Titan may have found its way to the surface, and where episodes of liquid water in the geologic past are possible. To complement and build upon the remote sensing studies of Titan by Cassini and the in situ exploration by Huygens in 2005, it is important to explore regions of Titan that are geographically, topographically, and geologically distinct.

Along with this interest in possible pre-biotic chemistries in Titan's atmosphere, surface, and subsurface [88] there is also high interest in understanding the wide diversity of surface compositions, textures, and structures, including extensive dune fields and geologies due to fluvial and lacustrine processes, and surface reservoirs of liquid methane and ethane mixtures. Many of the surface features on Titan largely reflect sedimentary processes driven by Titan's surface-atmosphere interactions. As outlined by Barnes, et al. 2011, atmospheric haze is deposited onto the surface, and surface winds help create large dune fields. Evidence suggests surface erosion due to precipitation, and channel beds are carved by streams that carry sediments into the low-lying plains.

In recent years, many mission concepts for future Titan exploration have been studied and proposed, including TiME, TSSM, and AVIATR, and a number of specific Titan surface and atmospheric science goals have been defined including the source(s) of methane on Titan, and the origin and evolution of Titan's atmosphere. The most important science goals have focused on Titan's surface and subsurface and includes studies of the composition and distribution of organics, and potentially prebiotic chemistries involving organics and nitriles exposed to water. Although characteristics of the ethane-methane lakes and detailed studies of the geomorphologies and composition of the lake including suspended particles and properties of the lake sediments are likely beyond the scope of a tensegrity-based Titan surface mission, tensegrity probes can address many of the Titan surface and subsurface science goals and objectives by performing chemical composition and mineralogical surface and subsurface studies of many of the most important regions on Titan including dry lake beds, the shorelines of present day lakes, dune fields, streambeds and outflow channels.

6.2 Approach, Entry, Decent and Landing on Titan

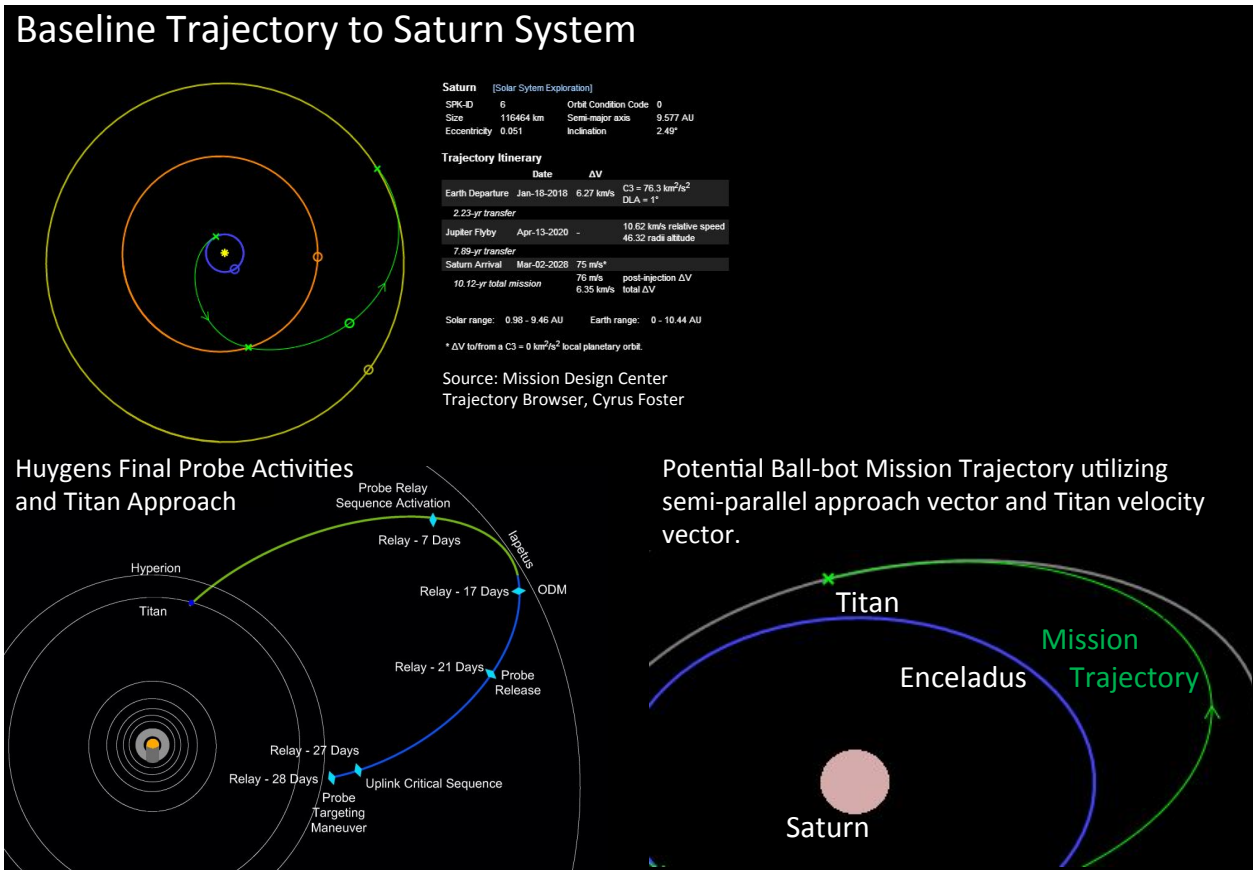

Figure 10: **Trajectory Analysis of Mission**. *Trajectory of tensegrity mission to Titan would be similar to Huygens.*

A planetary mission based on tensegrity robotics differs from traditional missions based on its unique unpacking, landing and mobility properties. We would therefore expect a total mission profile for a Titan mission to be similar to the Huygens mission for the approach and entry phase, but much different for the decent, landing and surface phase. The summary of our mission profile is as follows:

1. Enter Titan's atmosphere at 6.4 km/s after a 8-10 years in transit
2. Slow down in Titan's atmosphere using heat shield
3. Unpack and reach a terminal descent velocity of 11 m/s
4. Land at 11 m/s using the tensegrity structure to protect payload
5. Roll to lakeshore or other target destination to perform scientific measurements

6.2.1 Approach and Entry

As summarized in Figure 10 we expect the approach and entry profile to resemble the Huygens mission. Under this profile, the tensegrity robot would be packed into an aeroshell attached to a heat shield and would spend 8-10 years in transit, including a fly-by of Jupiter. After the conclusion of the approach, it would enter Titan's atmosphere at approximately 6.4 km/s. Upon entry, a thermal protection system (TPS) protects the tensegrity robot from the entry heat and dramatically reduces its velocity. For Titan missions, protection systems made from PICA, Tufroc, or heritage SLA are possible [40, 44]. Using these materials it is reasonable to have a TPS that weighs 40% of the weight of a single tensegrity robot. As will be discussed later, we have designed for a 100kg total mass for the tensegrity robot. Thus, including the heat shield, we estimate 140kg total system mass at the point of atmospheric entry for a system utilzing only one tensegrity robot.

6.2.2 Unpacking

Once the TPS has reduced entry velocity significantly, the tensegrity can then separate from the aeroshell and unpack (See Figure 11). For tensegrity structures built with elastic cables, this unpacking can happen automatically. Upon being released, such tensegrities would "spring" open. This form of unpacking can be especially advantagous if there are multiple tensegrity robots within one aeroshell. For non-elasticly packed tensegrities, unpacking can be performed through actuating the structure as shown in Figure 11 (right).

6.2.3 Terminal Velocity Landing

Upon release from the aeroshell most space probes need to reduce their velocity before landing. This is usually done with a parachute, possibly in combination with retro rockets. However, Titan's thick atmosphere and relatively low gravity could allow a tensegrity robot to land at terminal velocity without any additional hardware. This is possible since tensegrity structures 1) naturally have high drag, and 2) are able to withstand high impact landings. The high drag arises from the

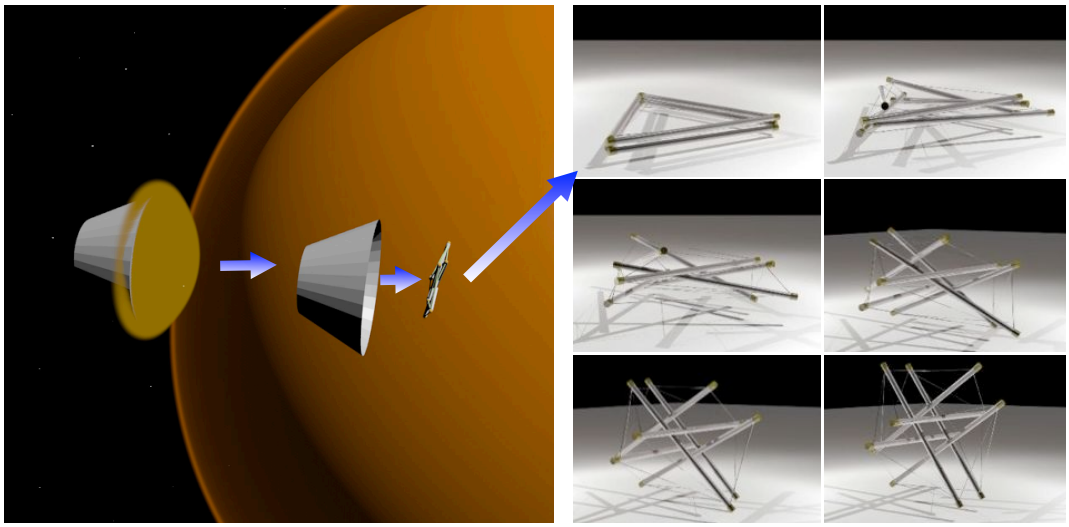

Figure 11: **Entry and Unpacking**.

use of rods and cables in the structure. The interwoven shape of the rods and cables causes them to induce chaotic flow and moderate velocities, therefore increasing drag. We tested the drag profile of a tensegrity structure by suspending it from a string and allowing the wind to drag it at a speed of 20 miles/hour (8.9 meters/second) as shown in Figure 12 (Left). From the angle of the string we determined that the tensegrity had a drag coefficient of approximately 0.5. From this drag profile, we calculated the speed we would expect a tensegrity to have versus altitude after entry into Titan's atmosphere. From results shown in Figure 12 (Right) we conclude that a tensegrity robot would have a surface impact speed of approximately 11.4 m/s even when no parachute is used. Our landing analysis described in detail in Section 10 shows that a tensegrity robot should be able to survive and protect a delicate payload when landing at such velocity.

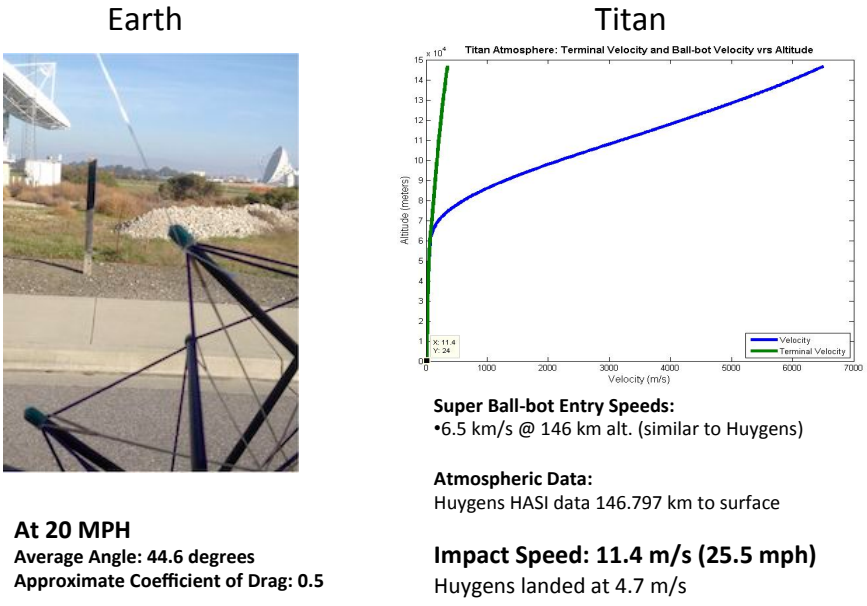

Figure 12: **Terminal Velocity Analysis**.

6.3 Mobility

Once the tensegrity robot has landing it can move to locations of interest. Due to its elastic oscillatory nature and its ability to give and take energy, it is likely to be able to move in an energy efficient way by rolling (results in Section 7 have shown that we can create control policies that allow for smooth rolling motion). The need for mobility is essential if several different surface locations need to be examined. In addition, even if only a single point of interest exists, mobility may still be essential since landing mechanisms may not be accurate enough to land in exactly the desired spot, or the point of interest may be in a location where landing is hazardous. One such location is likely to be near the lake shore of Titan. In such a mission, landing too close to the lake would be hazardous since the robot may land in the lake itself. Therefore in such a mission the tensegrity robot could land a safe distance from the lake, and then roll to its shore as shown in Figure 13.

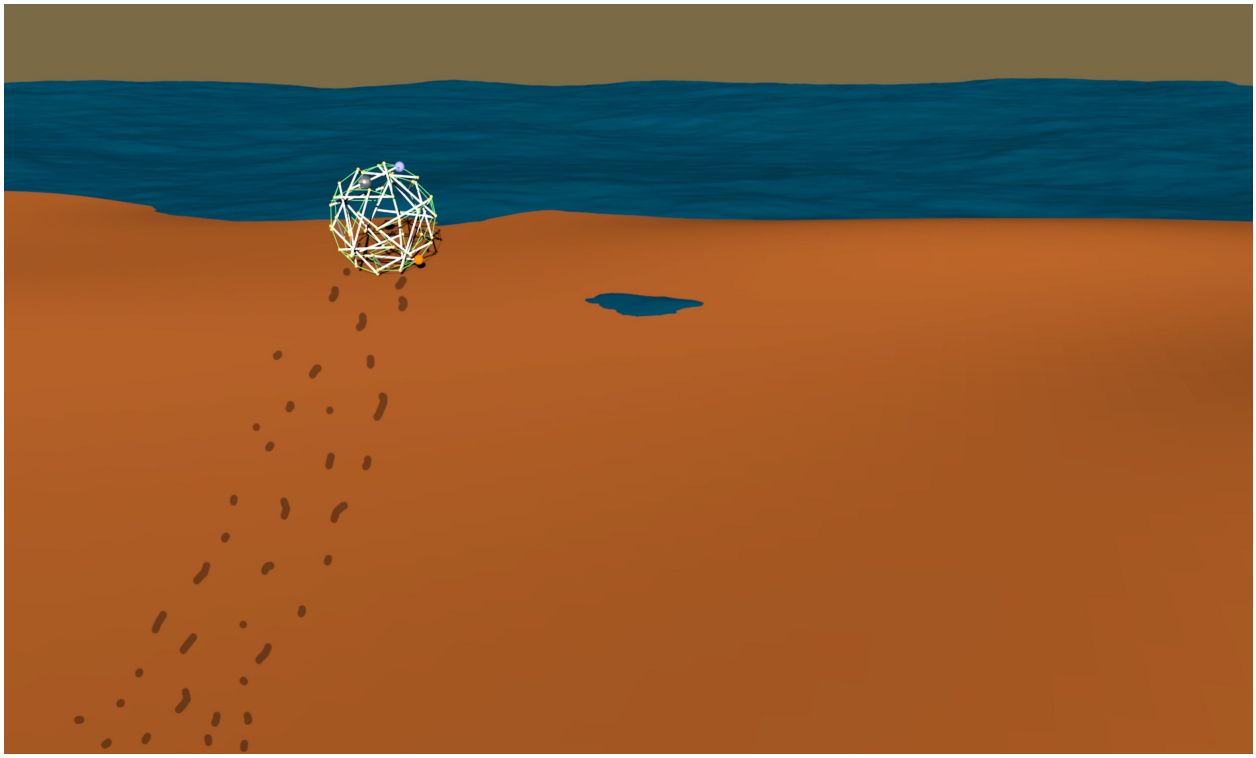

Figure 13: **Tensegrity Robot Moves to Lake Shore**. *The tensegrity is both a landing and mobility platform. After a terminal velocity landing, the tensegrity can move to desired areas of interests such as a lake shore.*

6.4 Scientific Study of Titan's Surface and Instrument Packages

Titan is a volatile rich, chemically active moon with a complex methane cycle. Dunes, craters, fluvial valleys, and lake shores are among the primary target sites for future Titan missions. While a tensegrity platform can potentially be used on all these sites, here we focus on lake shores since they provide a high scientific return do to the interaction between a liquid and solid surface, and the

atmosphere. We also focus on lake shores because these areas are difficult for traditional robotics due to the hazards of landing and navigating close to the lake shore, e.g. move on slippery terrain that could be hazardous to a traditional wheeled robot. Our notional mission will look closer at the mineralogical constituents of the surface, search for examples of prebiotic chemistry and its evolution on Titan and monitor variations in the meteorological cycle over a longer period and greater geological region than the Huygens probe.

To complete these tasks, we selected a notional set of instrument packages for this mission to support the fundamental science objectives of a future Titan tensegrity Mission. After an extensive literature search we selected a number of individual instruments which appeared to be of the appropriate science, mass, power, and data rate. Our main objective in this effort was to derive a notional payload mass that could be used as a requirement for further engineering and analysis of the mission and tensegrity robot technologies. Since we are designing for a future mission dependent on the development of novel tensegrity technologies, we also selected instrument concepts which are themselves under development and have not yet necessarily been flight qualified. Our instruments are:

- **Analytical Chemistry Package**, containing a Gas Chromatograph and a Mass Spectrometer [17].
- **Atmospheric and Meteorology Package**, containing instruments to measure Temperature, Wind Speed, and Methane Humidity [23].
- **Imagery Package**, containing Navigation Cameras and a Field Microscope [47, 27]

The analytical chemistry package will provide detailed analysis of the organic molecules present on the surface. Sites on Titan's surface where complex organic chemistry can produce and sustain organic molecules may provide an insight to prebiotic chemistries within the solar system. Determining the presence of organics and their make up on Titan's surface can also yield information about the processes and interactions which produce favorable or non-favorable conditions for organic chemistry in extreme environments.

The tensegrity robot for our notional mission will be equipped with an atmospheric and meteorology instrument package which will continuously monitor temperature, pressure, wind speed, and methane humidity as the tensegrity robot travels across Titan's surface. Operating on a continuous basis, the atmospheric and meteorology package will be one of the largest generators of data from the surface. The atmospheric and meteorology package will measure diurnal and possibly seasonal changes in temperature, wind speed and directory, and methane humidity variations at many locations across the surface, allowing for the identification and monitoring of local weather systems. A key data point will be the amount of methane precipitation recorded at the surface and its frequency. To begin understanding Titan's complex atmosphere requires surface measurements over large distances and times.

The Imaging package will consist of both a NAVcam and a field microscope to be used in a variety of surface operations. The tensegrity robot NAVcam will be similar to the Mars Exploration Rover

(MER) NAVcams with new larger heating elements to handle the harsh Titan environment and will be used to navigate the varied surface [46]. As the primary visual sensor, the NAVcam will also monitor the terrain surrounding the tensegrity robot for interesting surface structures. Using advanced image processing techniques which integrate with the accelerometers, a stable camera view can be generated even as the robot is rolling by selecting appropriate image frames maintaining a stable view of the horizon. Interesting surface structures can be further investigated using the field microscope, also part of the imaging package, located within the center payload. The tensegrity robot upon identifying a specimen worthy of further study, will use a field microscope instrument similar to the Microscopic Imager (MI) used on MER to acquire images at a spatial resolution of 30 microns/pixel over a broad spectral range (400-700 nm) [26]. Using the entirety of the tensegrity robotic structure and its ability to deform and adjust its shape to suit its environment and current tasks, the field microscope can be precisely positioned above the surface. When these detailed images are received and analyzed by planetary scientists and geologists on Earth, the mission science team can command the tensegrity robot to return to the region from which the image was taken or continue searching autonomously. This autonomous search and survey operation consisting of a visual search along a travel vector and in depth microscopic study, should a scientifically interesting specimen be identified, suits the mission's logistics and the tensegrity robot's capabilities.

6.4.1 Mass Analysis

For the tensegrity mission to be cost effective our overall weight must be low. Yet we must still have enough instruments for high scientific return. Our goal in instrument choices is to make a good balance between these competing requirements. Figure 14 shows the expected weight of the components of our mission, and the overall weight. While it is difficult to estimate the masses and capabilities of future instruments, for this study we determine the mass of the payload of the tensegrity robot by referencing the mass parameters of instrument, communications, avionics and power distribution subsystems from other planetary exploration missions. The mass of this operational science payload is used to determine engineering aspects of the tensegrity structure parameters, mission design, and mission operational scenarios, such as actuator strength and material properties. The notional operational payload is estimated to be 70 kg, including science instruments and support avionics and power. Given the operational payload mass, the tensegrity support structure and its actuators which weigh approximately 30 kg combined, the entire vehicle is estimated be 100 kg.

6.5 Tensegrity Probes in Comparison to Other Flown Missions

For more than 20 years NASA's Discovery program has funded low cost, highly focused missions demonstrating new technology and seeking out the answers to fundamental questions regarding solar system formation, potentially habitable environments, and potential locations within the solar system where life could begin and evolve. The program has many successes, amongst them the Mars Pathfinder mission which deployed a Mars rover called Sojourner, NASA's first rover on Mars [22]. A tensegrity based probe mission to Titan can be compared to other Discovery program missions due to it's demonstration of new EDL technology and focused science objectives.

Notional Mass Properties for a Tensegrity Probe:

Probe Subsystem:	(kg)
Tensegrity Structure and Actuation Hardware	30.0
Avionics	23.1
Communication	6.0
Electrical Power Subsystem	36.0
Imagery Package	0.7
Meteorology Package	1.4
Analytical Chemistry Package	2.8
Total	100.0

The notional scientific payload for a tensegrity probe mission will have three science packages:

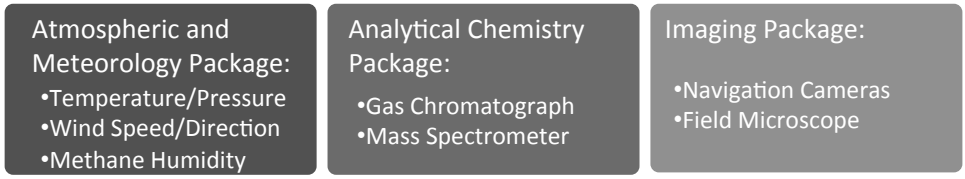

Figure 14: **Notional Mass Properties of a Tensegrity Probe**. *References: Avionics [15], Communications [15], Imagry Package [47, 27], Meterology Package [23], Analytical Chemistry Package [17].*

A primary goal of the mission is the demonstration and validation of the tensegrity structure as capable EDL equipment and primary mobility equipment. Using a tensegrity structure in this way enables the tensegrity probe to comprise a larger percentage of the entry mass than other missions such as Pathfinder, the Mars Exploration Rover missions, or the Mars Science Laboratory mission. When compared with the Mars Exploration Rovers which had an entry mass of 830 kg, of which 146 kg of equipment directly supported instrumentation and scientific study, the tensegrity probe represents the entirety of the planned landed mass and will not have to discard any hardware before initiating surface operations, other than a heat shield for initial entry. Based on Titan heat shield studies which show that it would be reasonable to assume 35-41% TPS/probe mass using PICA, Tufroc, or heritage SLA, we assume 40kg of heat shields required for a single 100kg probe. After slowing to terminal velocity and discarding the heat shield, a tensegrity probe is capable of landing and carrying a center slung payload weighing as much as 70 kg as it travels across the surface of Titan. This payload will contain all science instruments and payload support equipment. Thus, as can be seen in Table 15, the tensegrity probe enables a mission to dedicate 50% of the entry mass to productive science equipment whereas Pathfinder delivered 1% science payload, MER's was 18%, and MSL provided 22% of its entry mass as productive payload. Since mass is a driving aspect of mission cost – driving everything from launch vehicle to the interplanetary vehicle and fuel requirements, we believe that enabling better science payload to entry system mass will help drive down future missions costs.

	Pathfinder	MER	MSL	Huygens	Tensegrity
Entry Mass (kg)	587	831	3301	320	140
Landed Mass (kg)	372	540	943	223	100
Rover Mass (kg)	11	175	943	0	100
Science Payload and Support Avionics (kg)	8	146	723	223	70
Productive Science Mass Percentage	1%	17%	22%	69.7% No Mobility	50%

Figure 15: **Planetary Exploration Missions by Mass**. *References: Pathfinder [54], MER [54], MSL [41], Huygens [15].*

7 Evolutionary Controls

In this section we explore the use of Evolutionary algorithms to develop controllers for surface mobility of the tensegrity probe once on Titan. Evolutionary algorithms, genetic algorithms and reinforcement learning are all part of the broad field of machine learning that can be applied to sophisticated control problems. What makes these algorithms unique is that the control solution is not created in a top-down manner, but is instead "evolved" or "learned." These methods of controls are ideally suited for control problems that exhibit complex and non-linear characteristics making it difficult to apply traditional control algorithms. In this report, we describe how we successfully applied "evolutionary" algorithms to the task of controlling a tensegrity robot. The evolutionary aspect comes from our use of a population of control policies that is then slowly evolved to create populations of higher and higher performance. Note that this work does not exclude the possibility of using reinforcement learning for this problem, which would involve the tensegrity robot exploring the environment and learning to improve its control policy through negative and positive rewards.

7.1 Target Tensegrity Platform

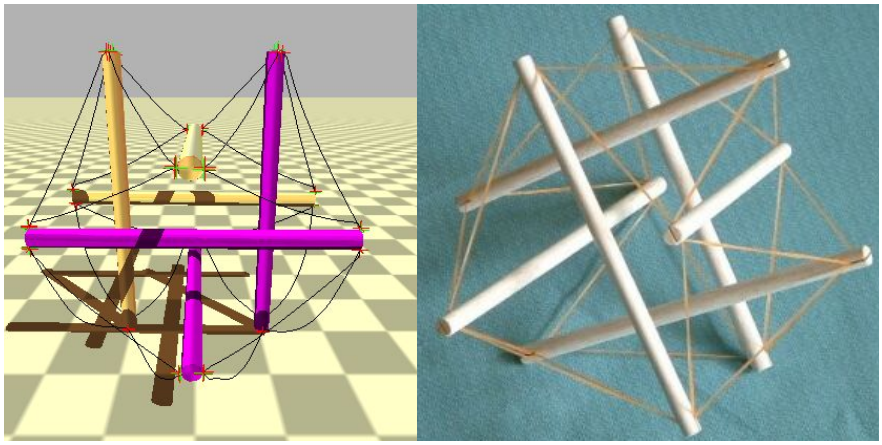

Figure 16: **Structure for Tensegrity Robot.** *This six-rod design is one of the simplest designs that can behave as a "ball." It is capable of rolling, changing shapes, and can be robust against failures.*

Our experiments for evolutionary controls of a tensegrity robot involves our basic "6-bar" tensegrity used throughout most of this report. This platform has 6-rod and 24-cable tensegrity as shown in Figure 16.

7.2 Tensegrity Actuation

The tensegrity is controlled by changing the lengths of the cables. Many hardware implementations do this by using a motor to wind the cable onto a spool that is either interior of the tensegrity structure or inside a rod. Other concepts involve using dynamic cable twisting or elastomers to

change the length of the cable. In this section we do not consider the hardware implementation, though we do limit our abstract model of actuation to reasonable performance characteristics for velocity, acceleration, and string elasticity.

The control of the robot is done via sinusoidal control of the lengths of the cables. The lengths of the cables change over time according to a sinusoidal signal, and the parameters of the signal are the output of the evolutionary algorithm. The length of each cable is calculated with the formula:

$$y(t) = C + A * sin(\omega t + \phi) \tag{1}$$

where,

- C represents the center position of the sine wave.
- A, the amplitude, is the peak deviation of the function from its center position.
- ω, the angular frequency, is how many oscillations occur in a unit time interval
- ϕ, the phase, specifies where in its cycle the oscillation begins at t = 0.

By using 24 sinusoidal signals for 24 cables, overall control of the tensegrity is based on 96 $(24 * 4)$ parameters.

7.3 Simulation

Our tensegrity simulator is built on top of the open-source Bullet Physics Engine [11]. Bullet was chosen because of its support for soft-bodied physics, and has been used previously in tendon-driven robotics simulators such as Wittmeier et al's CALIPER software [85]. We keep our model of actuation abstract in order to explore the best control solutions and then drive requirements back into real hardware design requirements. To enforce additional realism, we prevent the cables being actuated when stretched more than 25%, as an upper limit on the hypothetical motor force. This approach allows us to find the types of control and requirements that will be driven into actuation selection.

Due to limitations of the physics engine at the time the analysis in this section was performed, we scaled the parameters in the simulator by a factor of 10 such that the simulated 1 meter tensegrity structure had a size of 10 meters for each rod. This scaling was required because Bullet at the time was more numerically precise for larger objects. Thus, distances and velocities reported in this section should be scaled down by a factor of 10 to represent sizes and speeds more appropriate of tensegrity robot with 1 meter rods. Thus, when we report in this section that the robot moved 900m in 60 seconds, one can scale that to 90m in 60 seconds for a 1-m tensegrity. We later developed a better approach to the simulater such that all the other results in this report do not require this extra scaling factor.

Also, at the time of the experiments in this section, we were still using the built in soft-body cables which are represented as nodes with Hooke's-law-like stiffness between them. Therefore

our "cables" are actually somewhat elastic and exert a force dependent on their length. We later found that this approach was adding some undesired dynamics. Thus, we later built our own improved cable model (which has since been cross-verified in multiple ways), and so other sections in this report use that improved model. Recently, we reran some of the experiments reported in this section, using our improved scaling approach and new cable models, and found reasonably similar results (See section 7.9.5), providing validation for the work presented here at the scaled size and using the older cable model.

7.4 Evolutionary Algorithms

While the control parameters of our tensegrity platform are relatively straightforward, the relationship between these parameters is highly complex. In this section we explore how we can use the simulation combined with a fitness evaluation to implement an evolutionary algorithm that can evolve a set of control parameters that leads to the desired behavior.

7.5 Evaluation Function

We measure the performance of a simulated tensegrity based on how far it can travel from a starting location within 60 seconds using the following fitness equation:

$$f = d(C_1, A_1, \omega_1, \phi_1, \cdots, C_{24}, A_{24}, \omega_{24}, \phi_{24}) \ , \tag{2}$$

where, d is the distance travelled, which is a function of the 96 parameters of the control policy. Note that the decomposition of the distance function d is not readily obtainable in closed form. Instead it must be computed from observing simulations or measured from a physical implementation. Also note that our evaluation does not explicitly take any behavior into account besides distance moved. Tensegrities can exhibit many different gaits, ranging from hopping to rolling, and many different paths, ranging from spirals to straight lines. However, tensegrities that maximize our fitness function tend to roll in fairly straight lines. Deviations from this pattern tend to hurt performance.

7.6 Centralized Evolutionary Algorithms

In this paper, we perform both centralized evolution and multiagent coevolution. In the centralized case, a single control policy is evolved for the entire tensegrity robot. This control policy sets the 96 parameters for the sinusoidal controllers. The algorithm is a simple evolutionary algorithm designed to maximize our fitness function. At the beginning of training, a population of n random policies is created and evaluated based on our fitness function f. After each round of evolution, the worst k policies are removed, and are replaced by mutated versions of the best k policies. Mutation is uniformly random for each parameter. For experiments that use crossover, we use a simple basic single point crossover. In the simple single point crossover, new k policies get coupled, and each couple switches the second part of the parameters after a randomly selected parameter between 1 and 96. In both cases, as evolution progresses, the population tends to converge to higher performance policies.

7.7 Cooperative Coevolutionary Algorithms

While centralized approaches often produce good results, evolving a centralized controller can be slow due to the size of the search space. If the control parameters are tightly coupled, then the centralized approach may be the best we can hope for. However, control of a tensegrity robot is not necessarily tightly coupled. While changing the length of a cable will strongly affect neighboring components, it will have less of an effect on components on the opposite side of the tensegrity. Therefore decentralized control is possible and can greatly reduce the search space for each component in the decentralized controller.

In this paper, we introduce such a decentralized controller as a cooperative coevolutionary system, using principles derived from multiagent systems. In this paradigm each of the 24 cables is controlled by an individual agent. The job of each agent i is to control the four parameters of the sinusoid controlling its cable: C_i, A_i, ω_i and ϕ_i. To do this, each agent i will have its own population of control parameters, p_i, where each member of the population, $p_{i,j}$ specifies the four control parameters. Each agent then evolves its population to produce good values of control parameters in the context of the control choices of the other agents. The goal of these coevolutionary agents is still the same as the centralized evolutionary algorithm: Maximize the global fitness evaluation, f.

The advantage of this paradigm is that each agent now only has to search through four parameters. The difficulty is the value of each agent's choice of control parameters now depends on the choices of the other agents. The exact same choice may be good or bad, depending on what other agents are doing. One way to address this is to evaluate every possible team existing at the current generation. In this paper, this is not possible due to the number of possible cooperators. We attempt to handle this issue by taking a fixed number of samples of the population at each generation of evolution. Between two generations, each agent's population is sampled s time and they are put together to form s complete control policies. Each of these control policies is then evaluated with respect to our global fitness evaluation function, f, producing s evaluations. Typically the number of samples s will be many times larger than the size of the population, therefore each individual member of a population will typically be part of multiple control policies. The main issue now is how we evaluate a member of a population $p_{i,j}$ which has participated in multiple control policies, when each control policy has received a different global fitness evaluation f.

In this paper, we address this issue in the following three ways:

1. Generational Average - Assign the mean value of the global fitness evaluations for control policies in which the member participated during this generation.
2. Leniency - Assign the highest value of the global fitness evaluations for control policies in which the member participated in.
3. Historical Average - Assign the mean value of global fitness evaluations, averaging across all the generations that the member survived.

Taking an average and Leniency are commonly used methods with cooperative coevolution [58]. To improve performance, we augment this approach by taking historical averaging. Historical av-

eraging uses all the samples that the members had been part of, not only the current generation but also the ones with previous generations with previous teammates (Algorithm 1). Every surviving agent carries its history to the new generation and uses that information to calculate its average score.

Algorithm 1: Cooperative coevolutionary Algorithm with Historical Average

Data: Population of n elements for each agent
for *i=1..15* **do**
    random team $\leftarrow \emptyset$;
    forall the *Populations* **do**
        random team $\leftarrow$ random agent;
    end
    score = evaluate random team ;
    forall the *agents* $\in$ *random team* **do**
        agent.history $\leftarrow$ agent.score ;
    end
end
forall the *Populations* **do**
    forall the *agents* **do**
        agent.fitness = average(agent.history) ;
    end
    order the population;
    eliminate last k;
    copy first k to last k;
    set score of last k to MIN;
    mutate last k;
    clear history for last k;
end

7.8 Hand-Coded Solution

In addition to creating control policies through evolutionary algorithms, we explored how to hand-code a control solution using the same parameters available to the evolutionary system. The goal here is to explore the challenges of hand-coding a solution and to see how well our best effort compares to our learned solutions. It turns out that creating a control policy by hand using our 96 parameters is extremely difficult, so we created 8 control groups with 3 cables in each group. These 3 cables form a triangle that have the same length, making it easier to write a hand-coded controller. Even with this simpler approach, the best achieved solution barely moved. This problem will only get more difficult as we scale the tensegrity robots to more complex versions with more elements. To improve performance, we reduced the parameter space by hand coding the amplitudes of each group and making the oscillation frequency the same for all groups. The results shown later in this paper are for this second, better-performing hand-coded solution.

7.9 Experimental Results

In this section, we present experiments evaluating the performance of our evolution-based methods to control tensegrity robots in the physics simulator described in Section 7.3. The goal of our experiments is to evaluate whether evolutionary systems can be successfully applied to tensegrity robots under nominal conditions, and how robust these solutions are to limitations in the range of actuation, to actuator noise and to a physical breakage in a cable of the tensegrity. For the nominal condition case we test the following methods of creating the controller:

- **Hand Coded**, Control policy is developed by hand to try to achieve maximum performance.
- **Centralized Evolution**, A single control policy is learned for the entire tensegrity robot.
- **Decentralized Evolution**, Cooperative Coevolutionary Algorithms (CCEA) approach.

We then test different fitness methods for CCEAs: Average, Leniency, Historical Average. We test the robustness of our highest performance solution (historical average) in the following ways:

- **Actuation Noise**, We add noise to how far cables are actually moved as compared to how far they are being requested to move.
- **Cable Failure**, We test performance when a single cable in the robot breaks.
- **Obstacles**, We randomly place half sphere obstacles into the environment.

All experiments start with a stationary tensegrity robot on the ground. For each experiment, the robots are created on a flat surface, and after 5 seconds of stabilization time, active control of the cables starts. The agents are given a fixed amount of time (60 seconds) to move the robot as far as possible. The evaluation function is the distance between the starting position and the position at the end of the given time period. The population size in the policy search is set to $n = 10$ and the selection parameter is set to $k = 5$. We perform 10 statistical runs for each type of experiment. Using a t-test we confirm that our conclusions are statistically significant.

7.9.1 Centralized, Decentralized and Hand-Coded

The first experiment compares three different control policies: Hand-coded, centralized evolution and multiagent evolution. Figure 17 shows that both evolution-based approaches can easily outperform the hand coded solution. The multiagent evolution approach provides the best performance by moving 100% more quickly than the single agent and 400% more than our hand coded agent. Both centralized and decentralized evolution are able to achieve smooth rolling motions as shown in Figure 20. Note that while our hand coded tensegrity is not able to achieve a rolling motion, we are not trying to imply that this problem is impossibly complex for non-evolving algorithms. In fact there have been several successful algorithms to do this [69, 39, 82, 13]. Instead we are illustrating that it is in fact quite difficult to create these controls, and that the centralized and multiagent evolutionary algorithms are creating complex, non-trivial control solutions. In addition a multiagent framework has the potential to be adapted to many different complex tensegrities with

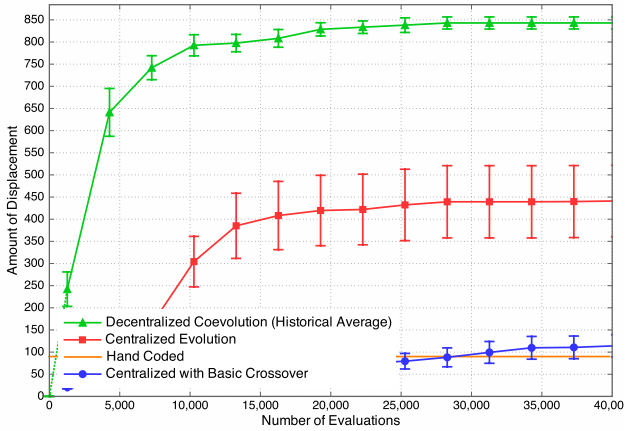

Figure 17: **Performance of Control Algorithms**. *Multiagent coevolution performs significantly better than other methods since it is able to take advantage of distributed nature of tensegrity control.*

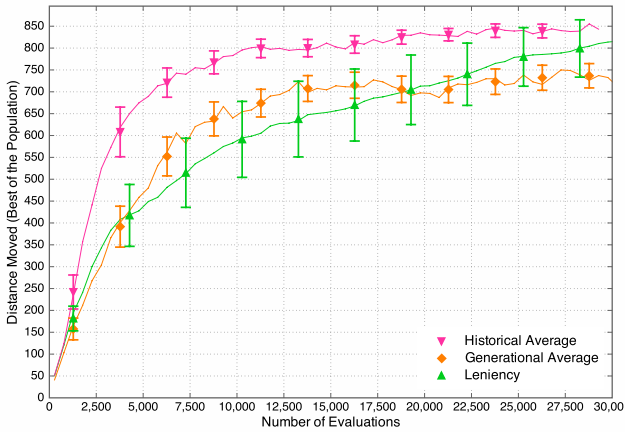

Figure 18: **Evaluation Methods**. *Using a historical average reaches best score and it is consistent. Lenient learners have bigger error bars.*

less effort than hand coding an algorithm for each new tensegrity.

It can be seen that the tensegrity controlled by policies evolved from coevolution reaches a performance around 900 meters in 60 seconds. By observing the behavior, we confirmed that the movement is established by smooth rolling motion as illustrated in Figure 20. This rate corresponds to the tensegrity moving at approximately 28 revolutions per minute. This result is independent of the size of the tensegrity. Therefore we would expect a 1 meter diameter tensegrity to move at approximately 90 meters per minute.

7.9.2 Historical Average, Average and Leniency

The second experiment compares different fitness assignment methods for CCEAs. As it can be seen, using a historical average performs better than every other method. Moreover, the small error

bars signifies that using the historical average consistently provides similar performance . Looking at the error bars of the lenient learners, it can be seen that standard deviation is high: It also reaches very good policies in some of the statistical runs, but the average success is lower.

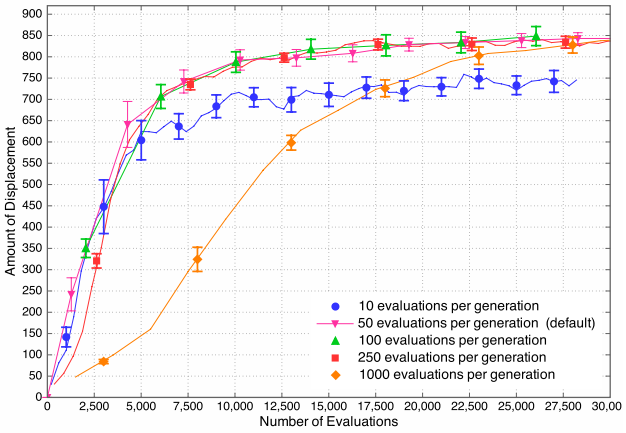

Figure 19: **Sample Size**. *Taking more samples for each trial improves stability but takes more time reach better behavior.*

To make sure that the sample size that we chose does not significantly affect the results, we tested the historical average method with different sample size between each generation (s). Figure 19 shows that the sample size affects performance when it is too low such as 10, on the other hand, a sample size as high as 1000 decreases the learning speed. Considering this result, we used 50 as the default value for the rest of the experiments.

7.9.3 Actuation Noise

To measure the robustness of our evolutionary algorithm against noise, we test the multiagent tensegrity robot in an environment with different levels of actuation noise. Actuation noise is applied at every time step to the sine wave that the evolutionary algorithm generates which control the cables. At every time step, noise is directly added to the value of the Equation 1. To test different levels of noise, we use different environments where the standard deviation of the noise is set to $1\%, 2\%, 5\%, 10\%, 25\%, 50\%, 100\%$ of the amplitude of the sine wave for each cable.

In this experiment, we test two different policies in our noisy environment: 1) Policies from a multiagent system that had learned in an environment without noise, and 2) Policies that are learned in an environment with the same amount of noise they are tested in. Figure 21 shows that tensegrities trained both with and without noise can perform remarkably well when the level of noise is below 15%. This is an impressive result, as it shows that the solutions generated in a non-noisy environment are not highly specific to an exact model of a tensegrity and exact environmental conditions. Instead the solutions appear highly generalizable. Beyond this level of noise performance goes down significantly. However, while performance is low, a tensegrity trained with a high level of noise can still perform at a base-line level while subjected to high levels of noise, which could be very useful in many situations.

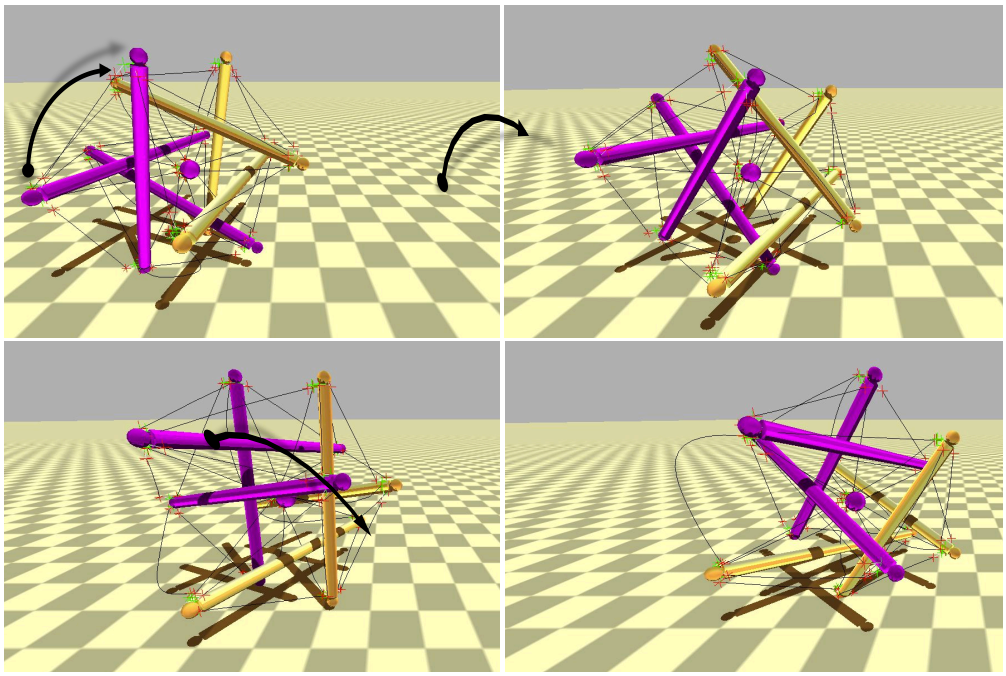

Figure 20: **Tensegrity Dynamics**. *Tensegrity is able to achieve smooth rolling motion. This rolling is accomplished solely by changing the length of the cables. Our learned control policies produce rolling that is also dynamical as the tensegrity does not stop to setup next roll action. This type of rolling can be fast and highly efficient.*

7.9.4 Broken Cable and Obstacles

In this section, we tested the robustness of the structure and the controller. Our first experiment was to remove one of the cables, which decreases controllability and also disrupts the balance of the structure. With the cable removed, the structure is no longer symmetrical and it can not keep its ball shape by default. In our second experiment we place the normal tensegrity in an environment containing randomly placed half sphere obstacles. When we test our best policy trained in a perfect environment in these two conditions, the performance drops to 50% with obstacles and it cannot roll with a broken link (Figure 22). On the other hand, if we perform evolution in these conditions, the evolutionary algorithm can still find successful locomotion policies for a tensegrity with broken cable, or in an environment with obstacles.

This result shows that under adverse conditions we can evolve a controller that takes advantage of the large range of motion inherent in tensegrity robots to effectively maintain locomotion. Note that this result does not show that the evolved control policy dynamically adapts to problems, since in this experiment we retrain our policy after the breakage. However, it does show the flexibility of the evolution process and the ability to pre-evolve controls associated with potential failure modes.

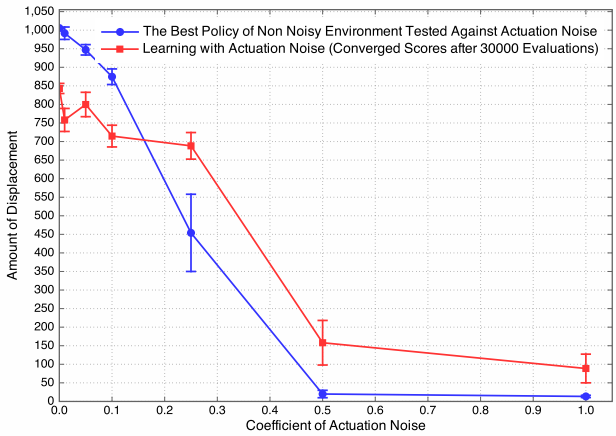

Figure 21: **Actuation Noise**. *The best policy can take up to 25% noise, evolving in a noisy environment scores better in higher noise environments.*

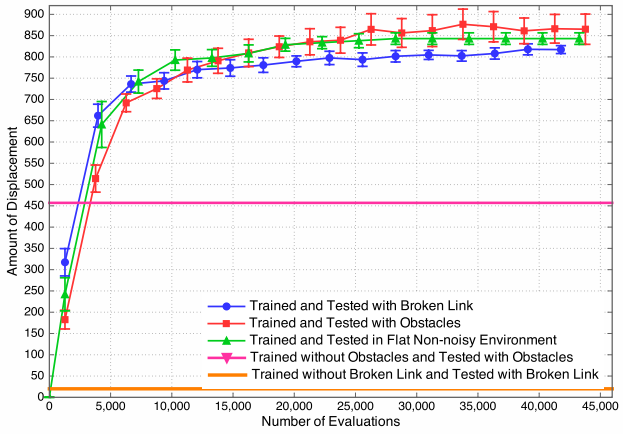

Figure 22: **Robustness Tests with Obstacles and Broken Link**. *Coevolutionary Algorithms can overcome both obstacles and broken link scenarios.*

7.9.5 Updated Analysis Using 1.0 Meter Rods

As mentioned at the start of this section on evolutionary learning, when we ran these experiments we were scaling our simulation world for numerical reasons such that we used rod lengths of 10 meters. Later in the project we developed a better way to work with the simulator without requiring that rescaling. We also discovered that the built in soft-body cables were introducing some unwanted dynamics and so we developed our own cable models with increased accuracy, which have been cross-validated with analytical solvers and hardware prototypes (See sections 10.1.3 and 10.1.4). Thus, recently we re-ran some of the earlier coevolutionary learning experiments from this section with rods of 1 meter length and using our newer accurate cable models. The results are encouraging and show that we are still able to learn fast, smooth, dynamic rolling controllers, as shown in this section. These new results are not quite as fast, as expected due to the more physically realistic cable models. We also see that the performance was still increasing steeply at the point that we ended the experiments. Given that the prior experiments showed a step learning

curve prior to leveling off in performance, we expect that further iterations of learning on the current model would continue to improve. In general, this quick experiment gives us confidence that the basic control dynamics learned in the earlier work were valid, despite the scaling by a factor of 10 and the older cable models. More work could be done on this in future phases of this study, but we can also point to the excellent results of our next section on Dynamical and CPG based controls, all done using our current version of the simulator, to show a robust approach to controls.

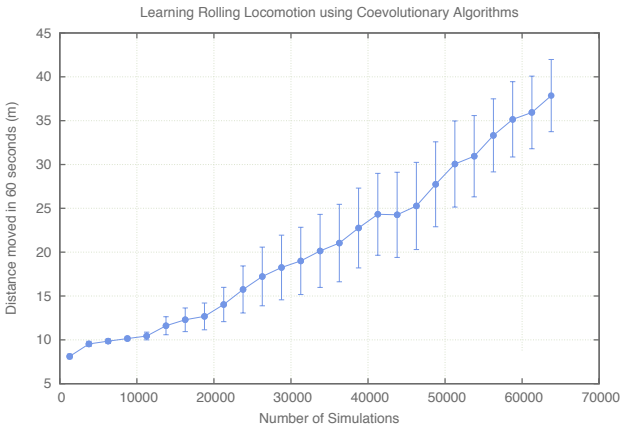

Figure 23: **Locomotion Learning with 1 Meter Rods and More Accurate Cable Model**. *Data is aggregated over 10 experimental learning sessions with the error bars showing max/min learned speeds. While slightly slower than prior results in this section, this shows that we can learn fast dynamic rolling controllers and gives us confidence that the results reported in this section are qualitatively valid.*

8 Dynamical and Central Pattern Generator Controls

The controls used by our evolutionary methods were a simple form of semi-distributed oscillatory control: All the actuations were controlled by sine waves synchronized through their relative phase shifts. These controls proved to be robust and sufficient for our goals of having our tensegrity platform roll smoothly. They also gave excellent examples and insight into what fundamental dynamics were required for fast smooth motion. On the other hand, a major limitation of these evolved controls is that they do not provide a means to direct or steer the motion of the tensegrity probe. Rather, a control law is learned which can be abstracted, but which does not allow reactive changes of direction. To develop steerable controls we took the insights gained from the evolved controllers and hand crafted reactive dynamical controllers that used a variety of simulated sensor feedbacks to enable steerable rolling. This approach was very successful and was shown to work on a variety of terrains, including moderate hills (Figure 28). But, this approach relied on significant amounts of sensor feedback which may be difficult to implement, so we wanted to find a hybrid approach that enabled steering while using a minimum amount of sensor feedback. Central Pattern Generators (CPG's) are able to store complex gait cycles in their network dynamics allowing for a significant reduction of sensor feedback required. We explored a variety of ways to use this property and to combine it with aspects of the dynamical controls approach to enable steering. The best result found so far uses the hand-coded dynamical controller as a trainer to learn the parameters for a Hybrid CPG which combines Hopf oscillators and Inverse Kinematics.

8.1 Principle

By inspecting the fast rolling controllers learned in the prior section we observed that the most efficient controllers would locate the central payload inside the probe such that its mass would cause the probe to roll. This was accompanied by different approaches for controlling the size and location of the polygon of ground contact points. Thus, in our dynamical controller the tensegrity structure is controlled using the torque created by the center of mass' displacement from the ground contact surface as illustrated on figure 24. This is achieved in 2 different ways: the heading is determined by the displacement of the central payload relative to its rest position in the center of the structure and speed is determined by the actuation of the outer shell strings.

The inner strings were actuated using three different approaches, a reactive approach, an inverse kinematics approach and a CPG approach (see Sections 8.2, 8.3 and 8.5 respectively). The outer strings where controlled in a different way. The goal of their dynamics is to reduce the contact surface with the ground. This affects the motion in several ways. First, it allows the creation of greater torques with the same payload displacement. Second, it allows a smoother rolling behavior of the whole structure, preventing shocks of the rods with the ground. Playing with the reactivity of the lengths corrections can also affect the global angular speed of the tensegrity structure.

The height of each string relative to the ground is computed using IR-like distance sensors located at the end of each rods (see Figure 25). The height assigned to each string is computed as the average of the two end points height. These measurements are performed continuously during the

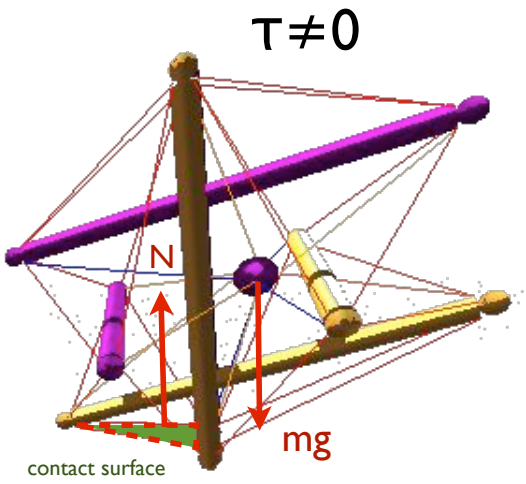

Figure 24: *Torque τ applied to the whole structure by a displacement of the center of mass*

simulations and the height parameter is constantly updated. If the tensegrity needs to move on uneven ground surfaces, it is important to know if the displacement occurs in the desired direction. Typically in the presence of a slope, the reduction of the ground contact surface can trigger the robot to roll down the slope without any control. In order to take this into account, we added a measure of the velocity. The velocity is computed using the global center of mass displacement between two consecutive time steps and the heading direction vector $\mathbf{v}$:

$$\text{velocity} = \mathbf{v} \cdot \frac{\mathbf{p}^{(n)} - \mathbf{p}^{(n-1)}}{dt} \tag{3}$$

where $\mathbf{p}^{(n)}$ is the 3D position of the center of mass at time t_n and $dt = t_n - t_{n-1}$ is the simulation time step. With this method, the velocity is a scalar number and has a sign depending on the heading of the tensegrity (positive if heading in the desired direction and negative otherwise). It can thus be used as a feedback to influence the strings command. The strings rest lengths are then computed using the following actuation rule:

$$\begin{cases} \dot{\ell}_i = w\left(\ell_0 + \min(h_i^2, h_0) - \ell_i\right) & , \text{ velocity} \geq 0 \\ \dot{\ell}_i = w\left(\bar{\ell} - \ell_i\right) & , \text{ otherwise} \end{cases} \tag{4}$$

where ℓ_i is the rest length of string i, ℓ_0, h_0 and $\bar{\ell}$ are constant parameters and $w \in \mathbb{R}_+$ accounts for the time scale at which lengths corrections occur.

Motor commands adjusting the strings rest length are performed through impedance controllers. The use of impedance controllers allow a smooth actuation of the string lengths and avoid creation of too high tensions within the string network. The commands are computed using the following actuation rule:

$$T_i = T_0 + k(\ell_i - l) + \eta(V_i - V_0) \tag{5}$$

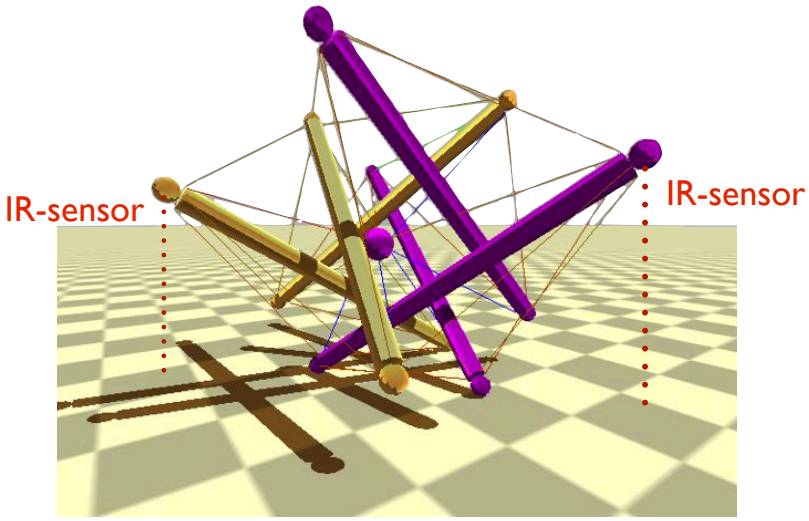

Figure 25: *Schematic view of the IR-sensors firing to the ground. Distance sensors are located at each rods end.*

where T_i is the target tension, T_0 is the offset tension, k is the elastic coefficient, ℓ_i the current rest length, l the current length, η a viscosity coefficient and V_i and V_0 the actual and target velocity of the motors, respectively. In our simulation, we kept T_0, k, η and V_0 constant.

8.2 Reactive Method

We first explain our reactive control method. Keep in mind that the only parameter that can be controlled is the rest length of each string. We denote ℓ_i as the rest length of the inner strings and l_i as their actual lengths. The global heading direction is defined by the unit vector $\mathbf{v}$ and the orientation of each string is represented by the vector $\mathbf{v}_i$. For each inner string we use the dot product $d_i = \mathbf{v} \cdot \mathbf{v}_i$ as feedback to control the position of the payload as follows:

$$\dot{\ell}_i = (\ell_0 + d_i\gamma - l_i)w$$
$$\ell_i(0) = \ell_0$$

where the weight w determines the reactivity of the system and $\gamma < 0$ is a fixed parameter. Thus, without any external perturbation, the system has a stable equilibrium position at $\ell_0 + d_i\gamma$. With this implementation, the strings that have their orientation aligned with the global heading see their rest length reduced and the strings pointing in the opposite direction are elongated. The global result is a displacement of the payload in the direction of the heading vector. See figures 26 and 27 below for a graphical representation of the method. Note that the heading direction $\mathbf{v}$ can be chosen arbitrarily and can be adjusted dynamically. It can be chosen in an absolute frame of reference or relative to the tensegrity orientation.

With this implementation, we were able to obtain stable and smooth rolling gaits allowing the tensegrity to roll up to 60 meters in 60 seconds over flat terrain. The robot could also handle slopes up to 8°, bumpy terrain (Figure 28), obstacles and collisions.

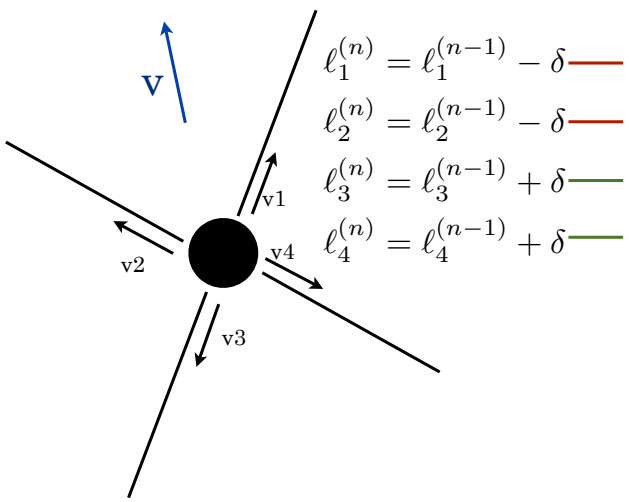

Figure 26: *Computation of the new rest lengths according to the strings individual orientations $\vec{v}_i$ (time $t^{(n-1)}$)*

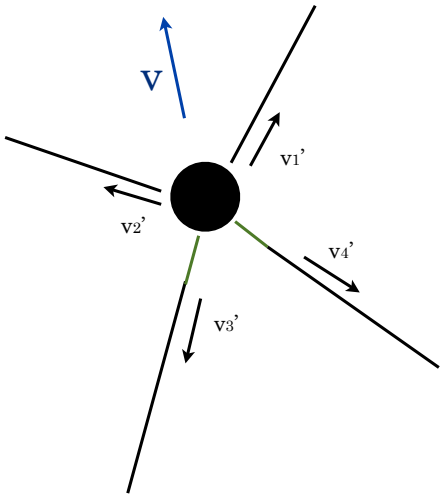

Figure 27: *Resulting effect is a displacement of the central payload in the desired direction $\vec{v}$ (time $t^{(n)} = t^{(n-1)} + dt$)*

Possible improvements:
The main disadvantage of the reactive method as presented here is the large amount of feedback required to actuate the motors. This can be a serious complication when it comes to designing the real tensegrity hardware. This justifies the research for simpler methods, based on the same physical principle but requiring less feedback information.

8.3 Inverse Kinematics Method

8.3.1 First order IK

The inverse kinematic method presented here can be an alternative to the reactive method. The idea is to apply the classical transpose Jacobian algorithm used in traditional robotics to control the 3D position of the central payload. Because of the intrinsic compliance of the tensegrity, the geometry of the robot is changing over time and an important modification that we have to add to this method is the dynamical computation of the Jacobian matrix to account for these changes of configuration.

The idea of this method is to define the 3D position of the central payload $\mathbf{p} = (p_1, p_2, p_3)$ as a function of the strings rest lengths $\boldsymbol{\ell} = (\ell_1, ..., \ell_n)$. Mathematically, we can write $\mathbf{p} = \mathbf{p}(\boldsymbol{\ell})$. As a consequence, in first approximation, a small displacement $\delta\mathbf{p}$ of the payload can be written as:

$$\delta p_i \approx p_i(\boldsymbol{\ell}^{(0)}) + \sum_{j=1}^{n} \frac{\partial p_i(\boldsymbol{\ell}^{(0)})}{\partial \ell_j} \delta\ell_j \qquad , \; i = 1, 2, 3 \tag{6}$$

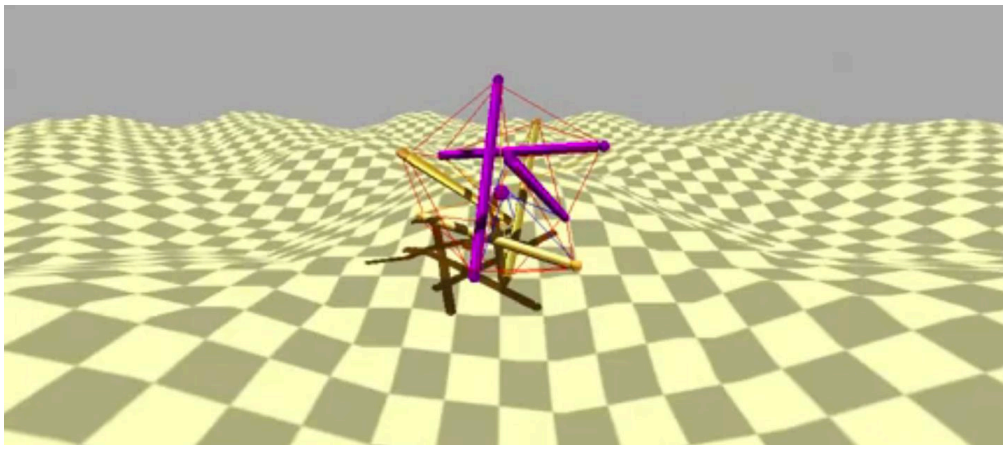

Figure 28: **Driving over Hills**. *The reactive control enables the tensegrity to be steered succesfully over moderate hills.*

Now, if we define the Jacobian matrix as $J(\mathbf{p}) = \left[\frac{\partial p_i}{\partial \ell_j}\right]_{ij}$, we can rewrite the above as:

$$\delta\mathbf{p} = \mathbf{p}^{(0)} + J\left(\mathbf{p}^{(0)}\right)\delta\boldsymbol{\ell} \tag{7}$$

This equation relates the payload displacement $\mathbf{p}^{(0)} - \delta\mathbf{p}$ to the change of rest lengths $\delta\boldsymbol{\ell}$. We can therefore determine what should be the change of the rest lengths to have the payload move in a certain direction. This can be expressed as:

$$\delta\boldsymbol{\ell} = J^{-1}(\mathbf{p}^{(0)})\left(\mathbf{p}^{(0)} - \delta\mathbf{p}\right) \tag{8}$$

However, computing the inverse of the Jacobian matrix is a very costly and complicated operation. Instead, we use the mathematical trick known as the Transpose Jacobian Method where we replace the inverse of J by its transpose to obtain:

$$\delta\boldsymbol{\ell} = \alpha J^T(\mathbf{p}^{(0)})\Delta\mathbf{p} \tag{9}$$

with $\alpha \in \mathbb{R}_+$ and $\Delta\mathbf{p} = \left(\mathbf{p}^{(0)} - \delta\mathbf{p}\right)$. This is relation allows us to compute the motor commands (i.e., the change of rest lengths) to move the payload in any direction we want. The main issue relies in the computation of the Jacobian matrix. In a static system made of bars and joints only, this matrix is constant and can be computed very precisely using appropriate mathematical tools. But in the case of a very compliant tensegrity structure, the coefficients of the Jacobian matrix are time dependent. The idea is thus to recompute the matrix coefficients dynamically using a finite difference method:

$$J(\mathbf{p}) \approx \left[\frac{p_i^{(n)} - p_i^{(n-1)}}{\ell_j^{(n)} - \ell_j^{(n-1)}}\right]_{ij} \tag{10}$$

Using equation (9) and (10) we are now able to move the payload in any direction with a feedback only on the payload position in space and each string's rest length.

The results obtained with these methods allow the tensegrity to roll up to 340 meters in 60 seconds on flat terrain. However the rolling gait is much more chaotic than with the reactive method. Moreover, some sudden and large corrections can occur unexpectedly. These unstable features come form the non-linearities present in the tensegrity structure that cannot be captured by this too simple first order method.

8.3.2 Second order IK

Again, the main drawback of the previous method are numerical inaccuracies due to the first order approximation to compute the relation between $\delta\mathbf{p}$ and $\delta\boldsymbol{\ell}$. Since tensegrity structures are by definition very compliant and oscillatory, higher order terms should be added in order to account for these non-linear behaviors. A possible improvement consists of extending the Taylor expansion to higher order terms, yielding (here up to 2nd order terms):

$$\delta p_i \approx p_i(\boldsymbol{\ell}^{(0)}) + \sum_{j=1}^{n} \frac{\partial p_i(\boldsymbol{\ell}^{(0)})}{\partial \ell_j}\delta\ell_j + \frac{1}{2}\sum_{j=1}^{n}\sum_{k=1}^{n} \frac{\partial^2 p_i(\boldsymbol{\ell}^{(0)})}{\partial \ell_j \partial \ell_k}\delta\ell_j\delta\ell_k \qquad , \; i = 1,2,3 \tag{11}$$

or

$$\delta p_i \approx p_i(\boldsymbol{\ell}^{(0)}) + \left(J(\mathbf{p}^{(0)})\delta\boldsymbol{\ell}\right)_i + \frac{1}{2}\delta\boldsymbol{\ell}^T H\left(p_i(\boldsymbol{\ell}^{(0)})\right)\delta\boldsymbol{\ell} \qquad , \; i = 1,2,3 \tag{12}$$

where $H(p_i) = \left[\dfrac{\partial^2 p_i}{\partial\ell_j\partial\ell_k}\right]_{jk}$ is the Hessian matrix associated to p_i.

Considering (12), we define additionally $\Delta\mathbf{p} = \delta\mathbf{p} - \mathbf{p}(\boldsymbol{\ell}^{(0)})$ and $\mathbf{f}(\delta\boldsymbol{\ell};\Delta\mathbf{p})$ as

$$f_i(\delta\boldsymbol{\ell};\Delta\mathbf{p}) = \left(J(\mathbf{p}^{(0)})\delta\boldsymbol{\ell}\right)_i + \frac{1}{2}\delta\boldsymbol{\ell}^T H\left(p_i(\boldsymbol{\ell}^{(0)})\right)\delta\boldsymbol{\ell} - \Delta p_i \qquad , \; i = 1,2,3 \tag{13}$$

The idea is, given a desired displacement of the payload in the 3D space $\Delta\mathbf{p}$, to find the corresponding lengths change $\delta\boldsymbol{\ell}$ that will lead to this displacement. This corresponds to finding $\delta\boldsymbol{\ell}$ such that $\mathbf{f} = \mathbf{0}$. Note however that this system is overdetermined, non linear and might not possess a real solution. In order to bypass these difficulties, we can compute an approximation of the solution using a quasi-newtonian iterative method. The idea is to start with an arbitrary position, e.g. $\delta\boldsymbol{\ell}_0 = \mathbf{0}$, and compute the next iteration as:

$$\delta\boldsymbol{\ell}_{k+1} = \delta\boldsymbol{\ell}_k - J_k^{-1}\mathbf{f}(\delta\boldsymbol{\ell}_k;\Delta\mathbf{p}) \tag{14}$$

until convergence is achieved. J^{-1} denotes here the Moore-Penrose pseudo inverse of the Jacobian defined by $J = \left[\dfrac{\partial f_i}{\partial(\delta\ell_j)}\right]_{ij}$.
Note that this matrix is not the same as the one appearing in the Taylor expansion of $\mathbf{p}(\boldsymbol{\ell})$. The pseudo inverse is computed using a singular value decomposition of the Jacobian matrix $J = U\Sigma V^*$ where U is a unitary matrix, Σ is a rectangular diagonal matrix containing the singular values of J, and V^* (the conjugate transpose of V) is a second unitary matrix. Once the three matrices have been computed, the pseudo inverse can be found by a simple matrix multiplication $J^{-1} = V\Sigma^{-1}U^*$ with $\Sigma^{-1} = \text{diag}(1/\sigma_i \; , i = 1, ..., n)$. Figure 29 shows how quickly this method converges for various iterations.

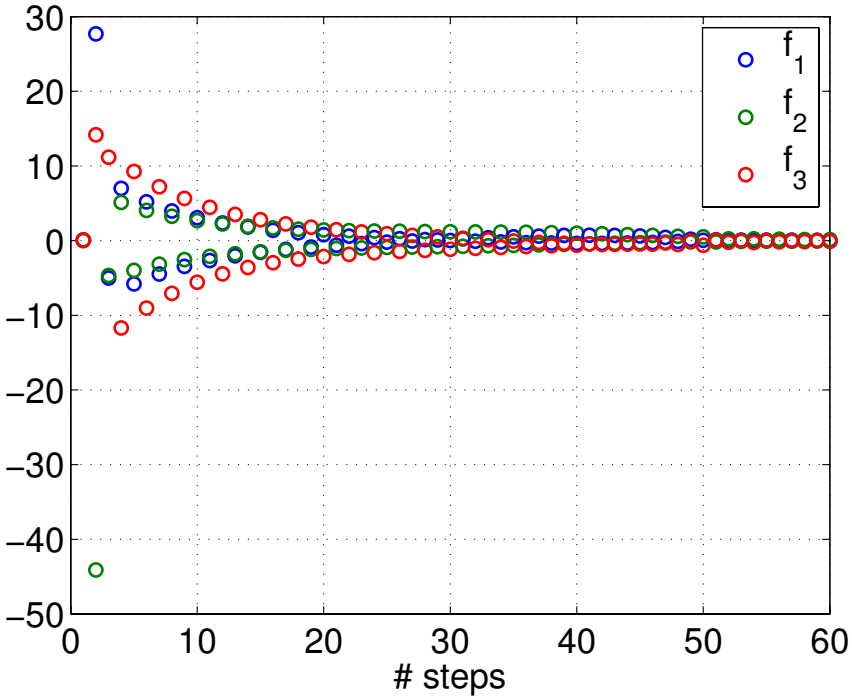

Figure 29: *Example of the convergence in ∼50 iterations of the quasi-Newton method for* $\Delta\mathbf{p} = (0.1, 0, 0.1)$, *starting from* $\delta\boldsymbol{\ell}_0 = \mathbf{0}$ *(plot of the 3 coordinates of* $\mathbf{f} = (f_1, f_2, f_3)$*).*

Possible improvements:
Of course this system is complicated than the first order approximation and requires more complex and costly numerical techniques to be solved. Moreover, convergence cannot be guaranteed as solutions may not exist or numerical instabilities might drive the system out of the convergence region. Note also that in real hardware these additional computations may lead to higher energy consumption and would require a greater computational power in order to solve these equations in real time. Another major drawback is the fact that the payload position depends only indirectly from the strings rest lengths. As a result, the inverse kinematics might be ”mistaken” if two or more antagonist motor commands are executed at the same time. Indeed, in this particular case, a motor might reduce a given string's rest length but still measure the payload moving away from the string's anchor point due to the other motors actions. This effect leads to contradictory motor commands once the inverse kinematics algorithm is executed and, unfortunately, these errors cannot be solved by better numerical accuracy or even higher order methods.

A possible improvement that might address this issue would be to reduce the number of strings that can be actuated. This would reduce both the complexity of the problem and the mistakes happening when antagonist strings are actuated. However these errors would always remain present at a certain level as they are inherent to the tensegrity physical properties and to the control and feedback method we adopted.

8.4 Gyroscopic Method

An easy way to tackle the orientation issue is to use the physical properties of gyroscopes to create torques in any given direction and keep track of a given orientation. The idea of the method is to construct a gyroscope inside the central payload and change its orientation in order to create a torque on the whole structure. The torque will tilt the payload, pulling on the inner strings of the structure and thus creating a force on the ground pulling the tensegrity forward. See Figures 30 and 31 for a schematic explanation.

This method has the advantage of requiring no actuation of the inner muscles, all the forces resulting from the payload's twisting motion. Furthermore, the heading of the tensegrity can be chosen quite easily as the gyroscope will try to keep its orientation if no external force is applied. The control of the motion is also simplified as we reduce the problem of actuating 12 strings to choosing the pitch, roll and yaw of the payload. A detailed physical analysis of this method can be done on the model of the torsion pendulum.

With this implementation and the current physical shape (no modifications to the payload size or inner strings tensions), we were able to achieve displacements of more than 53m over 60 seconds of simulation. Note however, that irregular terrain configurations such as bumps and slopes cannot be handle as well as with the reactive method.

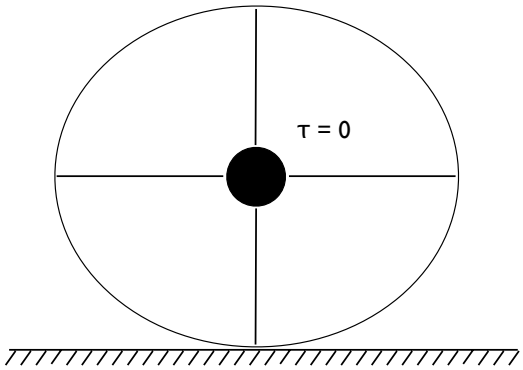

Figure 30: *Stable rest situation, no torque is applied. The tensegrity is schematized by the circular shape, the central payload is connected by 4 inner muscles.*

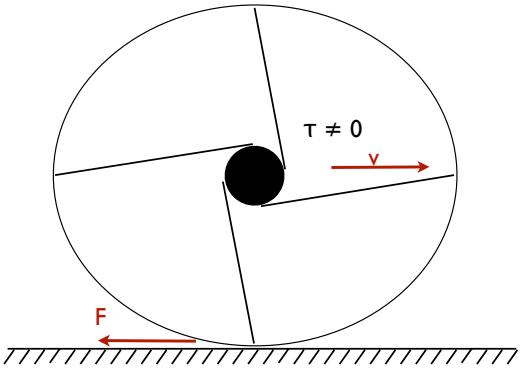

Figure 31: *Once a torque is applied, the central payload is tilted and pull on the inner strings. This motion creates a force F on the ground moving the tensegrity forward.*

Possible improvements:
Of course, the major drawback of this method is the requirement for relatively heavy and voluminous gyroscopes that have to be inserted in the payload structure. Also this method is heavily dependent on the diameter of the payload, the bigger the diameter, the greater the torque we can apply to the structure. As a result, the size of the payload would have to be optimized to match both the motion and security requirements. Moreover, the tension of the inner strings can be tuned to adapt to the magnitude of the force created on the ground.

8.5 CPG and Adaptive Frequency Oscillators Method

Another approach is the storage of a stable gait obtained in simulation inside a central pattern generator (CPG). The idea is to use as much feedback as needed in order to get a smooth motion and then store the resulting periodic commands as a stable limit cycle of a CPG. Once this process is done, the tensegrity can be driven with the CPG output with much less feedback than before.

8.5.1 Arbitrary Waveform Oscillator

In order to be able to store and recreate different types of signals, we use a so called arbitrary waveform oscillator (AWO). The dynamical system driving the CPG is presented below. As usual, we denote the muscle rest length by ℓ_i.

$$\dot{\ell}_i = \gamma(g(\varphi_i) - \ell_i) + \frac{dg(\varphi_i)}{d\varphi_i}\,\dot{\varphi}_i \tag{15}$$

$$\dot{\varphi}_i = \omega_i + \sum_j \sin(\varphi_j - \varphi_i - \phi_{ij}) \tag{16}$$

where the function $g(\varphi)$ is a periodic and derivable function, $\gamma \in \mathbb{R}_+$ is a parameter accounting for the systems time scale, ω_i is the pulsation of the periodic output and $\phi_{i,j}$ is the desired shift between signal i and j. Without any external perturbations, the system converges to $\ell_{i,\infty} = g(\varphi_i)$ where $\varphi_i = \omega t$ and $\varphi_i - \varphi_j = \mod(\phi_{ij}, 2\pi)\ \forall(i,j)$. In our case, for geometrical reasons and for simplicity we choose $g(\varphi) = A\sin(\varphi)$, $A \in \mathbb{R}^*$.

Furthermore, in order to synchronize to a periodic input signal $f_i(t)$ of pulsation ω_{in} and mean value $\bar{f}_i$, we add the following equation driving the time evolution of ω_i during the learning phase:

$$\dot{\omega}_i = \epsilon(f_i(t) - \bar{f}_i)g(\varphi_i + \pi/2) \tag{17}$$

where $\epsilon \in \mathbb{R}_+$ is a parameter accounting for the time scale. When the learning phase is completed, the value of ω_i is held constant by setting $\dot{\omega}_i = 0\ \forall i$.

On Figures 32 and 33, we can observe the convergence of the CPG pulsation ω to the input signal pulsation ω_{in} in an ideal case where the input signal is a simple sinusoidal function $f(t) = \sin(2t)$.

On Figures 34 and 35, we can see the synchronization of the CPG output (red) to the learning signal (blue) during the learning phase. The signal here correspond to the value of the dot product d_i when the tensegrity is driven using only the reactive method (see Section 8.2). Each string possess its own CPG that learns and creates its own output. The perturbations and irregularities appearing between 0 to 15 seconds are due to a chaotic motion where the tensegrity has not yet found a stable rolling pattern. After about 20 seconds, one can observe that the input signal becomes much more regular and periodic, this correspond to a stable rolling gait that can be well captured by the CPG as a sine function. Note that the mean of the signal $\bar{f}$ is dynamically updated in order to account for signal that are constantly shifted above and below 0.

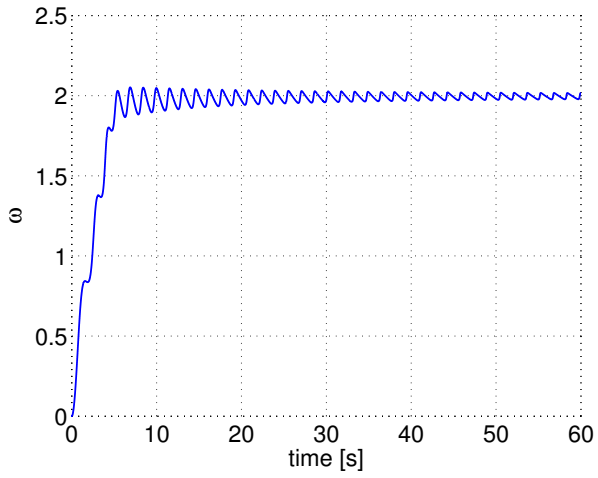

Figure 32: *Time plot showing the convergence of pulsation ω towards the input signal $\omega_{in} = 2$ during the learning phase*

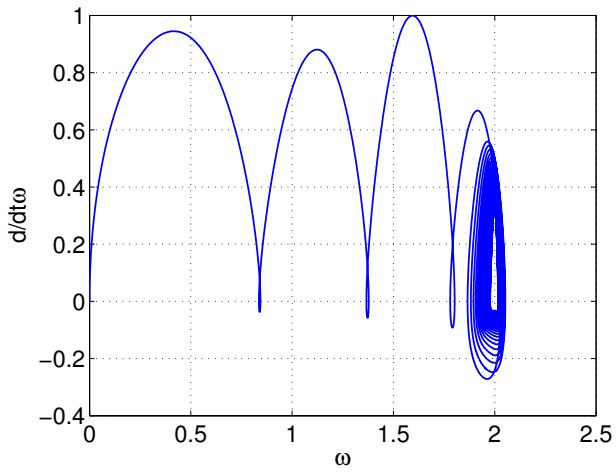

Figure 33: *Phase plot showing the convergence towards a stable fixed point at $\omega = 2$*

Once the learning phase is completed, the parameters of the CPG are kept constant and the CPG output $g(\varphi_i)$ is then used to command the rest lengths ℓ_i. If the CPG is able to mimic perfectly the previous commands, we would expect to see the tensegrity rolling with the same gait as with the reactive method but without the need for any orientation feedbacks. Using the phase shift parameters ϕ_{ij} (see equation (16)), we can also force a delay between two (or more) oscillators. In some cases, for instance for diametrically opposed strings, it is obvious that a phase shift of π would be appropriate (see figure 37 for a graphical representation of the whole oscillator network). The value of the coefficients ϕ_{ij} can also be extracted by a careful analysis of the signals shift during the learning phase and then be assigned to the corresponding coefficients.

This method has the advantage of requiring no (or almost no) feedback and thus only a very small amount of computations. It can therefore be implemented easily on real hardware. However, it is important to note that the dynamical system runs on a much larger time scale than the perturbations disturbing the system. A tensegrity driven only by a CPG would then, in the best case, have a stable rolling gait on a flat, obstacle free terrain. This effect is even accentuated by the inherent non-linear response that tensegrity structures possess. As a result, it is necessary to include also a second control method that can work on this smaller time scale and give an appropriate response to these external perturbations.

Simulations were performed where the tensegrity was driven during 50 seconds using the reactive method. This first phase was used to synchronize the CPG output with the input signal given to the robot (Figures 34 and 35). Then, the controls were shifted to be driven only by the CPG output and the learning phase was stopped. No further feedback was used to drive the robot's motion. Results showed that the tensegrity could continue rolling for a few seconds but quickly rolled on

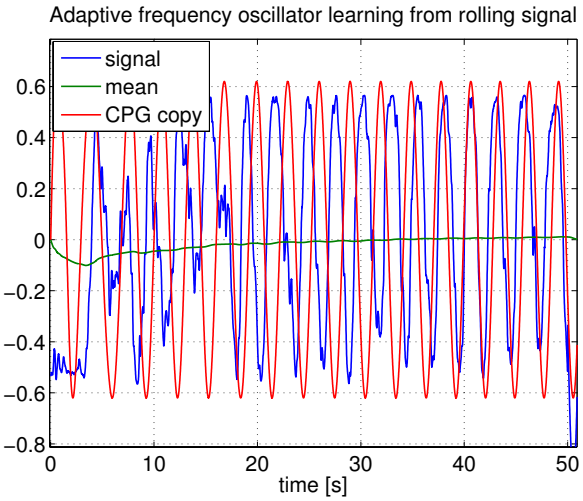

Figure 34: *Dynamic synchronization of CPG signal (string #3)*

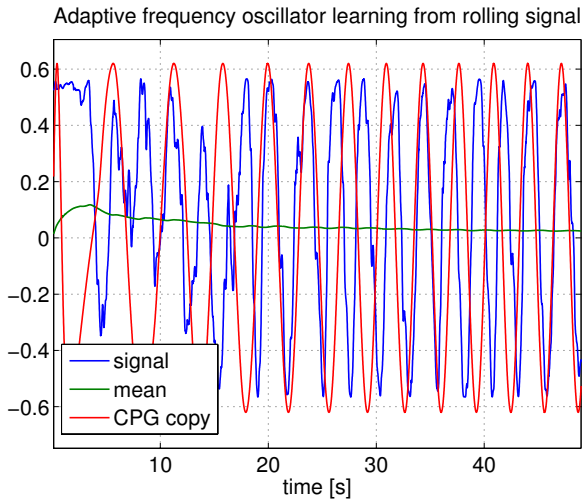

Figure 35: *Dynamic synchronization of CPG signal (string #4).*

the side changing completely the orientation and being therefore unable to move smoothly using the signal learned previously. After some time and random displacements, the robot can fall back in the right position and keep rolling for some more time but eventually falls back in an unwanted position. With this type of motion, only small travel distances were achieved compared to the reactive and inverse kinematics method. This can be seen in figure 36 and figure 37 is a graphical representation of the oscillator network.

Possible improvements:
Since the tensegrity can easily be perturbed and roll on the side, and since the synchronization of all CPG signals is not always perfect, the tensegrity cannot keep rolling on a stable gait for more than a few seconds. Even on flat and obstacle free terrain, an open loop control is not sufficient to drive the robot smoothly. A good improvement would be to mix the CPG approach with one of the

technique discussed above. As stated previously, the CPG could drive the global rolling motion, occurring on a large time scale, while the corrections, occurring on a much smaller time scales would be done through an inverse kinematics algorithm or a reactive control.

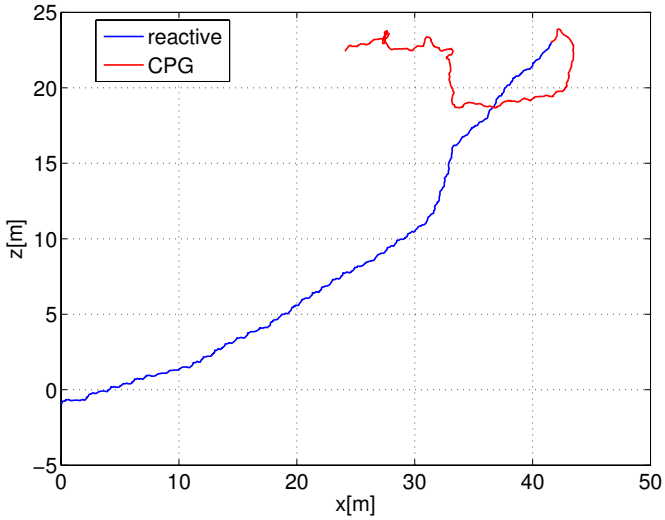

Figure 36: *2D trajectory of the tensegrity (seen from above). The blue curve represents the trajectory while the robot is driven by the reactive control algorithm and the CPG is in the learning mode (50 seconds). The motion is very regular and the heading is maintained throughout the whole period. The red trajectory represent the path traveled once the CPG controller takes over (40 seconds). Due to the open loop implementation, the heading of the robot cannot be maintained and the tensegrity ends up rolling in random directions.*

8.5.2 Hopf Oscillator

Due to the ball-like structure of the tensegrity, the signals we want to copy during the rolling phase can be assumed as sinusoids. Thus, instead of AWOs, we can consider using Hopf oscillators defined by:

$$\dot{x} = \gamma(\mu - (x^2 + y^2))x - \omega y \tag{18}$$
$$\dot{y} = \gamma(\mu - (x^2 + y^2))y + \omega x \tag{19}$$

where γ is a time constant, μ is the target frequency and ω the target pulsation of the signal. This dynamical system can be adapted to synchronize to any periodic input signal $f(t)$. The resulting adaptive frequency Hopf oscillator is defined by the following set of equations:

$$\dot{x} = \gamma(\mu - (x^2 + y^2))x - \omega y + \epsilon f(t) \tag{20}$$
$$\dot{y} = \gamma(\mu - (x^2 + y^2))y + \omega x \tag{21}$$
$$\dot{\omega} = -\epsilon f(t)\frac{y}{x^2 + y^2} \tag{22}$$

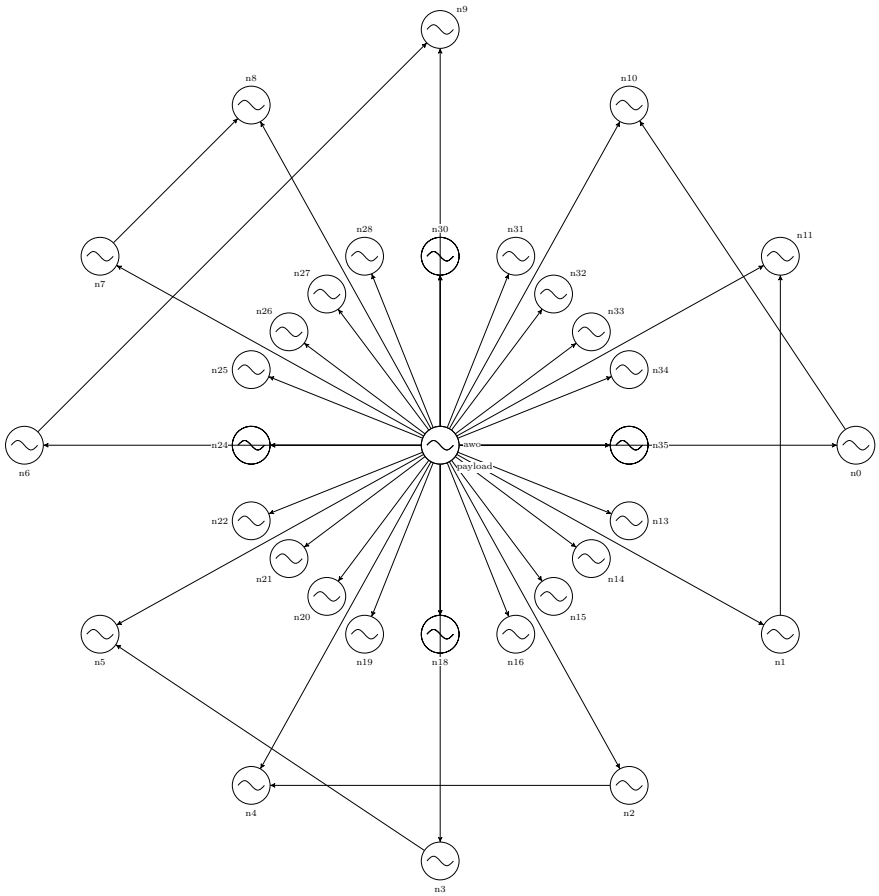

Figure 37: *Schematic view of the whole oscillators network. Nodes 0-11 represent the oscillators associated to the inner strings, nodes 12-35 represent the oscillators associated to the outer strings. The central node represent the payload, where the orientation and speed is computed and then shared to the other nodes through their common links (arrows). The arrows on the outer links represent a non zero phase shift* ϕ_{ij}.

As with the AWO, we can now record the periodic signal during a learning phase and store it as a stable limit cycle of the Hopf oscillator. This signal can later be used to drive the tensegrity.

On Figure 38 above, we can notice a coupling between the height signal (green), i.e. the height of the muscle connecting the payload with the learning signal (red). This coupling can be enforced by adding a new term to the dynamical system (18), (19). This coupling will allow the oscillator to synchronize with the real tensegrity motion and enable the system to deal with ground contact and unexpected perturbations that may occur during the rolling. We denote by $h(t)$ the height signal fed back by the ID-sensors, the resulting dynamical system used for rolling is then given by:

$$\dot{x} = \gamma(\mu - (x^2 + y^2))x - \omega y - kh(t) \tag{23}$$

$$\dot{y} = \gamma(\mu - (x^2 + y^2))y + \omega x \tag{24}$$

with $k \in \mathbb{R}_+$. Adding the coupling term improves significantly the distance that the tensegrity can roll, see figures 39 and 40 for a numerical example.

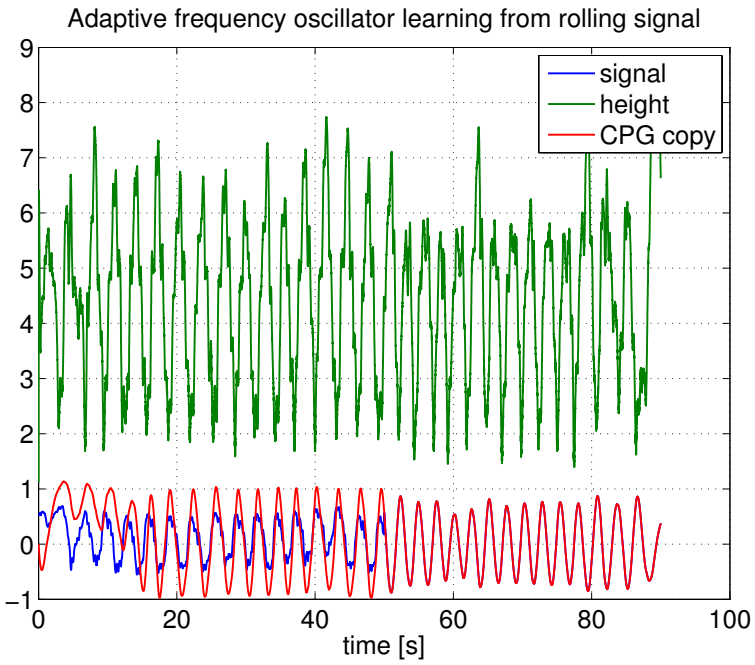

Figure 38: *Adaptive Hopf oscillator synching its output signal (red) to an periodic input signal (blue). The dynamical system can reproduce a sinusoid with the same frequency and phase once the learning signal is removed (50-90 sec).*

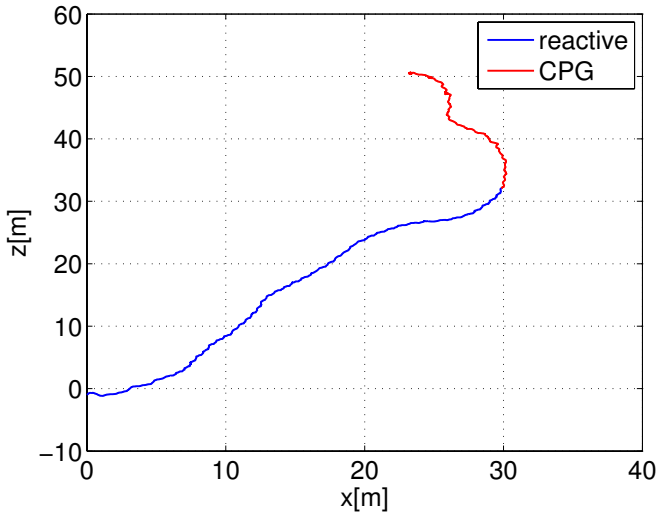

Figure 39: *2D trajectory of the tensegrity (seen from above). The blue curve represents the trajectory while the robot is driven by the reactive control algorithm and the CPG is in the learning mode (50 seconds). The motion is very regular and the heading is maintained throughout the whole period. The red trajectory represent the path traveled once the CPG controller takes over (40 seconds). The CPG is here driven purely open-loop and the tensegrity travels a total distance of 56.8m.*

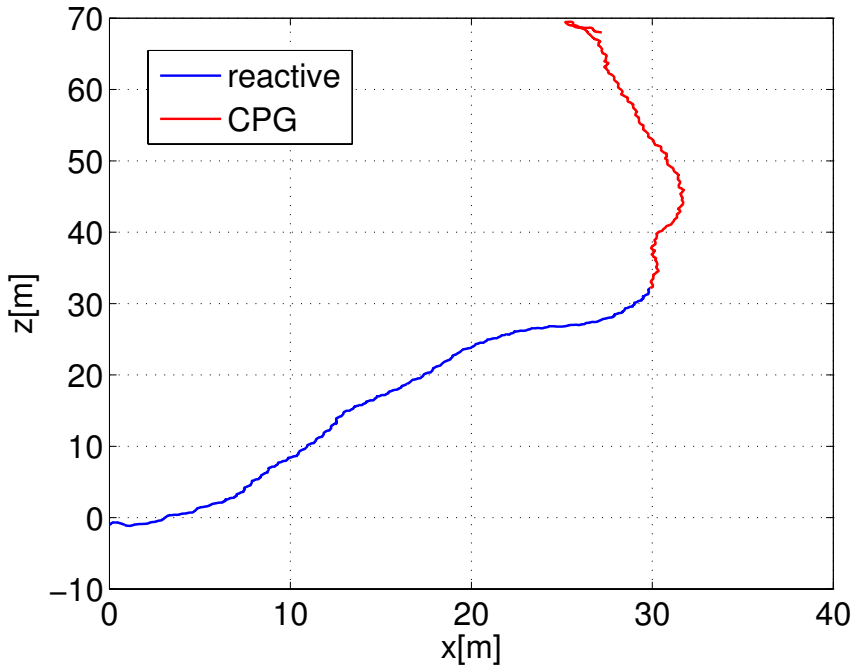

Figure 40: *2D trajectory of the tensegrity (seen from above). The blue curve represents the trajectory while the robot is driven by the reactive control algorithm and the CPG is in the learning mode (50 seconds). The motion is very regular and the heading is maintained throughout the whole period. The red trajectory represent the path traveled once the CPG controller takes over (40 seconds). The CPG receives here feed back from the payload strings height, the tensegrity travels a total distance of 74.3m.*

Possible improvements:
Hopf oscillators can synchronize very accurately to periodic input signal and are therefore very well suited for learning motor commands for rolling tensegrities. Moreover, coupling can be added using feedback signals obtained from data measured by the robot sensors. This coupling enables the tensegrity to react to unexpected obstacles on the ground and adapts the output signal of the oscillator to the real robots position. This allows the tensegrity to roll faster and further.

However, while allowing longer rolling distances, this feedback does not control the robots heading. As we can see on Figures 39 and 40, the red trajectory does not maintain a constant heading. As a consequence, additional parameters have to be added to the dynamical system or a hybrid method, such as a mix CPG - inverse kinematics can be used.

8.6 Hybrid CPG - Inverse Kinematics method

8.6.1 AWO and IK

The aim of this method is to close the loop of the AWO CPG in order to be able to control the motion of the tensegrity. For this purpose, we add two terms χ_i and ξ_i to the original dynamical

system equations (15) and (16):

$$\dot{\ell}_i = \gamma(g(\varphi_i) + \chi_i - \ell_i) + \frac{dg(\varphi_i)}{d\varphi_i}\dot{\varphi}_i + \xi_i \tag{25}$$

$$\dot{\varphi}_i = \omega_i + \sum_j \sin(\varphi_j - \varphi_i - \phi_{ij}) \tag{26}$$

These feedback terms will account for unpredicted movements of the tensegrity and perturb the limit cycle of the dynamical system to let the robot come back on the desired trajectory. Since these corrections have to be momentaneous, we impose a fading memory dynamic:

$$\dot{\chi}_i = -\lambda\chi_i$$
$$\dot{\xi}_i = -\mu\xi_i$$

with $\lambda, \mu \in \mathbb{R}_+$.

To compute the values of χ and ξ, we use the second order kinematics method as presented in Section 8.3.2. χ and ξ are updated if and only if the payload position lies on the opposite side of the robots center of mass. In this way, the corrections are made only if the tensegrity can potentially roll in a undesired direction. Note also that in order to use this method, we need to know the position of the payload and the center of mass.

8.6.2 Hopf oscillators and IK

We can apply the same method to the adaptive frequency oscillator as presented in Section 8.5.2. We add the corrective term to the output of the oscillator. The resulting dynamical system reads:

$$\dot{x} = \gamma(\mu - (x^2 + y^2))x - \omega y - kh(t) \tag{27}$$

$$\dot{y} = \gamma(\mu - (x^2 + y^2))y + \omega x \tag{28}$$

$$\text{out} = x + \xi(t) \tag{29}$$

where $\xi(t)$ decreases exponentially with time.

Possible improvements:
This method's efficiency relies on the quality of the inverse kinematics algorithm used. As a consequence, if we want to improve the method, we need to look into more accurate inverse kinematics algorithms. For simple tensegrity structures such as the 6-struts icosahedron considered in this paper, closed form solutions for the inverse kinematics can also be worth investigating.
Remember from the discussion of Section 8.3 that the IK method has to be relatively cheap in terms of calculations and precise enough in order to deal with the dynamics of the tensegrity.

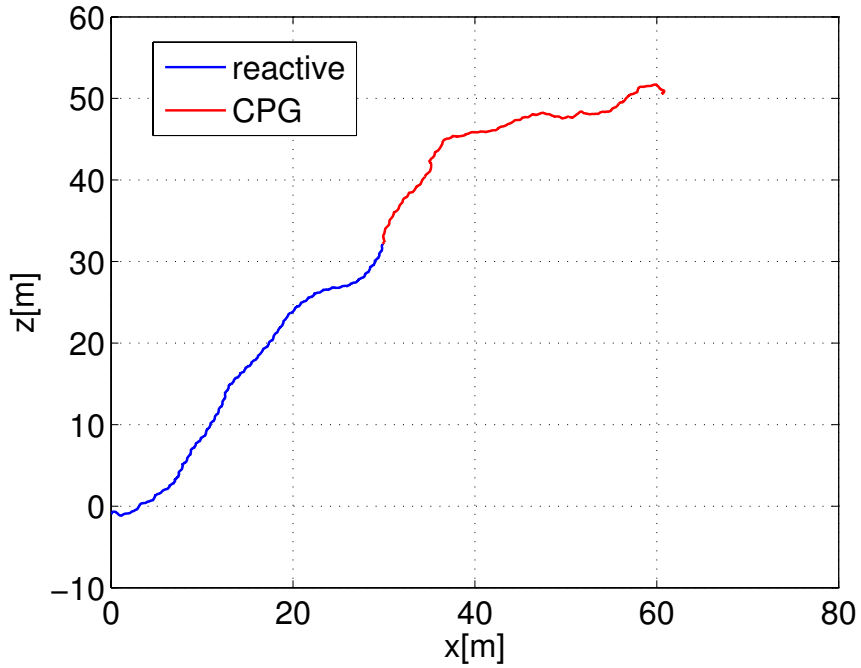

Figure 41: *2D trajectory of the tensegrity (seen from above). The blue curve represents the trajectory while the robot is driven by the reactive control algorithm and the CPG is in the learning mode (50 seconds). The motion is very regular and the heading is maintained throughout the whole period. The red trajectory represent the path traveled once the CPG controller takes over (40 seconds).*

The CPG is now coupled to the height signal and receives inputs from the second order inverse kinematics algorithm in case it starts rolling in a wrong direction. The resulting trajectory is a long and relatively straight line extending well the reactive control.

9 Hardware Robot

In conjunction with our Phase I study, we have been working collaboratively with the University of Idaho providing students with a capstone senior design project researching tensegrity structures for possible application in space exploration. This years project focused on investigating properties of spherical tensegrity probes, including its load capabilities and mechanization of the packing and deployment methods.

9.1 Project Goals

The four goals of this project were as follows:

1. Provide a structural design and prototype capable of withstanding a 10-meter test fall.
2. Structural Analysis of the Hardware design
3. Mechanization of the collapse and standing method(s) of the structure.
4. Perform Drop tests of the prototype. These will be reported on in Section 10.

The first goal was selected because the velocity achieved in a 10-meter drop here in earth's gravitational field is approximately equivalent to the terminal velocity reached in the gravitational field of Saturn's moon Titan. By withstanding a 10-meter drop here, the structure should be sufficiently strong to withstand the landing impact on Titan. In order to build the hardware, structural analysis was performed using Abaqus Finite Element Analysis. In order to either increase the number of probes sent to Titan or to reduce the amount of space needed to send a single probe to Titan, methods of collapsing and expanding the structure were investigated. The structures would be sent in the collapsed state to conserve space, but upon deployment would expand to a standing position to brace for impact with the surface. It is worth noting that the prototype built used a minimal number of actuators required for deployment, as a result the fully flat storage approach presented elsewhere is was not possible. Instead, we developed optimal packing methods given the six actuators in the prototype. Full actuation of the tensegrity probe would lead to much more efficient packing to a flat triangle. The Tensegrity Simulator built on the Bullet Physics Engine used elsewhere in this project was used to simulate this collapse, expansion, and impact.

9.2 Structural Component

9.2.1 Structure of Choice

In the beginning, the following three structures were considered: a six strut, 24-string Icosahedron; 12-strut, 36-string Cuboctahedron; and a 30 strut, 30-string Dodecahedron. These three structures are displayed below in Figure 42.

The 30 strut structure was quickly dismissed due to its lack of interior strength resulting from zero cross members in the design (see note below). The selection process was continued by a static load testing experiment. Since the structure needed the capability of withstanding a 10-meter test fall

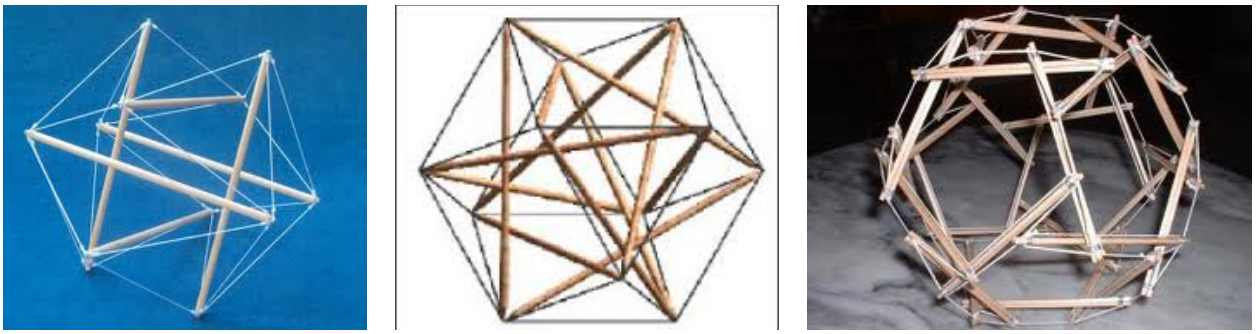

Figure 42: **Types of Tensegrity Structures**. *6-strut, 12-strut and 30-strut structures were considered.*

it was of interest to determine which configuration was inherently more rigid and thus most able to handle externally applied loads. To begin, three prototypes of both structures (for a total of six) were constructed out of standard SCH 40 1/2 inch PVC struts and 300lb test parachute cord. Static loading tests were conducted by placing each structure in its most stable orientation (most points of contact), placing a one foot square piece of plywood on top, and performing the following:

1. Measure standing height to bottom of plywood
2. Place weight on plywood
3. Measure height to bottom of plywood again (calculate deflection)
4. Remove weight
5. Measure again to check rebound and use for initial height of next load

This was performed for a range of weights from 5 lbs to 25 lbs. Once all the data was collected a One Way ANOVA statistical analysis was used in search of trends describing and favoring one structure over the other. The analysis favored the six strut Icosahedron's load bearing capabilities indicating this as the more rigid of the two structures. Additionally, with time spent investigating the geometry of each structure two easily definable methods to collapse and expand the six strut Icosahedron were developed. These two methods will be further discussed later. Based on the ANOVA analysis and methods of collapse, the decision was made to continue the study with a focus on the six strut Icosahedron.

Note: Later experiments by a different team of students from Berkeley (discussed in Section 10.3) show that the 30-strut Dodecahedron is in fact capable of protecting a payload during a 10 meter drop test. They key insights are that the cables required to suspend the payload add structural stiffness (much like the spokes on a bicycle wheel), and that the stiffness of the cables makes a significant difference in the load bearing properties of the structure, and finally that the larger interior volume of the 30-strut model is helpful in protecting a payload. The key lesson here is that a deeper analysis of optimal morphology of the structure is still required where one balances the engineering requirements of deployment, landing, payload protection, and mobility. The rest of this section focuses on the 6-strut tensegrity which has maximal structural stiffness and is the simplest form for our initial deployment and drop-test study, which did not consider the payload or mobility.

9.2.2 Structural Construction

Construction of the final prototype began by cutting a ten-foot piece of 1-3/8 OD, 1/8 wall thickness aluminum into 20 inch long pieces for use as each strut. Aluminum was selected as it is relatively inexpensive and has a sufficiently high strength to weight ratio. Instead of using the same material for all the tension members, it was decided to use both elastic and non-elastic members. By using the elastic members, the structure would be capable of deforming slightly on impact without breaking while the non-elastic members are necessary for creating actuated faces. For the 18 elastic members, extension springs with a spring constant (k) equal to 1.5 lbs/in were selected. Many other springs rates (ie 0.7 lbs/in and 0.5 lbs/in) were tried, but this was selected for the final structure due to the structural stiffness they provided. These springs also provided the amount of deflection necessary to reach full collapsibility. For the six non-elastic members on the actuated faces 200 lb test Dacron string was implemented. All connections were held in place by threading $1/4$"-28" holes on both ends of each strut and fitting them with steel spring anchors.

9.2.3 Motor Implementation

To mechanize the movement of the structure from standing to a collapsed position and back to a standing position six DC motors were internally mounted. Three in the ends of each strut that form one of the equilateral triangular faces with three more motors in the opposite side of the structure again forming an equilateral triangular face. Each motorized end assembly has the motor fitted in an aluminum sleeve with diameter a couple hundredths less than that of the aluminum pipe for a tight fit. 10-32 set screws were joined into the rod and pressed down onto the sleeve to hold the motor in place. On the top shaft of each motor a spool was placed and locked in place with a 4-40 set screw. Figure 43 shows an exploded view of this motorized end assembly.

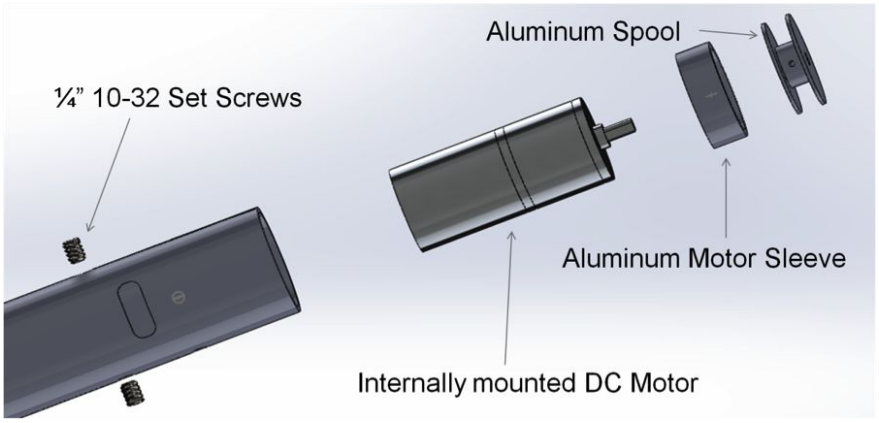

Figure 43: **Assembly of Actuators into Rods of the Prototype Lander.**

9.2.4 Methods of Collapse

There are two methods of collapsing and expanding the partially actuated structure used in this study. These two methods will be referred to as the Star Elongation and Linearly Extended methods.

1. Star Elongation: This method requires an orientation where the actuated faces are the top and bottom of the structure. By rotating the motors such that the string faces are allowed to elongate, the structure will collapse into a relatively flat star shape. The final height of this method depends greatly on the springs implemented. In the final prototype, the diameter of the springs prevented it from collapsing as far as earlier models. This is because in earlier models, the springs were able to bend allowing a greater range of collapse while the diameter of the final springs used was too large to allow this. With regards to storage, this method is preferable as the configuration allows for the most effective use of allowable storage space. Figure 44 shows the starting and final states of this structure.

Figure 44: **Tensegrity under Star Elongation Method of Collapse.**

2. Linearly Extended: This method requires an orientation where the string actauted faces are the right and left faces of the structure. Through spooling the string in and collpasing these faces the structure collpases approximately linearly. The method of collapse is displayed in Figure 45.

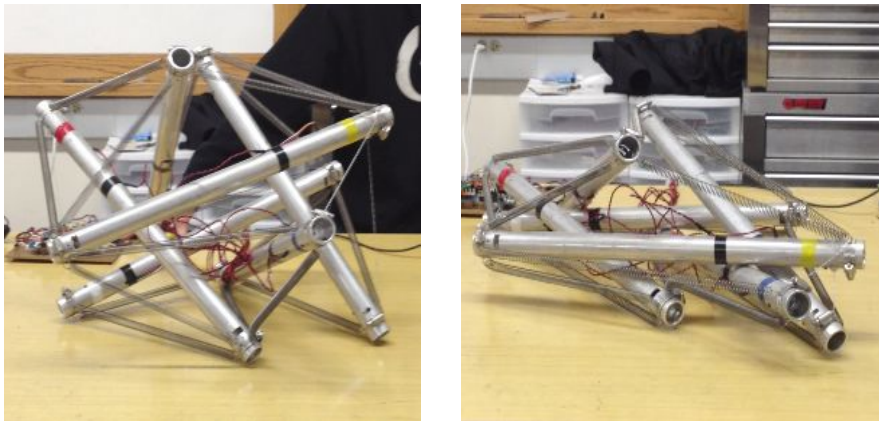

Figure 45: **Tensegrity under Linear Extension Method of Collapse.**

9.2.5 Abaqus FEA Simulation

In order to make informed design parameters and quickly and cheaply test designs without risking breakage, it was important to be able to simulate the structure falling in a computer simulation. It

was necessary that the software package used be robust enough to handle the indeterminate nature of a complex tensegrity structure, while providing the engineering precision necessary to inform design decisions.

The finite element analysis software Abaqus fit the criteria above. It modeled the fall of a six strut tensegrity structure from 10 meters. The structure was modeled to approximate the structure our team constructed. All values were considered to be metric units to maintain consistency, even though Abaqus does not in fact have any defined units system. The struts were defined as beams with a pipe cross section that were 0.508 m long and had an inner diameter of 0.0274 m and an outer diameter of 0.0318 m. The struts were rotated and translated in the assembly to form a tensegrity icosahedron. The springs were attached at the appropriate endpoints and given various elastic moduli according to the requirements for each simulation. A discrete rigid plane was defined with a reference point at its center to be the floor that the spherical tensegrity impacted.

For the initial conditions, the reference point on the floor was ENCASTRE to fix the floor. The structure was given a negative velocity of 14 m/s towards the floor. The model was translated to a small distance above the floor since it was already at its final velocity. It was also rotated to various configurations in the assembly to create various drop conditions. The model was given a tangential friction property of All with Self and the friction factor was defined to be 0.3.

The simulation was run as a dynamic explicit model to obtain convergence. In addition to obtaining the Mises stress in the field output, history output was specifically requested for each spring to record a force at small time steps in each spring during impact. Overall, it was found that implementing springs with lower elasticity led to lower overall forces, but this had to be balanced with maintaining structure shape during impact. A recommendation based on these models is made for implementing springs with a spring rate around 25 lb/in and a maximum force of about 100 lbs. The simulation showed that stress in the struts should be below the yield strength for the 6000 series aluminum used on the structure.

Some issues with the model that may require further investigation affected the springs. Unlike the standard model, the explicit model supports only tension and compression springs. This led to oscillations in the spring force that would not occur in a real tensegrity model with tension only members. One solution to this problem may be to use tension only members connected between struts instead of springs. Furthermore, it was assumed that the springs had no length limit, so the elasticity in some of the models may not be achievable with the actual hardware.

9.3 Simulation and Electrical Aspects of the Spherical Tensegrity

9.3.1 DC Gear Motors

The Pololu 172:1 metal DC gearmotors are arguably the most important electrical aspects of this project. They are integrated into the tensegrity structure and must withstand the 10 m drop and are also responsible for controlling the string length to expand and collapse the tensegrity for transport. They control the string length of the triangular faces of the 6 strut tensegrity by means of the spindle system described in earlier sections of the report.

In order to determine how the motors would perform in the structure, it was necessary to conduct an experiment to assess how much torque and current the motors could withstand without stalling.

The motors were tested by using a 6 V AC C-Clamp to fix a motor to a workbench. A spindle and string were then fixed to the motor shaft. In order to apply a force, increasing amounts of weight were attached to the string until the motor stalled. We attached a spindle and string to the motor shaft and a weight to the end of the string. We also powered the motor using a 6 V AC adaptor.

During the experiment, the motors stalled when a load of 29lbs was applied and ran with an average current of approximately 1.9A. When power was removed from the motor, the shaft of the motors would rotate and unspool at approximately 8.2 pounds of applied force.

9.3.2 Control Systems

The functioning prototype at the conclusion of this stage of the project used an Arduino Uno Microcontroller and three Arduino Motor Shields connected via a breadboard. This configuration does not allow independent control over each of the motors. The motor shields had two functions: to route current directly from the power source to the 6 DC motors and to act as an H-bridge allowing the motors to run in two directions for the collapse and expansion of the structure. Figure 46 shows the electrical system. Please note that the AC adapters see in this figure were not used in the final construction. Instead, only one AC adapter was used (to power the Arduino) and a 75W power supply. The power supply operated at 7V, and was capable of supplying 10A of current though this was higher than the required amount.

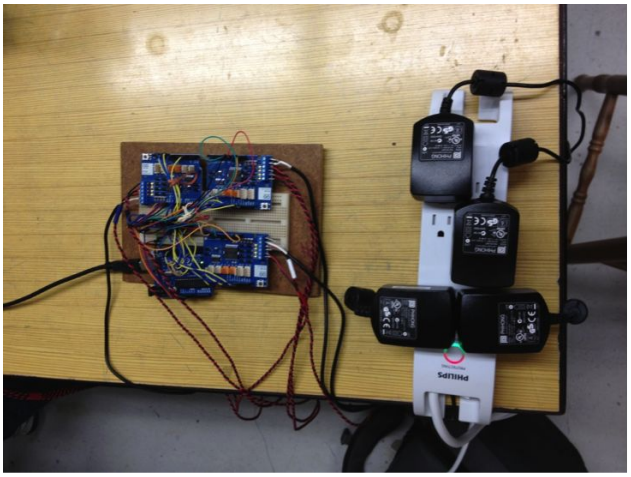

Figure 46: *Arduino Uno with Motor Shields and AC Adapters as a power source.*

A single channel, one-wire positional control scheme using an Arduino Mega 2560 was intended for the final prototype. The Mega 2560 has six different external interrupts and enough digital data pins to map encoder outputs. A single channel was envisioned originally to reduce complexity and resources used on the single Arduino control board but implementation showed that two-wire, two-channel encoder information was both possible using the single control board and necessary to obtain direction information.

10 Landing Structure Analysis

One of our biggest questions upon starting our Phase I study was how suitable a tensegrity structure would be as a landing platform for a NASA mission. More specifically we wanted to answer the following questions:

1. Can a tensegrity structure survive the impact of a hard landing impact of 15 m/s.
2. Can an actuated tensegrity structure still move after a landing impact of 15 m/s.
3. Can a tensegrity structure protect a delicate payload after a landing impact of 15 m/s.

To answer these questions we performed the following:

1. Performed extensive landing simulations using both a physics engine and an Euler-Lagrange Solver.
2. Dropped an actuated tensegrity from a height of 10 meters (landing speed of 15 m/s).
3. Dropped a tensegrity structure carrying an egg (simulated payload) from 10 meters.

We are glad to report that the tensegrity platform was successful at all three of our tasks.

10.1 Simulation of Landing

10.1.1 Landing Simulation using Bullet Simulator

To simulate landing and locomotion, we utilize a tensegrity simulator based on the Bullet physics engine. Bullet is an open source physics engine that does 3D collision detection, rigid and soft body dynamics in discrete time, though our simulator does not use the soft body dynamics. For the tensegrity simulation, we use the rigid body collisions provided by Bullet for compressional elements (rods of the structure), and we added simulation of tensional elements (strings) using basic physics for elastic strings. To be able to simulate both rigid bodies and tensional elements together, at each time step, all the forces applied by the strings to the rods are calculated in our own algorithms. These forces are then provided to the Bullet physics engine, and Bullet calculates the positions, orientations and velocities of all the rigid bodies considering previous states, tensional forces that we add, and possible collisions.

To simulate tensional forces, we use the rest length (L_R) and elasticity coefficient (c_e) of the strings that are defined as part of the material property. During the simulations, at each time step, the actual length (L_A) is extracted from Bullet, and if the string is stretched ($L_A > L_R$), the tensional force for each string is calculated using the elasticity formula $|F| = c_e * (L_A - L_R)$. On the other hand, if the string is slack ($L_A > L_R$) the force is accepted as zero (no compressional force caused by strings).

The resulting graphical illustration of the process is given at the Figure 48. As it can be seen on the left, before the moment of impact, all the strings are equally stretched. On the other hand, after the impact, the payload moves down further stretching some of the strings and temporarily deforming the structure.

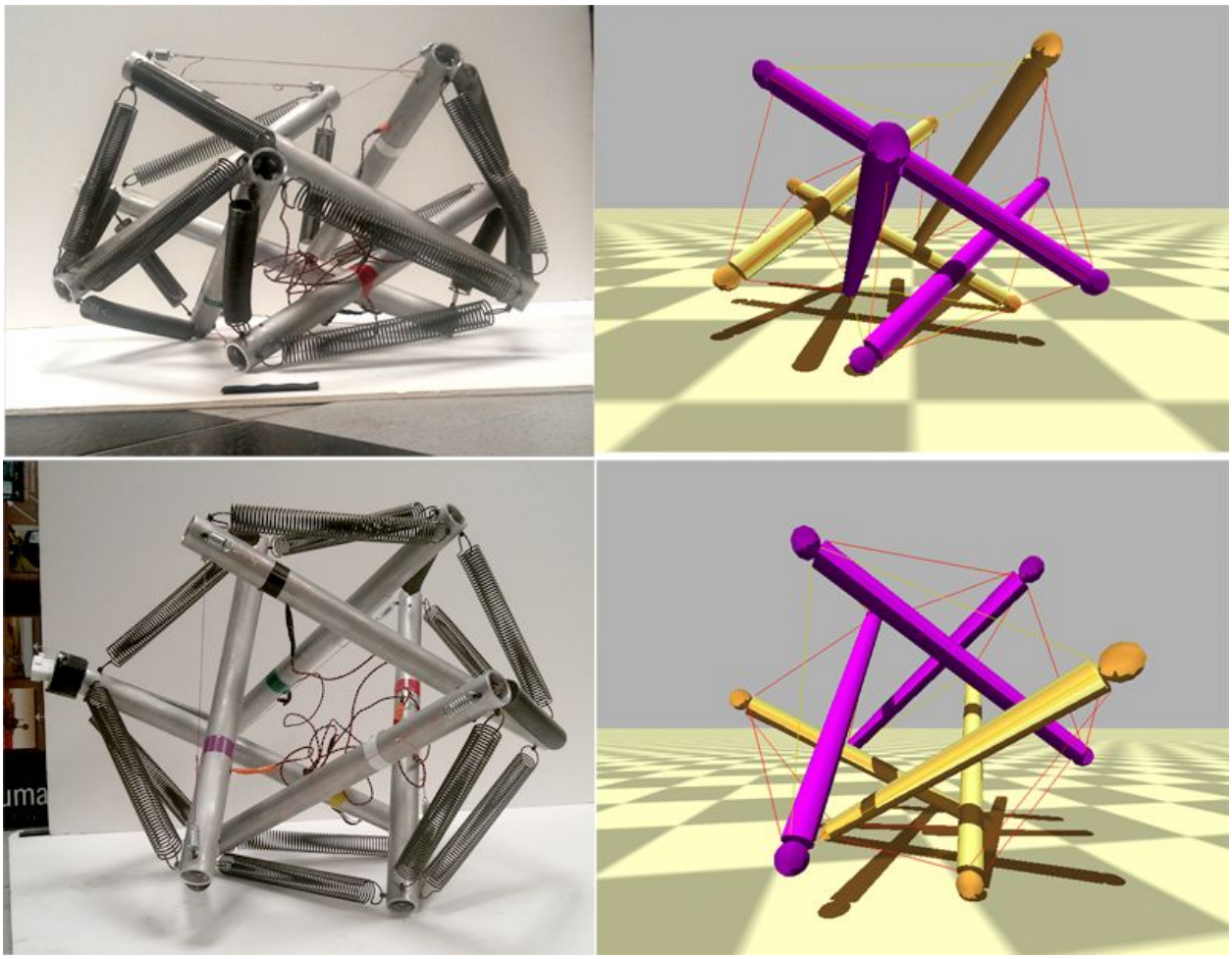

Figure 47: *We performed landing tests both in hardware and simulation.*

10.1.2 Landing Simulation using Euler-Lagrange (E-L) Solver

In order to verify the simulation results produced by our Bullet based simulator, we decided to compare the Bullet simulator to a published alalytic model for tensegrity systems. We choose to use Skelton's dynamic equations found in his *Tensegrity Systems* book [71] which is based on his work in [72]. In order to easily solve the dynamic equations with interactions with the environment, an Euler-Lagrange approach is used as well as Skelton's constrained class 1 structure. The lagrange equation for a constrained rod is given by

$$L = T - V - c \tag{30}$$

where

$$\mathbf{b} = l^{-1}(\mathbf{n}_j - \mathbf{n}_i) \tag{31}$$

$$c = \frac{\mathbf{J}\xi}{2}(\mathbf{b}^T\mathbf{b} - 1) \tag{32}$$

Equation (31) is the normalized vector of a rod with $\mathbf{n}_{i,j}$ the nodal positions in R^3, and equation (32) contains the lagrange multiplier ξ to keep (31) constrained. $\mathbf{J}$ is also defined as the inertia

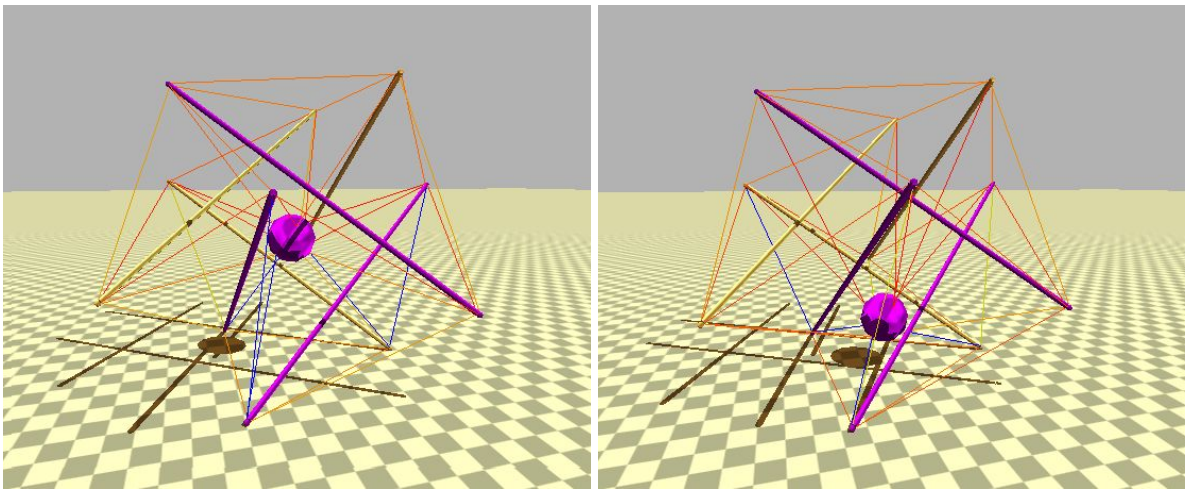

(a) Before Impact (b) After Impact

Figure 48: *Snapshot of the landing simulations using Bullet Physics Engine and Tensional Forces. The strings are colored according to their stretch / tension. After the impact the payload moves down stretching strings and temporarily deforming the structure.*

matrix for a 1 dimensional rod in 3 dimensional space. In order to define the system of k rods we need to define a combined Lagrangian as

$$\mathbf{L} = \sum_{i=1}^{k} L_i \tag{33}$$

where L_i is the Lagrange function for each rod. Using the approach outlined in Skelton's book for deriving the equations of motion, we can then derive the configuration matrix

$$\mathbf{Q} = \begin{bmatrix} \mathbf{R} & \mathbf{B} \end{bmatrix} \tag{34}$$

where $\mathbf{R}$ and $\mathbf{B}$ are matricies containing the translational and rotational vectors, respectively. They have the form

$$\mathbf{R} = \begin{bmatrix} \mathbf{r}_1 & \cdots & \mathbf{r}_k \end{bmatrix} \tag{35}$$

$$\mathbf{B} = \begin{bmatrix} \mathbf{b}_1 & \cdots & \mathbf{b}_k \end{bmatrix} \tag{36}$$

Also using the procedure to derive generalized forces within Skelton's book, the systems's generalized force equations are computed as

$$\mathbf{F_Q} = \begin{bmatrix} \mathbf{F_R} & \mathbf{F_B} \end{bmatrix} \tag{37}$$

with

$$\mathbf{F_R} = \begin{bmatrix} \mathbf{f}_{\mathbf{r}_1} & \cdots & \mathbf{f}_{\mathbf{r}_k} \end{bmatrix} \tag{38}$$

$$\mathbf{F_B} = \begin{bmatrix} \mathbf{f}_{\mathbf{b}_1} & \cdots & \mathbf{f}_{\mathbf{b}_k} \end{bmatrix} \tag{39}$$

Finally, we can define the resulting equations of motion in a compact form as

$$(\ddot{\mathbf{Q}} + \mathbf{Q}\boldsymbol{\Xi})\mathbf{M} = \mathbf{F}_{\mathbf{Q}} \tag{40}$$

where

$$\boldsymbol{\Xi} = diag\left[0, \cdots, 0, \xi_1, \cdots, \xi_k\right] \tag{41}$$

$$\mathbf{M} = diag\left[m_1, \cdots, m_k, J_1, \cdots, J_k\right] \tag{42}$$

This approach was then implemented in Python utilizing a 4th order Runge-Kutta formula for solving the system of ordinary differential equations. In order to implement a gravitational field, a force distribution function is applied along the length of each rod and calculated as a nodal force depending on the given density of the rod. This external force is then applied to the nodes during each time step, simulating a gravitational field.

10.1.3 Detailed Impact Simulations and Cross-Validation Using Two Simulators

We used these two simulators because they both have strengths and weaknesses. The Bullet simulator is the most general purpose, allowing us to explore control algorithms and complex environmental interactions, but it is an iterative discrete solver that we were concerned might not be providing accurate answers. The E-L solver, on the other hand, has a much stronger analytical basis and should provide very accurate answers, but is limited because some of the nodes (i.e. rod ends) must be constrained and locked into place. This is unrealistic for the deformation caused during landing, and makes it an inappropriate choice for mobility and controls research.

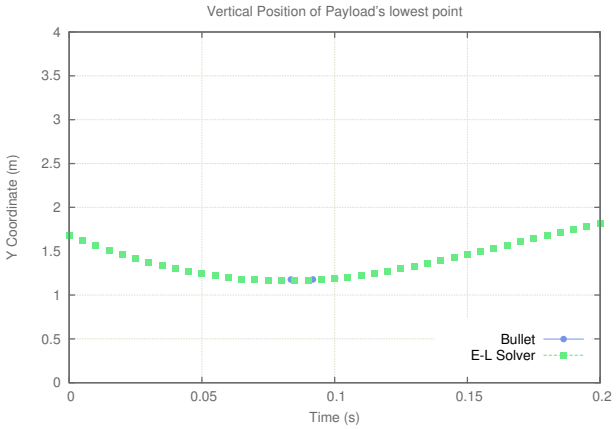

Figure 49: **Bullet vs EL: Vertical Position.**

In this section, we compare the Bullet simulator and E-L solver at the moment of impact with the ground. The simulations are compared at the moment of impact with the ground because our implementation of the analytic E-L solver requires select nodes to be constrained. We setup the structure so that it is barely in contact with the ground and is in balance at time equal to 0. In both simulations, we add an initial velocity equal to the terminal velocity of Titan, and compared each vertical trajectory, vertical velocity, and vertical acceleration of the payload. Since the structures

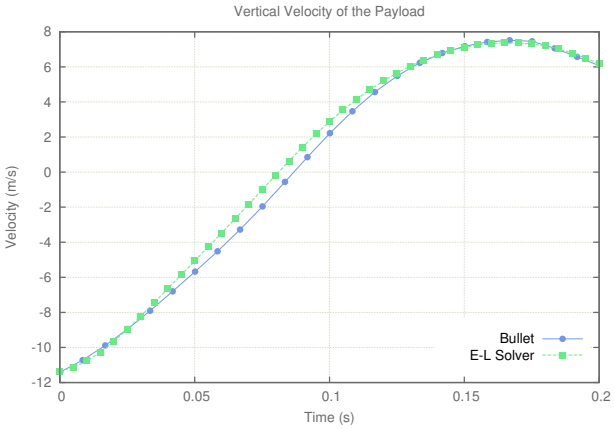

Figure 50: **Bullet vs EL Vertical Velocity.**

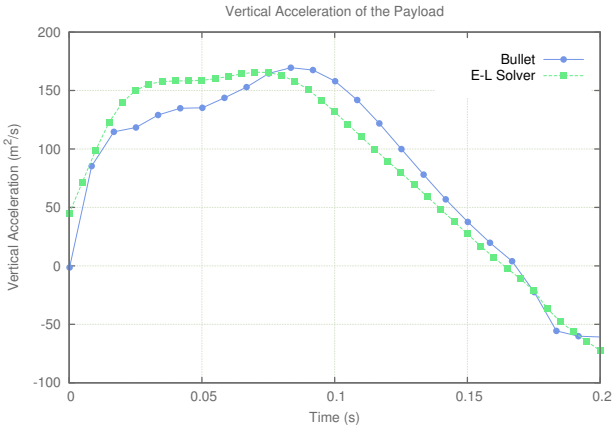

Figure 51: **Bullet vs EL Vertical Acceleration.**

horizontal speed is zero at the beginning and the structure is symmetrical, the payload's horizontal components of position, velocity and acceleration are zero. As it can be seen in the Figures 49 and 50, both simulators closely match and generate the same results for position and velocity with the error margin close to zero. Comparing the accelerations generated by two simulators (Figure 51) it can be seen that there is a bigger difference. The reason behind this difference is the fact that Bullet is a discrete time simulator and accelerations are calculated using two point estimations from velocities at the timestep before. Yet, even with these differences in accelerations, our conclusion at the end of the comparison is that both simulators showed the same basic dynamics and their results were close enough that we could move forward using the more general purpose Bullet Simulator for our controls, mobility, and landing experiments.

10.1.4 Comparing Simulators to Hardware

We are also interested in how the simulators compare with actual hardware. While a fully calibrated comparison between the hardware and the simulator is pending as future work once we have access to a motion capture system, we have made some initial casual comparisons. By taking the hardware parameters for the prototype described in Section 9 and making an exactly matching model in the Bullet simulator, we are able to command both the prototype and the simulated model to different positions. As can be seen in Figure 47, the results is visually similar and again supports the intuition that our simulators are generating the correct dynamics despite the challenges of modeling such complex and elastic structures.

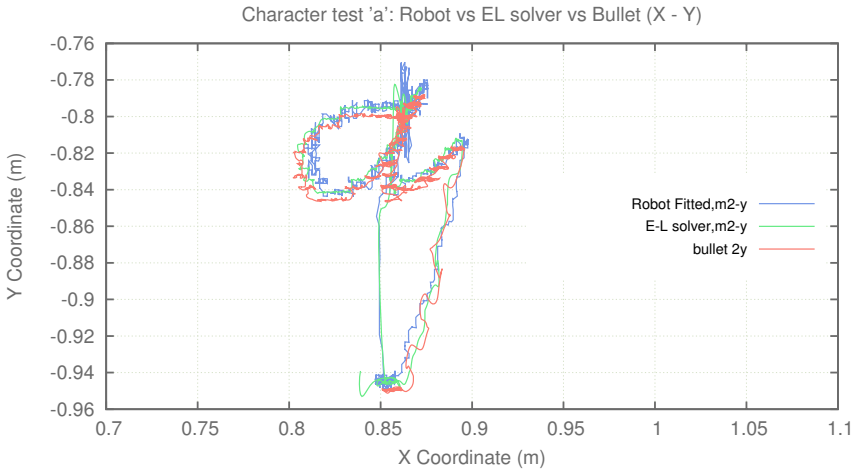

Figure 52: *Simulator Verification by tracing the letter "a" with one rod end in both simulators and with the hardware robot shown in Figure 61.*

An even more compelling cross-validation to hardware has come with the arrival of our visiting scientist Ken Caluwaerts from Belgium. He brought with him a prototype tensegrity robot which is very similar to our target design, which can be seen in Figure 61. While still in Europe he had

performed some motion capture tests with the robot tracing out different letters in the air with the end of one of the rods. We were able to replicate these tests with our simulators and compare results, which showed a very good match. Again, this is a preliminary verification, and further motion capture studies are warranted, but it gives us very strong confidence in our simulation tools.

10.1.5 Simulated Drop Tests and Payload Protection

Finally, we performed extensive analysis on drop tests and the protection provided to a payload. As expected, we found that by varying the rod lengths, which impacts the stroke distance for the payload to decelerate, we could control the maximum deceleration experienced by the payload while ensuring that it did not collide with the ground or structure. For example, with rods of 1.5 meters in length, our payload experienced a max deceleration of 21.4G when landing at 15 m/s. In figure 53 we show the results of a series of drop tests with different rod lengths and show the resulting maximum deceleration and forces experienced in the tension members. As can be seen from these graphs, even for reasonable rod lengths, the maximum G's are acceptable for most instruments, and the maximum forces experienced by the cables are easily within ranges that can be engineered for. In all tests we kept the total system mass constant, at 100kg (which is 70kg for the payload and 5kg per rod) in order to highlight the impact structural geometry and rod length. For the tension members we used spring constants of $44kN/m$ for the cables around the perimeter and $10kN/m$ for the cables attached to the payload. Also, the results in Figure 53 were found using the landing orientation of 35 degrees around X axis and 45 degrees around Z axis, which we selected from our orientation studies discussed below.

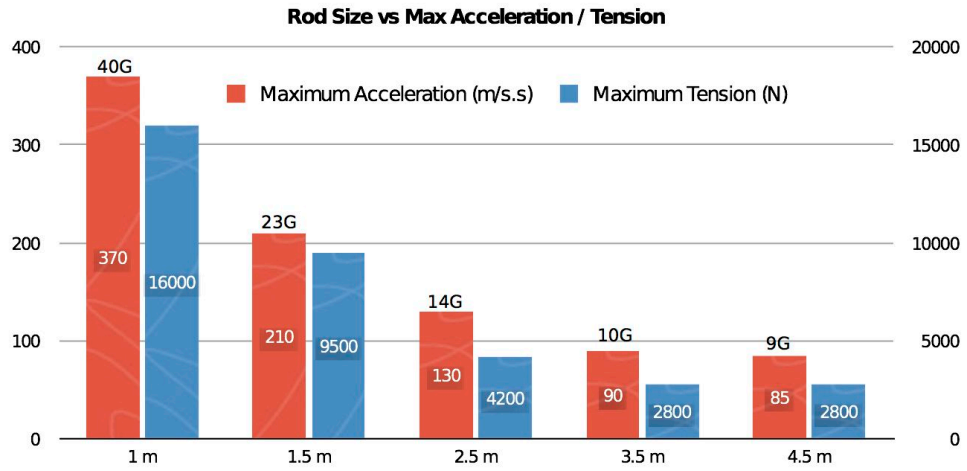

Figure 53: **Landing Forces Study**. *This shows how rod length impacts maximum deceleration of the payload and the maximum forces experienced by the tension cables. All tests were conducted with a landing velocity of 15 m/s onto a hard surface.*

A very interesting point to consider is that the mass of our system will grow in a linear fashion with the length in the rods, while providing increasing payload protection. On the other hand, the

mass of airbags increases with the square of the radius, which is one of the reasons that the MSL rover, with its increased size and mass, had to switch from the airbag approach used by MSL to the more complex Sky Crane approach. While this study has focused on small light-weight mission concepts, we look forward to phase two where we will explore how this system scales to handle larger payloads.

10.1.6 Landing Orientation Studies

In order to study how landing orientation affects payload decelerations and impact events, we conducted a systematic study of landing orientations. Since we wanted to get meaningful data, even for bad orientations, we used a larger tensegrity with 4 meter rods so the data wouldn't saturate. Our success criteria for this study was that the decelerations had to stay under an upper limit of 25G deceleration of the payload, and the payload had to avoid collision with the ground or parts of the tensegrity structure. Figure 54 shows the orientations that were safely within these criteria (black) or failed one or both of the criteria (colored). By using a simple trailing streamer during descent it would be possible to control landing at an optimal orientation and enable the use of smaller structures with shorter rods because the orientation control would maximize the available stroke for the payload to decelerate within the structure. Conversely, we can use these studies to know what the worst possible landing scenario will be and choose a structure size which will allow safe landing at any orientation.

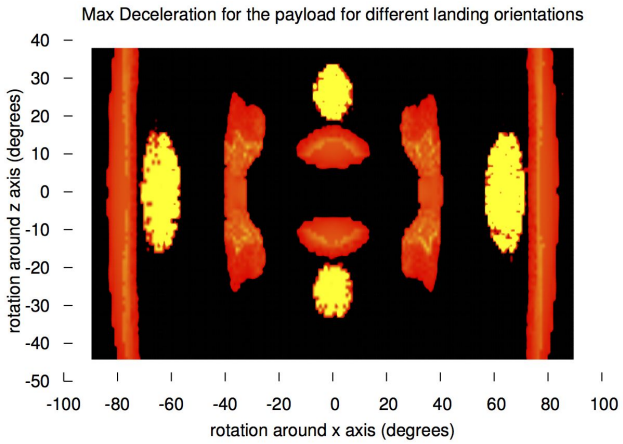

Figure 54: *Heat map of the maximum acceleration that the payload encounters for all possible landing orientations. Black areas are safe, colored areas are where the payload does not meet one or both success criteria.*

In addition to different orientations, we tested adding horizontal speeds during landing. Figure 55 shows the horizontal velocities above which the payload hits the rods that surrounds it. In this experiment, the orientation used is the same configuration as the previous landing experiment (35 degrees around X and 35 degrees around Z). As it can be seen, the structure can handle additional horizontal speeds up to 50 m/s. Depending on the direction of the speed, the structure can handle even more speeds.

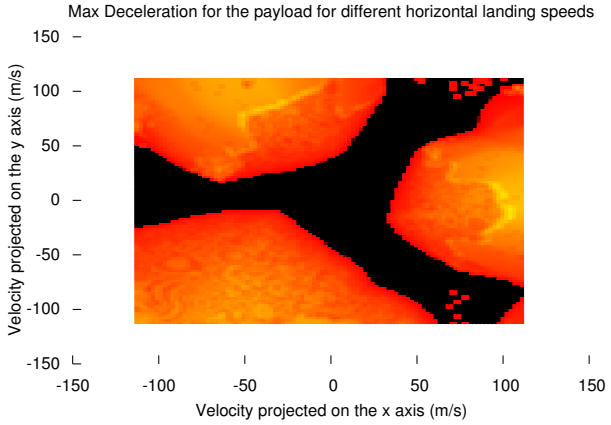

Figure 55: *Heat map of the maximum acceleration that the payload encounters for additional horizontal velocity, in addition to vertical terminal velocity. Black areas are safe, colored areas are where the payload does not meet a success criteria.*

10.2 Drop Test of Actuated Hardware Tensegrity

Once the prototype was built and deployment demonstrated, a series of drop tests were performed from successively greater heights until 10m was reached, at which point the prototype was landing at around 14 m/s, which is comparable to the terminal landing speed expected on Titan. After landing, the test was shown to be successful by demonstrating that the lander still functioned and could be collapsed to its packed state and once more deployed. In Figure 56 we show a sequence from the 7.5m drop test. During this landing, the probe rebounded and rolled sideways a distance about twice its diameter.

Figure 56: **Drop test from 7.5m.**

Most significantly, the probe survived the 10m drop test and was still functional afterwards, giving us confidence that this approach is viable, and that our simulation results are accurate enough to proceed to further analysis. One useful insight from this test is that the motors unspooled (i.e. were back driven) by a few centimeters during the landing. Thus, it is recommended that brakes be integrated to the motors, so they can be mechanically locked in place during landing.

Figure 57: **Drop test from 10m**. *Similar to terminal velocity on Titan.*

10.3 Drop Test of Hardware Tensegrity with Payload

The drop tests discussed above were focused on structure and the survivability of actuators and controllers, but those tests did not contain a centrally suspended payload. In the following drop tests, performed by a team of undergraduate mechanical engineers at UC Berkeley, the focus was to see how well a tensegrity structure would protect a payload, which in this case was simulated by using an egg. The structure was built using a Tensegritoy Kit which is composed of modular wooden rods and elastic cables for rapid prototyping. It is worth noting that the following tests were done with a different morphology of the tensegrity structure. While the rest of the report focuses on the 6-bar tensegrity, we had primarily chosen that one as it is the simplest form and would be the easiest to build and actuate. There are many morphologies of tensegrities which may be useful for landing and mobility, with different trade-offs of advantages and weaknesses. While the students in Idaho who built the first prototype found that the 30-bar tensegrity had low structural stiffness and reject that structure, we realize that the addition of a centrally suspended payload actually increases the structural stiffness. Furthermore, there are a number of design choices one can make to maximize the structures ability to absorb impact loads, as will be explained below.

10.3.1 Tensegrity Configuration

Initially, the Tensegritoy kit was assembled into the icosahedron tensegrity structure with pentagonal nodes. The testing payload, an egg, was inserted into the chamber made from cardboard tubing, and then suspended within the tensegrity structure using six of the Tensegritoy kits tension members (See Figure 58).

Starting the payload from an initial height of two feet, the tensegrity structure (as seen in Figures 58 and 60) was allowed to freely fall onto a flat surface. The results were recorded. In the cases where the payload was sufficiently protected and did not fail, the tensegrity structure would be dropped again from one foot higher than the previous drop. This was repeated until the failure of the payload, at which point the data would be recorded.

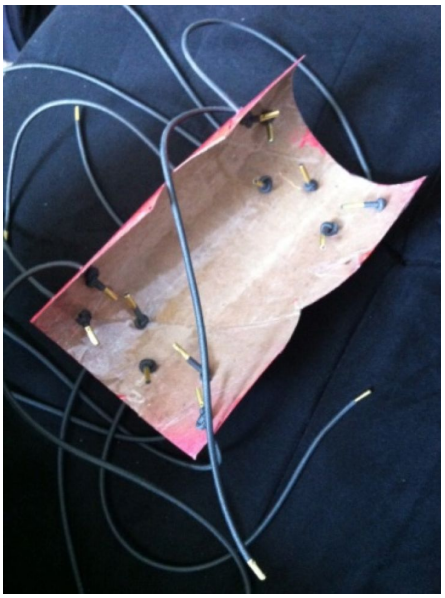

Figure 58: **Device Utilized to Suspend Payload (Egg) within Tensegrity Structure**.

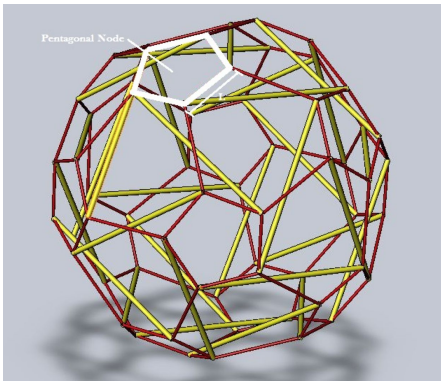

Figure 59: **3D Solidworks model of Tensegrity Structure**. *Highlighted is the pentagonal node with side length L.*

We tested two parameters. The first parameter involved tension in the payload suspension cables. Since the cables we used were fixed in length, the stiffness was changed by coiling the cable around the rod ends, with more coils causing the cable to shorten and stiffen. Thus, our metric for stiffness was the number of coils utilized in setting up the structure. The next parameter was the rigidity of the structure. This was configured through the size of the pentagonal nodes of the structure (see Figure 59), which was measured in terms of the length of the pentagons side; a smaller pentagonal node resulted in a more rigid structure.

Two sets of tests were run. The first set was run by maintaining suspension cable tension constant while changing pentagon size. Each experiment was run three times to account for noise as seen in Table 1.

The next set of experiments was run holding pentagon size constant while changing suspension cable tension. Each experiment was run three times to account for noise as seen in Table 2.

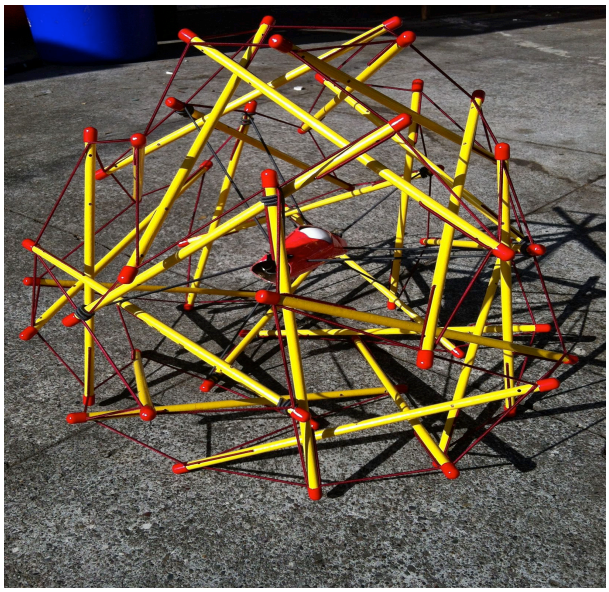
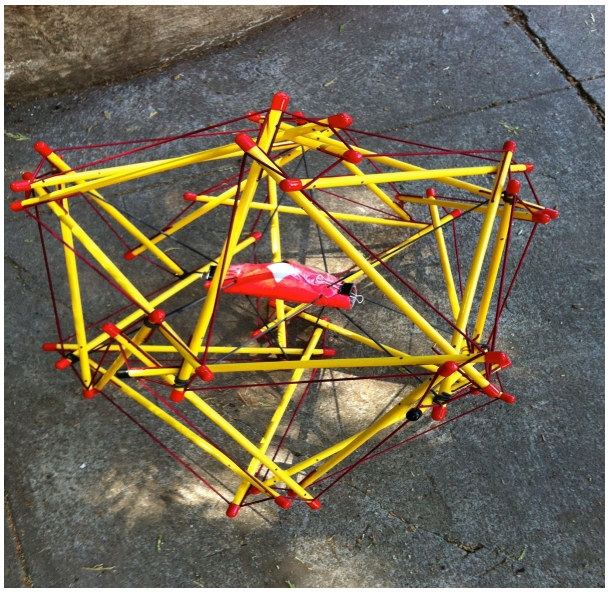

Figure 60: **Tensegrity Structures with Payloads (Egg) Suspended for Testing**. *Left: pentagonal nodes configured to have 3 inch sides and suspension cable tensions calibrated to 3 coils. Right: pentagonal nodes configured to have 1.5 inch sides and suspension cable tensions calibrated to 3 coils.*

Table 1: Testing Matrix 1

Suspension Cable Tension (Number of Coils)	Pentagon Size (length of side)
3	1.5 in
3	3.0 in
3	4.5 in

10.3.2 Results

Data gathered from experimentation is listed below in Tables 3 and 4. The most significant result is that with the right configuration of tensions and pentagon sizes, the payload (egg) was able to be dropped safely from almost 10m (31.67 ft = 9.65 m).

10.3.3 Droptest Evaluation

In order to understand the results of our measured parameters, it necessary to evaluate what constitutes payload protection. There are two main factors to consider: the maximal acceleration of the payload, and whether the payload collides with the structure itself. Both are determined by the vibrational mechanics of the payload, namely the natural oscillating frequency. If the oscillation frequency is too low, the payload will deflect more and collide with the structure. Inversely, if the

Table 2: Testing Matrix 2

Suspension Cable Tension (Number of Coils)	Pentagon Size (length of side)
2	3 in
3	3 in
4	3 in

Table 3: Results for Constant Tension

Suspension Cable Tension (Number of Coils)	Pentagon Size (length of side)	Failure Height	Failure Height Average
3	1.5 in	21/24/22 ft	22.33 ft
3	3 in	23/22/24 ft	23 ft
3	4.5 in	25/25/24 ft	24.67 ft

Table 4: Results for Constant Pentagon Size

Suspension Cable Tension (Number of Coils)	Pentagon Size (length of side)	Failure Height	Failure Height Average
2	3 in	6/4/6 ft	5.33 ft
3	3 in	23/22/24 ft	23 ft
4	3 in	34/31/30 ft	31.67 ft

oscillation frequency is too high, the payload will experience large accelerations that may break finely tuned instruments contained within.

Due to limitations in resources for this student project, the instrument used to measure protection in our experiment is an egg. The egg essentially measures the collision variable, as video footage shows most breaks occurred due to collisions between the payload and structure. The evidence is not decisive though; it may be that high accelerations caused pressure points on the egg from the casing containing it. In any case, future experimentation should include an accelerometer that accurately depicts dynamics of the payload.

Some variables to consider in the future are inherent in the design of the payload casing shape. Our cylindrical casing allowed some protection to the egg for axial collisions, while radial collisions with the structure directly imparted forces on the egg. Furthermore, due to the shape of the casing, we were unable to attach suspension cables to the center of the payload. As a result, the distribution of cables was not perfectly symmetric around the egg, causing variant spring coefficientsand thus natural frequenciesabout the egg. Both these factors imply that the orientation of the structure upon impact causes variable reactions of the payload.

The quantity and orientation of the suspension cables is another inherent design factor. Only a few nodes on the structure connected to the limited number of suspension cables. These nodes experienced unique forces due to both suspension cable pre-tensioning and payload oscillations. Additionally, the shape of the tensegrity as a whole deforms due these forces applied at only specific nodes. Thus different allowable deflections occur along differing axis due to the deformed shape. Again, these factors implicate that the structure is not symmetric in its distribution of forces and allowable deflections, and thus subject to variable reactions dependent upon orientation. For future designs, the ideal configuration would most likely be a spherical payload casing with symmetric suspension cables connecting to each node on the structure. This would eliminate the aforementioned imbalances that cause orientation-specific reactions. Note that the simulated payload drop tests reported earlier in this section used such a fully-connected symmetric payload suspension system.

In order to qualify the use of the egg as a proxy payload, we made some rough estimates of the drop velocities required to break an egg. From an online search, we found prior documented experiments on dropping eggs [1], which listed the heights at which an egg would break when dropped onto a hard surface (15 cm) and when dropped onto a cushioned surface (60 cm). From this one can calculate that an egg breaks when landing with a velocity of 1.7 m/s on a hard surface and 3.4 m/s on a cushioned surface. Thus, we see that in our best performing drop tests from around 10m that while the entire structure was landing with about 13.7 m/s velocity, the egg was experiencing an impact equivalent to about 2 m/s (assuming some minor padding from the casing). This is interesting because it matches the analysis shown in Figure **??**, though this is a different morphology for the tensegrity structure. This leads us to believe that there are many shapes of tensegrity structures which can provide the impact protection desired and further investigation into different morphologies is warranted as they may also provide different trade-offs with respect to packing, rod lengths, and mobility efficiency.

10.4 Conclusions from Landing Structure Analysis

In our landing analysis we developed and cross-validated two different simulation methods that allowed us to explore the capabilities of a tensegrity structure to absorb the forces of landing and to simultaneously protect a delicate payload. This analysis confirmed that indeed it is possible to do so using a 6-bar tensegrity probe while maintaining maximum decelerations experienced by the instrument-containing payload to forces less than 25G, despite the structure landing at 15 m/s (which is greater than terminal velocity on Titan). Within our scenarios in which the probe experienced a successful landing on Titan, the maximum acceleration applied to the payload was $180m/s^2(18.3G)$ and the minimum acceleration was $140m/s^2(14.3G)$. Comparing this to the Huygens probe's landing acceleration of $32G$ [45], the tensegrtiy probe will have a 43% reduction in G forces experienced by the scientific payload.

We also built a hardware prototype of this 6-bar tensegrity and performed drop-tests which showed that it was capable of surviving and operating after landing at these speeds. A useful insight from this test was that the motors should have mechanical brakes on them for the landing impact, as they were slightly back driven during landing. Finally, we performed more drop tests, now with a differently shaped 30-strut tensegrity, which carried a delicate payload (an egg) and which was shown to also be able to protect that payload after a 10 meter drop test. This final test highlighted the fact that there are a variety of different morphologies of tensegrities which may be able to accomplish our core goals. While we have extensively studied the simplest 6-bar tensegrity to prove the basic value of this approach, other morphologies may provide even better solutions to shock absorption, payload protection, packing efficiency, and mobility over rough terrain. We look forward to building on the initial positive results presented here exploring deeper into the optimal designs for tensegrity based probes.

11 Conclusions and Future Work

When this project was first proposed, the idea of using a tensegrity probe for planetary landing and mobility bordered on science fiction, and it has been our objective over the last year to determine if the concept was sound or if there were fundamental flaws. We are extremely pleased that after many forms of analysis, simulation, and prototype construction and testing we find that the concept is indeed sound and worthy of further research and engineering effort. Clearly there is much more to be done on both the technology and on the mission design fronts, but at this point we can safely make the following claims based on the work done:

- Tensegrities can be an effective landing and mobility platform for a Titan mission. Compared to existing flown missions, a tensegrity probe can have a high mass fraction between science payload and overall weight (as measured at atmospheric entry) due to its dual use as a landing system (like an airbag) and as a system for surface mobility. As a result, tensegrity based missions can be cheaper and open up new forms of surface exploration that take advantage of their natural tolerance to impacts.
- We demonstrated in our physics based simulator that tensegrity probes can be controlled effectively with evolutionary and dynamical algorithms resulting in robust smooth rolling motion over a variety of terrains.
- Using multiple analysis and simulation tools we showed that tensegrities are a very robust landing platform, and can protect delicate payloads from a landing impact of 15 m/s (and possibly beyond). This was further confirmed by performing drop tests on multiple physical prototypes.

In the process of our investigations we also developed multiple simulation and analysis tools which we cross-validated with each other and have even performed initial cross-validations with hardware prototypes. We now have strong confidence that these tools provide useful engineering data to us which we can use as we explore a greater range of morphologies and higher-fidelity prototypes capable of the full range of activities, from deployment, to landing, and surface mobility. This is a significantly valuable tool to have developed in Phase I, and will enable our Phase II study to make significant progress on maturing this technology to TRL 3. Looking to a future Phase II effort, we will be going beyond just answering the question of "are tensegrity probes *possible*" to answering the question "are tensegrity probes *practical.*" To accomplish this, there are three primary aspects to be matured:

- **Prototype for Mobility** and refined engineering analysis.
- **Explore Other Morphologies** and associated controls and capabilities.
- **Refine Mission Design**, such as thermal and power issues, and extend concept to other solar system targets, including low gravity locations (NEO's).

Mobility Prototype: In terms of maturing the core technologies our highest priority is to build a fully actuated terrestrial prototype which expresses all the core aspects of the Titan mission,

from deployment, to landing, to surface mobility, while safely protecting an engineering payload (i.e. instrumented to measure experienced forces and accelerations). This prototype will give us critical insights into the detailed engineering required for such a mission and further refining our estimations of the mass fraction of productive science equipment compared to overall system mass. This next prototype will be designed to be light-weight and modular. In this way it will be similar to the extremely light-weight carbon-fiber tensegrity robot (Figure 61) developed by Ken Caluwaerts, a visiting scientist from Ghent University, Belgium, who brought his robot to our lab. This tensegrity robot, with 1 meter long rods and six actuators, weighs only slight more than 1 kg. A key aspect of the design of the next prototype will be to develop a modular approach to the rods of the tensegrity. The intention is to make modular end-caps which house the actuation and sensing such that they can easily be placed onto rods of varying lengths and can be assembled into tensegrities of different morphologies. While our initial focus will be to build a prototype of the 6-strut version studied in Phase I, so that we can fully verify our control algorithms, we have evidence from our current study that other morphologies may provide enhanced capabilities, as will be explored in our second task.

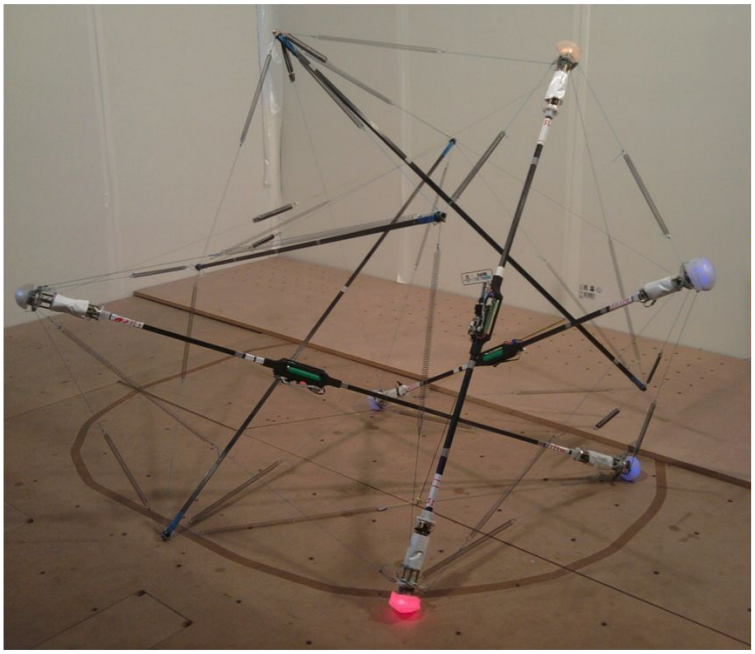

Figure 61: **Light-weight Design**. *Our Phase II prototype will incorporate design insights from this extremely light-weight carbon-fiber tensegrity robot developed by Ken Caluwaerts, a visiting scientist from Ghent University, Belgium. This robot was developed with support from a Ph.D. fellowship of the Research Foundation-Flanders (FWO) and the European Community's Seventh Framework Program FP7/2007-2013 Challenge 2 Cognitive Systems, Interaction, Robotics under grant agreement No. 248311-AMARSi.*

Explore Morphologies and Controls: In Phase I we primarily focused on the simplest morphology, the 6 strut icosahedron, to make our initial analysis easier. Yet there is a wide range of possible shapes and configurations of tensegrity probes, and some of our experiments have shown that these other morphologies may provide a better balance of properties to support the full mission profile. Thus, the second task in phase two will be to explore other morphologies in depth (in simulation

and in hardware as appropriate) and evaluate the trade-offs between packing efficiency, landing performance, and an expanded list of mobility and control issues. The new mobility and controls areas we would like to explore include the ability to crawl up steep hills, reshape the structure to avoid getting stuck, dig into low traction surfaces for mobility or to trench the regolith for science investigations, and to change shape to position instruments directly attached to the structure.

Refine Mission Design and Extend to Other Targets: Building on the insights gained from our first two tasks, we will be able to further refine our estimates of a full mission design and better constrain our mass estimates which we use to evaluate the system mass fraction of productive scientific payload compared to the full system mass delivered to orbital entry. In the process we will also investigate two critical mission design aspects: Thermal Analysis and Power. While full mission engineering of thermal and power issues is out of scope at this point in the technology development, we will focus on appropriate material choices for our tension elements with the capability to provide flexibility and elasticity in the cold thermal environment of Titan. Likewise, our mobility research until now has focused on the possibility of controls - so next we will investigate the power consumption required, possible efficiency gains, and use that information to further refine the mission design for power generation and storage.

Along with maturing our Titan mission design details, we will also explore the application of the tensegrity probe concept to other destinations. The most obvious step is to explore the upper limits of possible landing speeds and identify other bodies within the solar system which may be candidate targets for tensegrity probe missions. A very intriguing point to consider is that the mass of our system will grow in a linear fashion with the length in the rods, while providing increasing payload protection. On the other hand, the mass of airbags increases with the square of the radius, which is one of the reasons that the MSL rover, with its increased size and mass, had to switch from the airbag approach used by the MER rovers to the more complex Sky Crane approach. While this study has focused on small light-weight mission concepts, we look forward to Phase II where we will also explore how this system scales to handle larger payloads.

Another exciting variant on the current technology we will investigate is the use of tensegrity probes for landing and exploring small airless bodies such as Near Earth Objects (NEOs). Recent results in our lab indicate that through a combination of the natural compliance of the tensegrity probe and with active control of the cables, the probes may be able to actively deform and thereby dissipate residual contact energies encountered when trying to land on micro-gravity targets. This would result in a compliant "gripping" probe which lands and deforms, sticking to the NEO, rather than bouncing off of it in an uncontrolled manner. (Figure 62) We have also observed that our probes can passively transfer kinetic energy into rotational energy, giving another means of managing micro-gravity landing events safely. Finally, our work on alternate mobility approaches for tensegrity robots leads us to expect that a properly designed probe could traverse the surface of a NEO much like a rock-climber, expanding and wedging itself between surface features, utilizing its capability for a wide range of deformations and shape control.

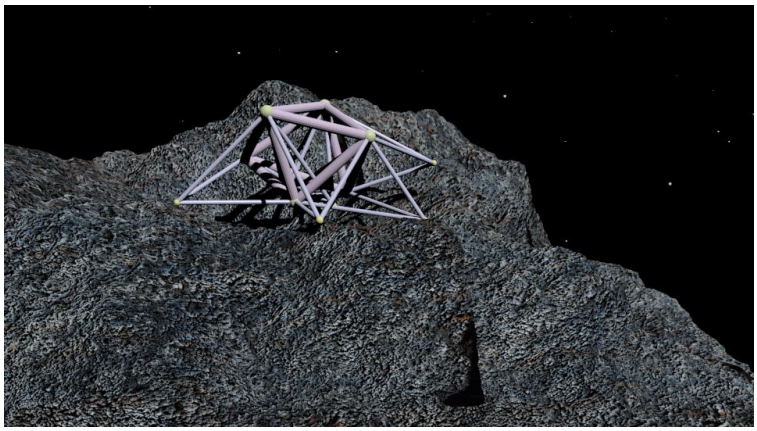

Figure 62: **Tensegrity Asteroid Mission**. *Tensegrity probes may be able to land on low-gravity astroids by dynamically absorbing residual impact forces through controlled compliance and deformation, thus enabling them to be "sticky" and not bounce away.*

12 Acknowledgements

As part of our Phase I study, we directed and collaborated with numerous students in our labs and at Universities around the Nation, and were honored to work with two International Visiting Researchers who were inspired to donate their time contributing fundamental research to this exciting project. The goals of our study were very broad and ambitious, covering many disciplines, and we greatly appreciate the work done by these teams in helping bring this study together. This projects success has also been strongly supported by Terry Fong and all the members of the Intelligent Robotics Group at NASA Ames Research Center. Thank You!

Work performed at Intelligent Systems Division (NASA Ames)

- Atil Iscen, Oregon State University. Atil contributed heavily to the evolutionary controls and simulated landing analysis.
- Jonathan Bruce, UC Santa Cruz. Jonathan contributed heavily to the simulated landing analysis and comparison of simulators.
- Steve Burt, UC Santa Cruz. Steve developed forward and inverse kinematic algorithms for general purpose tensegrity structures.
- In Won Park, Post Doc. In Won provided insights from related tensegrity projects and provided lab management support.

Visiting International Researchers

- Jeremie Despraz, Ecole Polytechnique Federale De Lausanne (EPFL), Switzerland. Jeremie developed the dynamical and CPG based controls. Jeremie's time is support by his Masters Program in the EPFL Biorobotics Laboratory, run by Prof. Auke Ijspeert.

- Ken Caluwaerts, Ghent University, Belgium. Ken contributed to the E-L Simulator, landing analysis, and engineering designs. Ken's time is support from a Ph.D. fellowship of the Research Foundation-Flanders (FWO) and the European Community's Seventh Framework Program FP7/2007-2013 Challenge 2 Cognitive Systems, Interaction, Robotics under grant agreement No. 248311-AMARSi.

Case Western Reserve University

- Brian Tietz, supported by a NASA Space Technology Research Fellowship (NSTRF) focused on a related Tensegrity Spine project, Brian has developed significant portions of the Tensegrity Simulator built ontop of the Bullet Physics Engine.

University of Idaho The students at the University of Idaho performed analysis, design, and construction of a deployable tensegrity probe which they then successfully tested by dropping from 10 meters. Their work was supported by the NASA Idaho Space Grant Consortium.

- **Undergraduates**
  - Mogley Samter - Biosystems Engineering
  - Sarah Lynn - Mechanical Engineering, Physics
  - Karen Jolley - Computer Engineering, Physics
  - Joe Hepner - Mechanical Engineering
  - Kyle Morse - Mechanical Engineering
  - Nathan Clark - Electrical Engineering
- **Graduate Mentors**
  - George Korbel - Mechanical Engineering
  - Sophie Milam - Mechanical Engineering

University of California at Berkeley The students from Berkeley conducted the analysis and drop tests of the egg-payload.

- **Undergraduates**
  - Andrew Deng - Mechanical Engineering
  - Grant Paulson - Mechanical Engineering
  - Jon Saltz - Mechanical Engineering
  - Anton Savinov - Mechanical Engineering
- **Graduate Mentor**
  - Andrew Sabelhaus - Mechanical Engineering

References

[1] Egg drop breakage experiments: http://professionaldevelopment.ibo.org/files/ocd/egg_dropping_activity.pdf.

[2] Tensegrity based probes for planetary exploration: Entry, descent and landing (edl) and surface mobility analysis. *To Appear in International Journal of Planetary Probes*, July 2013.

[3] A. Agogino and K. Tumer. Distributed evaluation functions for fault tolerant multi rover systems. In *Proceedings of the Genetic and Evolutionary Computation Conference*, Seattle, WA, July 2006.

[4] J. B. Aldrich and R. E. Skelton. Backlash-free motion control of robotic manipulators driven by tensegrity motor networks. *IEEE Conference on Decision And Control*, pages 2300–2306, 2006.

[5] N. Bel Hadj Ali and et al. Design optimization and dynamic analysis of a tensegrity-based footbridge. *Engineering Structures*, 32:3650–3659, 2010.

[6] T. Bliss. Central pattern generator control of a tensegrity swimmer. *Ph.D. thesis, Dept. Mech. Aerosp. Eng., Univ. Virginia,*, December 2011.

[7] T. Bliss, J. Werly, T. Iwasaki, and H. Bart-Smith. Experimental validation of robust resonance entrainment for CPG-controlled tensegrity structures. *IEEE Transactions On Control Systems Technology*, 2012.

[8] T. K. Bliss, T. Iwasaki, and H. Bart-Smith. CPG Control of a Tensegrity Morphing Structure for Biomimetic Applications. *Advances in Science and Technology*, 58:137–142, 2008.

[9] V. Böhm, A. Jentzsch, T. Kaufhold, F. Schneider, and K. Zimmermann. An approach to compliant locomotion systems based on tensegrity structures. *56th International Scientific Colloquium, Ilmenau University of Technology*, pages 1–6, August 2011.

[10] A. S. Boxerbaum, A. D. Horchler, K. M. Shaw, H. J. Chiel, and R. D. Quinn. A controller for continuous wave peristaltic locomotion. *2011 IEEE/RSJ International Conference on Intelligent Robots and Systems*, pages 197–202, September 2011.

[11] BulletPhysicsEngine. http://www.bulletphysics.org/, 2013.

[12] A. Büschges, T. Akay, J. P. Gabriel, and J. Schmidt. Organizing network action for locomotion: insights from studying insect walking. *Brain research reviews*, 57(1):162–71, January 2008.

[13] M. Calisti, A. Arienti, F. Renda, G. Levy, B. Hochner, B. Mazzolai, P. Dario, and C. Laschi. Design and development of a soft robot with crawling and grasping capabilities. In *Robotics and Automation (ICRA), 2012 IEEE International Conference on*, pages 4950–4955. IEEE, 2012.

[14] G. Chalkiadakis and C. Boutilier. Coordination in multiagent reinforcement learning: A bayesian approach. In *Proceedings of the Second International Joint Conference on Autonomous Agents and Multiagent Systems (AAMAS-03)*, Melbourne, Australia, July 2003.

[15] KC Clausen, H Hassan, M Verdant, P Couzin, G Huttin, M Brisson, C Sollazzo, and J-P Lebreton. The huygens probe system design. In *The Cassini-Huygens Mission*, pages 155–189. Springer, 2003.

[16] Fascia Research Congress. http://www.fasciacongress.org/2012/about-the-conference/.

[17] MR Darrach, R Kidd, JA MacAskill, A Chutjian, J Simcic, E Neidholdt, M Sinha, and B Bae. An overview of mass spectroscopy based instrument development at the jet propulsion laboratory. mr. *LPI Contributions*, 1683:1114, 2012.

[18] Sarah Degallier and Auke Ijspeert. Modeling discrete and rhythmic movements through motor primitives: a review. *Biol. Cybern.*, 103(4):319–338, October 2010.

[19] T. G. Dietterich. Hierarchical reinforcement learning with the maxq value function decomposition. *Journal of Artificial Intelligence*, 13:227–303, 2000.

[20] Tom Flemons. The bones of tensegrity. *http://www.intensiondesigns.com/bones_of_tensegrity.html*, 2012.

[21] Buckminster Fuller. Tensegrity. *Portfolio and Art News Annual*, 4:112–127, 1961.

[22] Matthew P Golombek. The mars pathfinder mission. *Journal of geophysical research*, 102(E2):3953–3965, 1997.

[23] J Gomez-Elvira and REMS Team. Environmental monitoring station for mars science laboratory. *LPI Contributions*, 1447:9052, 2008.

[24] A. Graells Rovira and J. M. Mirats-Tur. Control and simulation of a tensegrity-based mobile robot. *Robotics and Autonomous Systems*, 57(5):526–535, May 2009.

[25] C. Guestrin, M. Lagoudakis, and R. Parr. Coordinated reinforcement learning. In *Proceedings of the 19th International Conference on Machine Learning*, 2002.

[26] K. E. Herkenhoff, S. W. Squyres, J. F. Bell, J. N. Maki, H. M. Arneson, P. Bertelsen, D. I. Brown, S. A. Collins, A. Dingizian, S. T. Elliott, W. Goetz, E. C. Hagerott, A. G. Hayes, M. J. Johnson, R. L. Kirk, S. McLennan, R. V. Morris, L. M. Scherr, M. A. Schwochert, L. R. Shiraishi, G. H. Smith, L. A. Soderblom, J. N. Sohl-Dickstein, and M. V. Wadsworth. Athena microscopic imager investigation. *Journal of Geophysical Research: Planets*, 108(E12), 2003.

[27] KE Herkenhoff, SW Squyres, JF Bell III, JN Maki, HM Arneson, P Bertelsen, DI Brown, SA Collins, A Dingizian, ST Elliott, et al. Athena microscopic imager investigation. *Journal of Geophysical Research*, 108(E12):8065, 2003.

[28] C. HolmesParker and A. Agogino. Agent-based resource allocation in dynamically formed cubesat constellations. In *Proceedings of the Tenth International Joint Conference on Autonomous Agents and Multi-Agent Systems*, Taipei, Taiwan, May 2011.

[29] A Ijspeert. Central pattern generators for locomotion control in animals and robots: A review. *Neural Networks*, 21:642–653, May 2008.

[30] A. J. Ijspeert. Central pattern generators for locomotion control in animals and robots: a review. *Neural networks : the official journal of the International Neural Network Society*, 21(4):642–53, May 2008.

[31] D. E. Ingber. The architecture of life. *Scientific American*, 278(1):48–57, 1998.

[32] Donald E. Ingber. Cellular tensegrity: defining new rules of biologic design that govern cytoskeleton. *Journal of Cell Science*, 104:613–627, 1993.

[33] A. Iscen, A. Agogino, V. SunSpiral, and K. Tumer. Learning to control complex tensegrity robots. In *To appear in: Twelfth International Conference on Autonomous Agents and Multiagent Systems*, 2013.

[34] Atil Iscen, Adrian Agogino, Vytas SunSpiral, and Kagan Tumer. Controlling tensegrity robots through evolution. In *Genetic and Evolutionary Computation Conference (GECCO 2013)*, Amsterdam, NL, 2013.

[35] Atil Iscen, Adrian Agogino, Vytas SunSpiral, and Kagan Tumer. Learning to control complex tensegrity robots. In *Proceedings of the 2013 international conference on Autonomous agents and multi-agent systems*, AAMAS '13, pages 1193–1194, Richland, SC, 2013. International Foundation for Autonomous Agents and Multiagent Systems.

[36] Atil Iscen, Adrian Agogino, Vytas SunSpiral, and Kagan Tumer. Robust distributed control of rolling tensegrity robot. In *The Autonomous Robots and Multirobot Systems (ARMS) workshop at AAMAS 2013*, 2013.

[37] H. Klimke and S. Stephan. The making of a tensegrity tower. In *IASS Symposium*, Montpellier, 2004.

[38] Y. Koizumi, M. Shibata, and S. Hirai. Rolling Tensegrity Driven by Pneumatic Soft Actuators. *Robotics*, pages 1988–1993, 2012.

[39] Y. Koizumi, M. Shibata, and S. Hirai. Rolling tensegrity driven by pneumatic soft actuators. In *Robotics and Automation (ICRA), 2012 IEEE International Conference on*, pages 1988–1993. IEEE, 2012.

[40] B. Laub and E. Venkatapathy. Thermal protection system technology and facility needs for demanding future planetary missions. In *International Workshop on Planetary Probe Atmospheric Entry and Descent Trajectory Analysis and Science*, pages 268–278, Oct 2003.

[41] Darlene Lee. The mission loads environment and structural design of the mars science laboratory. 2012.

[42] S. M. Levin. The tensegrity-truss as a model for spine mechanics: biotensegrity. *Journal of Mechanics in Medicine and Biology*, 2:375–388, 2002.

[43] Stephen Levin. The tensegrity-truss as a model for spine mechanics. *Journal of Mechanics in Medicine and Biology*, 2:375–388, 2002.

[44] Mary K. Lockwood, Eric M. Queen, David W. Way, Richard W. Powell, Karl Edquist, Brett W. Starr, Brian R. Hollis, Vincent E. Zoby, Glenn A. Hrinda, and Robert W. Bailey. Aerocapture Systems Analysis for a Titan Mission. Technical report, NASA Langley Research Center, Feb 2011.

[45] RD Lorenz. Huygens probe impact dynamics. *ESA Journal*, 18:93–117, 1994.

[46] J. N. Maki, D. Thiessen, A.Pourangi, P. Kobzeff, T. Elliott L. Scherr and, A. Dingizian, and Beverly St. Ange. The mars science laboratory (msl) navigation cameras (NAVCAMS). In *42nd Lunar and Planetary Science Conference*, pages 268–278, 2011.

[47] JN Maki, D Thiessen, A Pourangi, P Kobzeff, L Scherr, T Elliott, A Dingizian, and B St Ange. The mars science laboratory (msl) navigation cameras (navcams). In *Lunar and Planetary Institute Science Conference Abstracts*, volume 42, page 2738, 2011.

[48] M. Masic and et al. Algebraic tensegrity form-finding. *International Journal of Solids and Structures*, 42:4833–4858, 2005.

[49] M. Masic and R. E. Skelton. Open-loop control of class-2 tensegrity towers. *Proceedings of the 11th Smart Structures and Materials Conference*, 5383:298–308, 2004.

[50] J. M. Mirats-Tur. On the movement of tensegrity structures. In *International Journal of Space Structures*, volume 25, 2010.

[51] K. W. Moored, III, S. A. Taylor, and H. Bart-Smith. Optimization of a Tensegrity Wing for Biomimetic Applications. *Proceedings of SPIE*, 6173:617313, March 2011.

[52] Thomas W. Myers. Dissection of the anatomy trains: http://www.anatomytrains.com/explore/dissection.

[53] Thomas W. Myers. *Anatomy Trains: Myofascial Meridians for Manual and Movement Therapists, 2nd Edition*. Churchill Livinstone, Edinburgh, 2009.

[54] Erik N Nilsen. Exploring mars: an overview. 2012.

[55] O. Orki. *A Model Of Caterpillar Locomotion Based On Assur Tensegrity Structures*. PhD thesis, Tel Aviv University, 2012.

[56] O. Orki, A. Ayali, O. Shai, and U. Ben-Hanan. Modeling of caterpillar crawl using novel tensegrity structures. *Bioinspiration & Biomimetics*, 7(4):046006, 2012.

[57] O. Orki, O. Shai, A. Ayali, and U. Ben-Hanan. A Model of Caterpillar Locomotion Based on Assur Tensegrity Structures. *Proceedings of the ASME 2011 IDETC/CIE*, August 2011.

[58] Liviu Panait, Karl Tuyls, Sean Luke, and Pack Kaelbling. Theoretical advantages of lenient learners: An evolutionary game theoretic perspective. *Journal of Machine Learning Research*, page 2008.

[59] C. Paul, H. Lipson, and F. J. V. Cuevas. Evolutionary form-finding of tensegrity structures. *Proceedings of the 2005 Genetic and Evolutionary Computation Conference (GECCO)*, pages 3–10, 2005.

[60] C. Paul, J. W. Roberts, H. Lipson, and F. J. V. Cuevas. Gait production in a tensegrity based robot. In *Advanced Robotics, 2005. ICAR '05. Proceedings., 12th International Conference on*, January 2005.

[61] C. Paul, F. J. Valero-Cuevas, and H. Lipson. Design and control of tensegrity robots for locomotion. *IEEE Transactions on Robotics*, 22(5), October 2006.

[62] K. Pearson. Role of sensory feedback in the control of stance duration in walking cats. *Brain research reviews*, 57(1):222–7, January 2008.

[63] Schleip R, T. W. Findley, L. Chaitow, and P. Huijing, editors. *Fascia: The Tensional Network of the Human Body: The science and clinical applications in manual and movement therapy, 1e*. Churchill Livingstone, 1 edition, April 2012.

[64] A. L. Ridgel and R. E. Ritzmann. Effects of neck and circumoesophageal connective lesions on posture and locomotion in the cockroach. *Journal of comparative physiology. A, Neuroethology, sensory, neural, and behavioral physiology*, 191(6):559–73, June 2005.

[65] J. Rieffel, R. Stuk, F. Valero Cuevas, and H. Lipson. Locomotion of a Tensegrity Robot via Dynamically Coupled Modules. *Proceedings of the International Conference on Morphological Computation*, 2007.

[66] J. Rieffel, B. Trimmer, and H. Lipson. Mechanism as Mind : What Tensegrities and Caterpillars Can Teach Us about Soft Robotics The Manduca Sexta Caterpillar : Morphological Communication in Tensegrity Robots. *Artificial Life*, pages 506–512, 2008.

[67] J. A. Rieffel, F. J. Valero-Cuevas, and H. Lipson. Morphological communication: exploiting coupled dynamics in a complex mechanical structure to achieve locomotion. *Journal of the Royal Society, Interface / the Royal Society*, 7(45):613–21, April 2010.

[68] M. Shibata and S. Hirai. Rolling Locomotion of Deformable Tensegrity Structure. *Mobile Robotics: Solutions and Challenges*, pages 479–486, 2009.

[69] M. Shibata and S. Hirai. Moving strategy of tensegrity robots with semiregular polyhedral body. In *Proc. of the 13th Int. Conf. Climbing and Walking Robots (CLAWAR 2010), Nagoya*, pages 359–366, 2010.

[70] M. Shibata, F. Saijyo, and S. Hirai. Crawling by body deformation of tensegrity structure robots. In *Robotics and Automation, 2009. ICRA '09. IEEE International Conference on*, pages 4375 –4380, may 2009.

[71] R. E. Skelton and M. C. De Oliveira. *Tensegrity Systems*. Springer, 2009 edition, June 2009.

[72] Robert Skelton. Dynamics and control of tensegrity systems. In H. Ulbrich and W. Gnthner, editors, *IUTAM Symposium on Vibration Control of Nonlinear Mechanisms and Structures*, volume 130 of *Solid Mechanics and its Applications*, pages 309–318. Springer Netherlands, 2005.

[73] Robert E. Skelton and Mauricio C. Oliveria. *Tensegrity Systems*. Springer, New York, 2009.

[74] Kenneth Snelson. http://www.kennethsnelson.net/.

[75] Kenneth Snelson. Continuous tension, discontinuous compression structures. united states patent 3169611, Feburary 1965.

[76] P. Stone, R. S. Sutton, and G. Kuhlmann. Reinforcement learning for RoboCup-soccer keepaway. *Adaptive Behavior*, 2005.

[77] Tibert and et al. Review of form-finding methods for tensegrity structures. *International Journal of Space Structures*, 18:209–223, 2003.

[78] Brian R Tietz, Ross W Carnahan, Richard J Bachmann, Roger D Quinn, and Vytas Sunspiral. Tetraspine : Robust Terrain Handling on a Tensegrity Robot Using Central Pattern Generators. In *2013 IEEE/ASME Advanced Intelligent Mechatronics*. IEEE, July 2013.

[79] K. Tumer and A. Agogino. Distributed agent-based air traffic flow management. In *Proceedings of the Sixth International Joint Conference on Autonomous Agents and Multi-Agent Systems*, pages 330–337, Honolulu,HI, May 2007. **Best Paper Award**.

[80] K. Tumer and D. Wolpert, editors. *Collectives and the Design of Complex Systems*. Springer, New York, 2004.

[81] J. M. Mirats Tur and S. H. Juan. Tensegrity frameworks: Dynamic analysis review and open problems. *Mechanism and Machine Theory*, 44:1–18, 2009.

[82] J.M.M. Tur. On the movement of tensegrity structures. *International Journal of Space Structures*, 25(1):1–14, 2010.

[83] Katja Verbeeck, Maarten Peeters, Ann Nowe, and Karl Tuyls. Reinforcement learning in stochastic single and multi-stage games. In *Adaptive Agents and Multi-Agent Systems II, Lecture Notes in Artificial Intelligence*, pages 275–294. Springer Verlag, Berlin, 2005.

[84] P. J. Whelan. Control of locomotion in the decerebrate cat. *Progress in Neurobiology*, 49(5):481 – 515, 1996.

[85] Steffen Wittmeier, J Michael, Konstantinos Dalamagkidis, and Markus Rickert. CALIPER : A Universal Robot Simulation Framework for Tendon-Driven Robots. In *2011 IEEE/RSJ International Conference on Intelligent Robots and Systems*, pages 1063–1068, 2011.

[86] J. Y. Zhang and M. Ohsaki. Adaptive force density method for form-finding problem of tensegrity structures. *International Journal of Solids and Structures*, 43:5658–5673, 2006.

[87] L. Zhang and et al. Form-finding of nonregular tensegrity systems. *Journal of Structural Engineering*, 132:1435–1440, 2006.

[88] W. Zimmerman, J. Lunine, and R. Lorenz. A post-huygens titan surface science mission design. In *Aerospace Conference, 2005 IEEE*, pages 268–278, 2005.